

Accelerated Reliability Testing of Fresh and Field-Aged Photovoltaic Modules:  
Encapsulant Browning and Solder Bond Degradation

by

Hamsini Gopalakrishna

A Dissertation Presented in Partial Fulfillment  
of the Requirements for the Degree  
Doctor of Philosophy

Approved in April 2020 by the  
Graduate Supervisory Committee

Govindasamy Tamizhmani, Chair  
Bradley Rogers  
Peter Hacke

ARIZONA STATE UNIVERSITY

May 2020

## ABSTRACT

The popularity of solar photovoltaic (PV) energy is growing across the globe with more than 500 GW installed in 2018 with a capacity of 640 GW in 2019. Improved PV module reliability minimizes the levelized cost of energy. Studying and accelerating encapsulant browning and solder bond degradation—two of the most commonly observed degradation modes in the field—in a lab requires replicating the stress conditions that induce the same field degradation modes in a controlled accelerated environment to reduce testing time.

Accelerated testing is vital in learning about the reliability of solar PV modules. The unique streamlined approach taken saves time and resources with a statistically significant number of samples being tested in one chamber under multiple experimental stress conditions that closely mirror field conditions that induce encapsulant browning and solder bond degradation. With short circuit current ( $I_{sc}$ ) and series resistance ( $R_s$ ) degradation data sets at multiple temperatures, the activation energies ( $E_a$ ) for encapsulant browning and solder bond degradation was calculated.

Regular degradation was replaced by the wear-out stages of encapsulant browning and solder bond degradation by subjecting two types of field-aged modules to further accelerated testing. For browning, the  $E_a$  calculated through the Arrhenius model was  $0.37 \pm 0.17$  eV and  $0.71 \pm 0.07$  eV. For solder bond degradation, the Arrhenius model was used to calculate an  $E_a$  of  $0.12 \pm 0.05$  eV for solder with 2wt% Ag and  $0.35 \pm 0.04$  eV for Sn<sub>60</sub>Pb<sub>40</sub> solder.

To study the effect of types of encapsulant, backsheet, and solder on encapsulant browning and solder bond degradation, 9-cut-cell samples maximizing available data points while minimizing resources underwent accelerated tests described for modules. A ring-like browning feature was observed in samples with UV pass EVA above and UV cut EVA below the cells. The backsheet permeability influences the extent of oxygen photo-bleaching. In samples with solder bond degradation, increased bright spots and cell darkening resulted in increased  $R_s$ . Combining image processing with fluorescence imaging and electroluminescence imaging would yield great insight into the two degradation modes.

*To my parents C S Gopalakrishna and Rama Gopalakrishna  
for their unconditional love and support.*

*To my husband, Joe Victor Carpenter III, for believing  
in me while being in the same PhD boat.*

## ACKNOWLEDGEMENTS

I thank my thesis advisor, Dr. Govindasamy Tamizhmani for his valuable guidance and support. I also thank my committee members, Dr. Bradley Rogers at ASU and Dr. Peter Hacke at NREL for their valuable time and inputs. This material is based upon work supported by the Department of Energy, Office of Energy Efficiency and Renewable Energy (EERE), under Award Number DE-EE0007138. I thank the well-qualified and extremely helpful staff and students, both past and present, of Arizona State University's Photovoltaic Reliability Laboratory (ASU-PRL) for their timely help, faith in me, and their well wishes. Last but not least, I thank my family and friends for their constant encouragement.

## TABLE OF CONTENTS

	Page
LIST OF TABLES .....	xi
LIST OF FIGURES .....	xiv
CHAPTER	
1: INTRODUCTION .....	1
1.1 Components of a PV Module.....	1
1.1.1 Frame .....	2
1.1.2 Glass Superstrate.....	2
1.1.3 Encapsulant .....	2
1.1.4 Solar Cell and Cell Metallization.....	2
1.1.5 Glass or Polymer Substrate .....	3
1.2 Degradation of PV Modules .....	3
1.3 Studying the Reliability of PV Modules.....	6
1.4 Motivation and Objective .....	9
2: LITERATURE REVIEW .....	11
2.1 Polymers Used in Solar Modules.....	11
2.1.1 Encapsulants in Solar Modules .....	11

CHAPTER	Page
2.1.2 Backsheets in Solar Modules .....	18
2.2 Module Metallization in Solar Modules .....	20
3: EXPERIMENTAL METHODOLOGY .....	30
3.1 Characterization Methods .....	30
3.1.1 Ultra-violet Fluorescence (UVF) Imaging .....	33
3.1.2 Light current-voltage (LI-V) Curve Tracing.....	34
3.1.3 Dark Current-Voltage (DI-V) Curve Tracing .....	36
3.1.4 Electroluminescence (EL) Imaging .....	37
3.1.5 Infra-red (IR) Imaging .....	37
3.1.6 Colorimetry .....	38
3.1.7 Spectral Reflectance Measurements .....	39
3.1.8 Scanning Electron Microscopy and Energy Dispersive X-ray Spectroscopy .....	40
3.1.9 Quantum Efficiency (QE) Measurements.....	40
3.1.10 Cell-level LI-V and DI-V Measurements .....	42
3.2 Activation Energy Calculation.....	44
3.2.1 Arrhenius Model .....	44
3.3 Qualification tests as prescribed in IEC 61215.....	45

CHAPTER	Page
3.3.1 UV Pre-Conditioning [92] .....	45
3.3.2 Thermal Cycling (TC200) [92] .....	45
3.4 Accelerated Stress Testing to Induce Encapsulant Browning and Solder Bond Degradation in Field-Aged Modules .....	46
3.4.1 Studying Encapsulant Browning in Field-Aged Modules .....	46
Methodology .....	46
Encapsulant Browning Degradation Rate Prediction .....	51
3.4.2 Studying Solder Bond Degradation in Field-Aged Modules .....	53
Methodology .....	53
Solder Bond Degradation Rate Prediction .....	56
3.5 Accelerated Stress Testing to Induce Encapsulant Browning and Solder Bond Degradation in Freshly Fabricated 9-cut-cell Samples .....	57
3.5.1 Studying Encapsulant Browning in 9-cut-cell Samples UV-T exposure of 9-cut-cells with either UV-cut and UV-pass EVA Above and Below the Cell [97] .....	59
3.5.2 Combined UV-T-RH Accelerated Testing of PV Modules: Reliability of UV-Cut and UV-Pass EVA Encapsulants [98] .....	61
3.5.3 Combined UV-T-RH Accelerated Testing of 9-cut-cell Samples ..	64
3.5.4 Studying Solder Bond Degradation in 9-cut-cell Samples .....	66



CHAPTER	Page
4: RESULTS AND DISCUSSION.....	68
4.1 Accelerated Stress Testing to Induce Encapsulant Browning and Solder Bond Degradation in Field-Aged Modules .....	68
4.1.1 Studying Encapsulant Browning in Field-Aged Modules .....	68
Module-level Characterization Results.....	69
Cell-level Characterization Results.....	76
Activation Energy Calculation and Encapsulant Browning Degradation Rate Prediction.....	81
4.1.2 Studying Solder Bond Degradation in Field-Aged Modules.....	84
Module-level Characterization Results.....	86
Cell-level Characterization Results.....	87
Electron Imaging and Compositional Analysis .....	88
Activation Energy Calculation and Solder Bond Degradation Rate Prediction .....	93
4.2 Accelerated Stress Testing to Induce Encapsulant Browning And Solder Bond Degradation in Freshly Fabricated 9-cut-cell Samples.....	96
4.2.1 UV-T exposure of 9-cut-cells with either UV-cut and UV-pass EVA Above and Below the Cell .....	96

CHAPTER	Page
4.2.2 Combined UV-T-RH Accelerated Testing of PV Modules: Reliability of UV-Cut and UV-Pass EVA Encapsulants .....	99
4.2.3 Combined UV-T-RH Accelerated Testing of 9-cut-cell Samples	101
4.2.4 Studying Solder Bond Degradation in 9-cut-cell Samples .....	113
5: CONCLUSIONS AND OUTLOOK .....	119
5.1 Encapsulant Browning and Solder Bond Degradation .....	119
5.1.1 Field-Aged Modules .....	120
5.1.2 Fresh 9-cut-cell Samples .....	122
5.2 Outlook .....	124
REFERENCES .....	126
APPENDIX	
A LIST OF PUBLICATIONS .....	135

## LIST OF TABLES

Table	Page
I: Requirements of Encapsulants for Solar Module Application .....	12
II: Thermal Properties Of Materials at a Solder Bond.....	23
III: $T_H$ of Solders Used in this Work at Temperatures Used in Thermal Cycling.....	25
IV: List of Module-Level Characterization Techniques Used Along with Their Significance.....	30
V: List of Cell-Level Characterization Techniques Used Along with Their Significance	32
VI: Interpretation of I-V Curve Shapes Based on Fig. 22 .....	35
VII: Summary of the Fields of the Accelerated and the Field Databases. Grey Boxes Indicate Inapplicable or Unavailable Data.....	47
VIII: Summary of Sample Parameters and Stressors of Accelerated UV Exposure at Elevated Temperatures.....	59
IX: Summary of Sample Parameters and Stressors of Accelerated UV Exposure at Elevated Temperatures with Humidity .....	61
X: Summary of Sample Parameters and Stressors of Accelerated UV Exposure at Elevated Temperatures with Humidity .....	64
XI: Sample Parameters and Stressors Thermal Cycling.....	66
XII: Temperatures of MSX 60 and M55 Modules During the 450 kWh/m <sup>2</sup> UV Accelerated Test.....	68
XIII: Module-Level LI-V and DI-V Performance After 450 kWh/m <sup>2</sup> of UV Dosage .....	71

Table	Page
XIV: Predicted $I_{sc}$ Degradation Rates Based on Accelerated UV Exposure. Degradation Rates in %/Year. ....	82
XV: Degradation in I-V Parameters of MSX 60 and M55 Modules After the Modified TC Testing.....	85
XVI: Average % Cell-Level $R_s$ Increase in the MSX 60 and M55 Modules for 200 Cycles .....	88
XVII: Sample Temperatures Obtained with the Help of Silicone Heating Blankets. Due to the Lack of an Enclosure Box, Distinct Sample Temperatures Could not be Maintained in the UV-T Samples. ....	101
XVIII: YI Values Averaged from 18 Spots on each UV-H Sample Exposed to Accelerated UV Light at Elevated Temperatures with and Without Humidity .....	102
XIX: Percentage Decrease in Averaged $I_{sc}$ Values from Samples Exposed to Accelerated UV Light at Elevated Temperatures with and Without Humidity. Each Data Point is an Average of 9 Cells .....	102
XX: Summary of 9-Cut-Cell Samples Exposed to UV-T With Varying Intensities of Stressors.....	111
XXI: Summary of 9-Cut-Cell Samples Exposed to UV-T-RH with Varying Intensities of Stressors.....	112
XXII: Sample Temperatures Obtained with the Help of Silicone Heating Blankets Over 456 Modified Thermal Cycles. The Average of Samples Temperatures above	

Table	Page
75°C, 85°C, And 95°C Were Taken For The Low T, Mid T, And High T Samples, Respectively.....	113
XXIII: The % Increase in $R_s$ Using Dark I-V Based on Solder Bond Composition and Sample Temperature During the Hot Dwell Time. Each Data Point is an Average of 6 Cells. ....	113

## LIST OF FIGURES

Figure	Page
1. Components of a Typical Crystalline Silicon Module Along with Some Degradation Modes and Their Locations are Highlighted. Figure Adapted from [3].	4
2. Schematic of Irradiance Induced Degradations [4]. Changes in the Irradiance Reaching the Cell Usually Causes a Drop in the Short-Circuit Current of the Module.	4
3. Degradation Mechanisms Induced by Heat Whose Effects Include Increased Series Resistance, Decreased Voltage, Module Shunting, Severe Safety Issues, Decrease in Short-Circuit Current among others [4].	5
4. Degradation Mechanisms Induced by Humidity that can Affect all Components of a PV Module. Presence of Humidity Around and Inside a Module can cause Secondary Degradation Mechanisms that Affect the Power Output of the Module [4].	6
5. Bathtub Curve Describing the Causes of Different Failure Types in Product Reliability [9].	7
6. (a) Transmittance Curves of Freshly Laminated EVA (1), Yellowed EVA (2), and Dark Brown EVA (3). As the Encapsulant Degrades, More Chromophores are Formed Increasing the Light Absorption Within the Polymer Layer [14]. (b) Represents the Solar Spectrum at Sea Level. Even a Small Drop in Transmittance in the 250 nm – 1050 nm Range Greatly Affects the Power Output [18].	13
7. Equations Representing the Norrish I Reaction Whose Products Include Acetaldehyde Or Methane, Carbon-Dioxide, and Carbon Monoxide [20].	14
8. An EVA Reaction that Results in Lactone and Methane Formation [21].	14

Figure	Page
9. Equations Representing the Norrish II Reaction Whose Products Include Polyenes and Acetic Acid [20].	14
10. Equations Representing the Norrish III Reaction Whose Products Include Ketone and Aldehyde [20].	14
11. Formation of Conjugated Polyenes by Multistep Deacetylations [3].	15
12. Reaction of (a) the UV Absorber, 2-Hydroxy-4-Octoxybenzophenone (Cyasorb 531), with Products of Peroxide Homolysis and (b) The Hindered Amine Light Stabilizer (HALS), The Bis(2,2,6,6-Tetramethyl-4-Piperidiny)Sebacate (Tinuvin 770) [24].	15
13. Absorbance Curves of Various Chromophores Formed in EVA. As the Conjugation Length Increases, the Absorption Peaks Shift from Shorter to Longer Wavelengths [14].	16
14. Layers in TPT and KPE Backsheets Commonly Used in PV Modules. TPT Backsheets are Typically 0.34 mm Thick and KPE Backsheets Are 0.33 mm Thick.	18
15. SEM Image Showing Effects of (a) TMF [51] and (b) IMC Formation and Phase Coarsening Induced due to Thermal Cycling and Static Elevated Temperatures, Respectively [52].	21
16. Phase Diagrams of (a) SnPb [53] and (b) SnBi [54] Showing the Main Phases.	22
17. A Typical Creep Curve at Constant Stress and Elevated Temperature [44].	25
18. Creep Deformation map of Solder Alloys. With the Operational Temperature of Solders Being Above $0.65 T_H$ , the Grain Boundary, Lattice Diffusion, and Dislocation Creep is Dominant [68].	26

Figure	Page
19. Optical Micrographs Showing Grain Coarsening in (a) Sample Quenched in Liquid Nitrogen. (b) By Aging at 150°C for 15 Hours, the Grain Size Increased Significantly [75].	28
20. Schematic Representing the (a) Absorption and (b) Emission Spectra of Chromophores [80].	33
21 (a) Schematic of UVF Imaging Set-Up with two UV Light Source Arrays Angled Towards the Module. The Module Emits Visible Light. (b) Photograph of the Set-Up with the UV Arrays.	34
22 A Typical IV Curve with Some Common Anomalies (Dotted Lines) Highlighted in a Graph by Solmetric [81].	35
23. Schematic of Dark I-V and Light I-V [84]. The Inverse Slope at $V_{oc}$ Gives the Series Resistance ( $R_s$ ) and that at $I_{sc}$ Gives Shunt Resistance ( $R_{sh}$ ).	36
24. Typical EL Image Showing Cell Cracks, Isolated Dead-Cell Regions, and Cell Issues [85].	37
25. IR Imaging Highlighting Relatively Hotter Cells that Could Indicate Issues with Cell Metallization [86].	38
26. Components of the X, Y, and Z Color Space [89].	39
27. Representative QE Curve of a Typical Solar Cell [87].	41
28. Image of the Class AAA Continuous Solar Simulator at PRL in Use. The Incident Beam is Centered on the Cell.	42



Figure	Page
29. (a) Image of the Backside of a Module with Cells Cut. (b) Close up of One Cell where (1) The Al Tape, Backsheet, and Back EVA were cut to Access the Cell Interconnect. After Soldering the Ribbons, The Site was Covered with Silicone Paste to Prevent Moisture Ingress. (2) The Soldered Ribbons were Taped Down on Kapton Tape (Used for Insulation) to Give Strain Relief. (3) The Two Positive/Negative Ribbons from each Cell were Soldered Together to have one Point Used For Consistent Measurements.	43
30. Representative Arrhenius Plot from Which the Activation Energy can be Calculated. .....	44
31. (a) Photograph of the Outside of the UV Chamber Along with the Power Controller. Photograph Inside the UV Chamber (b) Without the UV Lamps on and (C) With the UV Lamps on.....	47
32. Images of the Prepared (a) MSX 60 and (b) M55 Modules that Underwent 450 kWh/m <sup>2</sup> of UV Eposure. ....	49
33. Schematic Showing the Alphanumeric System Used to Identify Cells in the Modules. For (a) MSX 60, the Junction Box was Placed to the Right During Imaging Characterizations. For (b) M55 Modules, the Positive Junction Box was Maintained on the Right During Imaging Characterizations. ....	50
34. Schematic Representing the Low T, Mid T, and High T Zones of the (a) MSX60 Module and the (b) M55 Module. The Grey Boxes Represent Cells not Covered by the Blankets and are Excluded from Data Analysis. Six Temperature Controllers with Six Attached Thermocouples were used to Control The Six Individual Heating Blankets.	

Figure	Page
(c) The Temperature and Current Injection Profiles of the Modified Thermal Cycling Test. Three Zones in Each Module were Maintained at Different Temperatures During the 15-Minute Dwell Time Using Three Thermally-Separated but Individually-Controlled Thermal Blankets. Current Equivalent to The Module $I_{sc}$ was Injected into the Module when the Chamber Temperature was above 25°C.....	54
35. Maximizing Data Points Available from one Cell by Cutting the Cell and then Laminating it Individually. ....	58
36. Schematic Showing the Spots where Colorimetry and Reflectance Measurements were Obtained for all 9-Cut-Cell Samples.....	58
37. Images of Samples with no Insulation on the UVC1 and UVP1 9-Cut-Cell Samples, Half-Inch Thick Foamboard Insulation on the UVC2 and UVP2 9-Cut-Cell Samples and Two-Inch Thick Foamboard Insulation on the UVC3 and UVP3 9-Cut-Cell Samples. ....	60
38. Concept of the Set-Up with UV and RH Exposure at Elevated Temperatures. ....	62
39. (a) And (b) Model of the UV-T-RH Setup Along with (c) and (d) Images of the Setup. ....	62
40. Distribution of Samples for Accelerated UV Exposure at Elevated Temperatures with and Without Humidity. ....	64
41. Schematic Showing the Three Solder Types in Each 9-Cut-Cell Sample Used for Accelerated Testing. ....	66

Figure	Page
42. Representation of Arrangement of Samples During the Thermal Cycling Test.....	67
43. UVF Images of Modules Before and After UV Exposure.....	70
44. EL Images of the Modules Before and After the UV Exposure. Current Equivalent to the Module $I_{sc}$ was Injected and the Image was Taken over 60 s. ....	73
45. Indoor IR Images of the Modules Before and After the UV Exposure. The Module was Connected in Forward Bias and Current Equivalent to the $I_{sc}$ was Injected for 5 Minutes. ....	74
46. Outdoor IR Images of the Modules Before and After the UV Exposure. The Module was Placed in the Sun under Short-Circuit Conditions for 5 Minutes.....	75
47. UVF Images with Cells Marked that Correspond to Measurements Taken. Solar Simulator Measurements were taken on the Cells Highlighted in Red. Reflectance, and Quantum Efficiency Measurements were Taken on Cells Highlighted in Yellow. Fresh Modules did not have their Cells Individually Accessed. ....	76
48. QE Measurements of Representative Cells from the Low T, Mid T, and High T Modules of MSX 60 and M55 Modules. The Cell Centers Consistently show Lower QE than the Cell Edges Between 400 nm and 900 nm. ....	78
49. Reflectance Curves from one Representative Cell in each of the Six Field-Aged Modules, the same for which QE Measurements are Shown in Fig. 48.....	79
50. Box Plot of the Cell-Level $I_{sc}$ Measurements of the Individual Cells in the MSX 60 and M55 Modules. Module-Level $I_{sc}$ (At 0 kWh/m <sup>2</sup> ) was taken as the Initial Measurement whereas Cell-Level $I_{sc}$ (At 450 kWh/m <sup>2</sup> ) was taken as the Final Measurement.....	80

Figure	Page
51. Activation Energy Calculation from the Average % $I_{sc}$ Drop from the MSX 60 and M55 Module. The $E_a$ for MSX 60 Modules is 0.37 eV. The Low T, Mid T, and High T Data Points Represent the Average % $I_{sc}$ Drop of 10 Cells, 9 Cells, and 12 Cells, Respectively. The $E_a$ for M55 Modules is 0.71 eV. The Low T, Mid T, and High T Data Points Represent the Average % $I_{sc}$ Drop of 16 Cells, 13 Cells, and 13 Cells, Respectively.....	81
52. The Achieved Thermal Profiles of the MSX 60 Module with Three Temperatures During 15 Minute Dwell Time of Accelerated TC Test. The Black Line Corresponds to Chamber Temperature. ....	84
53. (a – d) EL and (e – h) IR Images of the Field-Exposed Modules Before and After Thermal Cycling. The MSX60 Module EL Images (a and c) do not show Much Degradation Whereas the M55 Module (b And d) shows an Overall Cell Darkening and Brightness near the Busbars Indicate Increased $R_s$ Leading to Electron Crowding. The Cells in Green on the MSX60 Module and the Cells in Yellow on the M55 Module Correspond to the Cells in IR Imaging that have a Slightly Higher Temperature.....	87
54. SEM Micrograph of a Sample from the MSX 60 Mid T Region (a) with a Corresponding Line Scan Showing the At% Of Pb, Cu, and Sn (b). Between 5 $\mu\text{m}$ and 8 $\mu\text{m}$ , the IMC Observed is $\text{Cu}_3\text{Sn}$ . Some Segregation was Observed with Pb-Rich and Sn-Rich Phases. The $\text{Cu}_6\text{Sn}_5$ IMC Layer was about 3 $\mu\text{m}$ Thick.....	89
55. SE Micrographs of Cell Interconnect Cross-Sections from the Three Temperature Zones of the MSX60 and the M55 Modules along with their Corresponding EDXS	

Figure	Page
Maps. Note the Feature-Size Appropriate Scale Bars used in the Mid T and High T Sample Images of the MSX Module. Overlap of Cu and Sn Maps Indicate at the Presence of Cu <sub>3</sub> Sn and Cu <sub>6</sub> Sn <sub>5</sub> IMCs. While the Low T MSX60 Sample has a Lamellar Structure, an Increase in the Pb-Rich Segregation was Observed in the Mid T (94 Pb-Rich Islands with an average area Of 14.38 μm <sup>2</sup> ) and High T (15 Pb-Rich Islands with an average area of 82.64 μm <sup>2</sup> ) Samples. Samples from all Temperature Zones of the M55 Module Show Major Segregation.....	90
56. Arrhenius Plot for Solder Bond Degradation with the Average R <sub>s</sub> Degradation in Cells from the MSX 60 and the M55 Module. The E <sub>a</sub> Calculated for the MSX 60 Module was 0.12 eV. The Low T, Mid T, and High T Data Points Represent the Average %R <sub>s</sub> Increase of 7 Cells, 5 Cells, and 7 Cells, Respectively. The M55 Module was 0.35 eV. The Low T, Mid T, and High T Data Points Represent the Average %R <sub>s</sub> Increase of 6 Cells, 9 Cells, and 5 Cells, Respectively. ....	93
57. UVF Images of the 9-Cut-Cell Samples with UVC EVA and UVP EVA at Every 200 kWh/m <sup>2</sup> . ....	96
58. (a) I <sub>sc</sub> Change after every 200 kWh/m <sup>2</sup> until 600 kWh/m <sup>2</sup> Show Little Drop. (b) YI Change over the Duration of the Test. The YI Increase in the UVC Samples Indicate that Encapsulant Browning is the Likely Degradation Mode whereas the Negligible Change in the YI of the UVP Mini-Modules Indicate a Different Degradation Mode. ....	97

Figure	Page
59. Close-Up UVF Images of one Cell from the (a) UVC3 and the (b) UVP3 Samples. The area of Browning is Clearly Seen in the UVC3 Sample. A Ring Like Pattern is Seen in the UVP3 Sample that could be Attributed to EVA Main Chain Degradation. ....	98
60. UVF Imaging of UVC and UVH Samples at Different Temperatures and Humidities. the Extent of Encapsulant Browning and Influence of Oxygen Diffusion can be Seen. the Ring-Like Feature is Browning.....	99
61. (a) Median $I_{sc}$ Drop in the Six 9-Cut-Cell Samples after 186 kWh/m <sup>2</sup> of UV Dosage. (b) The YI Plot Shows a Consistent Increase YI Data for all 9-Cut-Cell Samples. .	100
62. Box Plots of (a) Samples with TPT Backsheets in the UV-T Test, (b) Samples with KPE Backsheets in the UV-T, (c) Samples with TPT Backsheet in the UV-T-RH Test, and (d) Samples with the KPE Backsheet in the UV-T-RH Test. ....	103
63. UVF Images of 9-Cut-Cell Samples During the 225 kWh/m <sup>2</sup> of UV Exposure at Elevated Temperatures Without Humidity. ....	105
64. UVF Images of 9-Cut-Cell Samples During the 225 kWh/m <sup>2</sup> of UV Exposure at Elevated Temperatures and Humidity. ....	106
65. Schematic Showing the Possible Pathways of Encapsulant Browning and Subsequent Oxygen Photobleaching due to the Movement of UV Absorbers During Lamination. ....	107
66. Reflectance Measurements Before and After UV Exposure (a) and (b) with Elevated Temperatures and (c) and (d) with Elevated Temperatures and Relative Humidity. Each Line is the Median of 18 Measurements from Each 9-Cut-Cell Sample. The Inset	

Figure	Page
Figures show a Decrease in Reflectance Between 350 nm – 370 nm Indicating an Increase in the Absorbance. ....	109
67. Comparative UVF Images with Varying EVA Combinations Showing the Effect of EVA Type on Extent and Pattern of Encapsulant Browning.....	111
68. Average $R_s$ Increase and Standard Deviation in the 9-Cut-Cell Samples that Underwent Thermal Cycling Separated by Solder Type (a) for $Pb_{36}Sn_{62}Ag_2$ (6 Cells), (b) for $Pb_{40}Sn_{60}$ (6 Cells), and (c) $Sn_{42}Bi_{58}$ (6 Cells). ....	114
69. Individual Cell-Level EL Images Corresponding to Cells with Relatively Higher $R_s$ . the Cells Exhibit Cell Darkening and Formation of Bright Spots. ....	116
70. EL Images of 9-Cut-Cell Samples Before, During, and After 456 Thermal Cycles.	118

## CHAPTER 1: INTRODUCTION

The world is moving towards renewable energy sources. The global photovoltaic (PV) installation by the end 2018 was 512.3 GW with 54% being installed between 2015 – 2018 [1]. The increased role of solar in energizing the world necessitates a deeper understanding of the technology and its reliability. Photovoltaics is versatile with the possibility of residential, commercial, and utility scale installations. Most installations need minimal maintenance over their 25 – 30 year lifetime. With crystalline silicon-based PV technology (mono- and poly- crystalline) accounting for 95% of the module production, a lot of research is being done into its various aspects of crystalline silicon technology including reliability. Thin film technologies (CdTe, CIGS, amorphous, etc.) account for 5% of the global module production [2].

### 1.1 Components of a PV Module

Solar modules are a laminate of multiple materials; each carefully selected for their properties and economics. The superstrate/substrate combination is the module construction; most modules have a glass/backsheet construction while some have glass/glass construction. The structure of the PV laminate includes i) high transmittance glass superstrate, ii) highly transparent polymer encapsulant, iii) solar cells wired with solder-coated copper interconnects, iv) highly transparent polymer encapsulant, and v) glass or a polymer backsheet. The module leads are housed inside a junction box on the backsheet of the module. The entire laminate is encased in a metal frame for added structural support.



### 1.1.1 Frame

Most modules have an aluminum frame to increase structural integrity. Frames also make mounting modules easier. The frame encompasses an edge seal and a rubber inlay to help reduce moisture ingress through the module edge.

### 1.1.2 Glass Superstrate

The low-Fe, tempered glass typically used in solar modules is 3.2 mm thick. Some manufacturers have started to use 2.5 mm thick glass. The glass offers high optical transmittance, mechanical stability, electrical insulation, water impermeability, and impact resistance. The glass could contain cerium oxide that absorbs some of the incident UV light.

### 1.1.3 Encapsulant

Encapsulants provide structural support and positioning during the various stages of manufacturing, transportation, handling, and installation. It helps with optical coupling between the glass superstrate and the solar cell while physically isolating the cells and other components from the stresses of the environment. It also helps electrically isolate the cells from a safety and an operational standpoint [3]. The most popular encapsulant used is ethylene vinyl acetate (EVA).

### 1.1.4 Solar Cell and Cell Metallization

The solar cell is usually a doped semiconductor with a p-n junction. The cells sometimes have anti-reflection coatings. PV module technology is classified based on the type of cells. Crystalline technology refers to either monocrystalline or polycrystalline cells. Monocrystalline cells have higher efficiency than polycrystalline cells owing to the

absence of grain boundaries. However, polycrystalline silicon cells are easier to fabricate. Several cell architectures exist within silicon cells which are usually 150 – 300 microns thick. Thin film, having cells a few microns thick, are usually made from CIGS, CIS, amorphous silicon, CdTe, etc. The potential failure modes and degradation mechanisms for different cell materials changes with the cell technology.

Cell metallization typically consists of screen-printed silver (Ag) positive and negative terminals on the solar cell. The metallization on the cells include fingers, that collect the charges generated by the solar cell, and busbars, that carry the charge to the terminals of the module. Cell interconnects connect cells in series and have a copper core coated with a lead-tin solder.

#### 1.1.5 Glass or Polymer Substrate

The substrate shields the module from harsh environmental conditions. The substrate of modules is usually a permeable polymer backsheets. Some modules have a glass substrate that increases the structural integrity. However, glass substrates add weight to the module, are impermeable to the degradation by-products and decrease heat dissipation.

### 1.2 Degradation of PV Modules

Each of the numerous materials, interfaces, and components involved have a significant role in regular operation of modules and yet pose unique challenges for module reliability. Prolonged exposure of solar modules to environmental factors cause degradation of its components and interfaces resulting directly or indirectly in significant power loss. Primary degradations in modules can make way for secondary degradation mechanisms causing

further power loss. Fig. 1 illustrates the components, degradation modes and their locations seen in field-aged modules

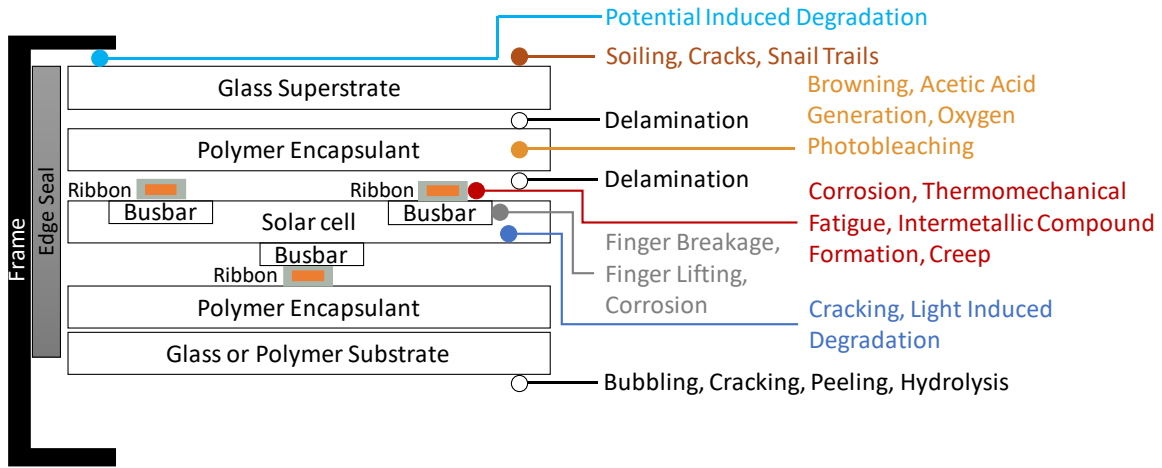


Fig. 1. Components of a typical crystalline silicon module along with some degradation modes and their locations are highlighted. Figure adapted from [3].

The main environmental factors PV modules are exposed to are light (Fig. 2), heat (Fig. 3), and humidity (Fig. 4). Other factors like soiling, cloud cycling, snow load, wind load, albedo, air conditions (salty conditions), and hail affect the power output and safety of modules.

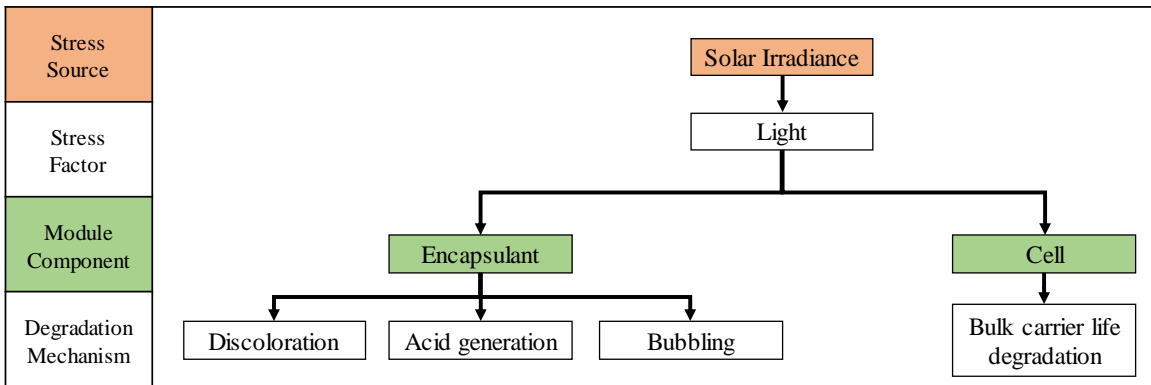


Fig. 2. Schematic of irradiance induced degradations [4]. Changes in the irradiance reaching the cell usually causes a drop in the short-circuit current of the module.

With prolonged exposure to irradiance, parts of the sun’s spectrum interact with the polymers and additives in the encapsulant causing structural changes that hinder full

functionality of the encapsulant. Acid generation could lead to further encapsulant discoloration and metallization corrosion. Bubbling could cause delamination and reduced  $I_{sc}$  generation. The cells undergo light induced degradation by the Staebler-Wronski effect where reduced cell performance stabilizes after a 1% - 5% drop in the short-circuit current ( $I_{sc}$ ) [5], [6]. Irradiance changes the material properties of the encapsulant and the cell leading to reduced power output. These degradation mechanisms lead to other safety and performance issues.

Thermal stresses cause degradation of most of the module components especially in conjunction with other stressors. Intermetallic compound (IMC) formation, thermomechanical fatigue (TMF), creep, and related phenomenon are encouraged in the presence of thermal stresses. Thermal stresses can accelerate other ongoing degradation modes such as encapsulant browning and delamination.

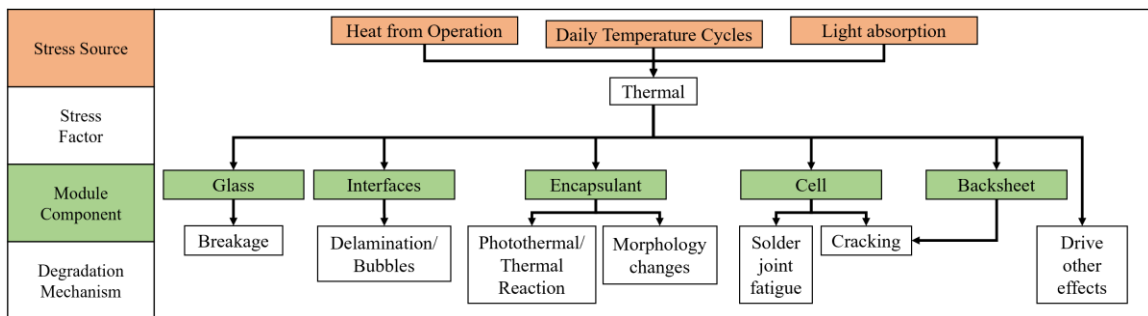


Fig. 3. Degradation mechanisms induced by heat whose effects include increased series resistance, decreased voltage, module shunting, severe safety issues, decrease in short-circuit current among others [4].

The main pathway for moisture ingress in a glass/backsheets modules is through the backsheets. Some can enter through the edge seal if it degrades. Glass is impermeable to water vapor and in a glass/glass module, the only moisture ingress pathway would be through degraded edge seal. Moisture on the glass could make conditions conducive for

potential induced degradation [7]. Once moisture enters the laminate through the backsheet, it interacts with the backsheet, back and front EVA layers, and the metallization.

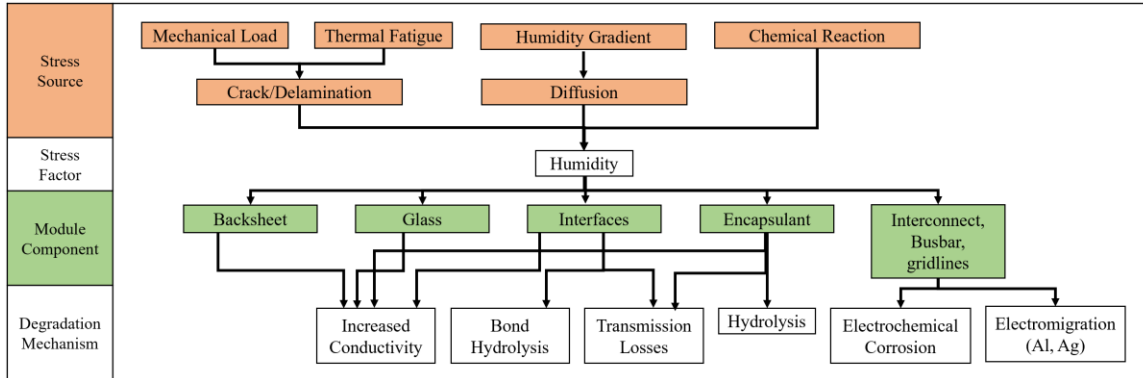


Fig. 4. Degradation mechanisms induced by humidity that can affect all components of a PV module. Presence of humidity around and inside a module can cause secondary degradation mechanisms that affect the power output of the module [4].

Rarely in the field, are modules exposed to a single environmental factor. The combined effect of multiple factors can drastically affect the electrical parameters of short-circuit current ( $I_{sc}$ ), open-circuit voltage ( $V_{oc}$ ), and maximum power ( $P_{max}$ ). The  $P_{max}$  is the product of the  $I_{sc}$ ,  $V_{oc}$ , and the fill factor (FF) of a module. The primary degradations seen in modules can make way for secondary degradation mechanisms. Hydrolysis leads to acid generation, corrosion, and current leakage. Delamination leads to decoupling of transmitted light, heat trapping, and thermal fatigue.

### 1.3 Studying the Reliability of PV Modules

The general trend seen in reliability of products is shown in a bathtub curve (Fig. 5). The three parts of the Observed Failure Rate can be classified as Infant Mortality, Useful Life, and Wear Out. In the first stage, failures related to product design, choice of material, and fabrication method are observed. In the second stage, randomly occurring failures

during the useful life are observed. In the third stage, the components have reached the end of their useful life and fail due to the applied stresses over the product lifetime [8].

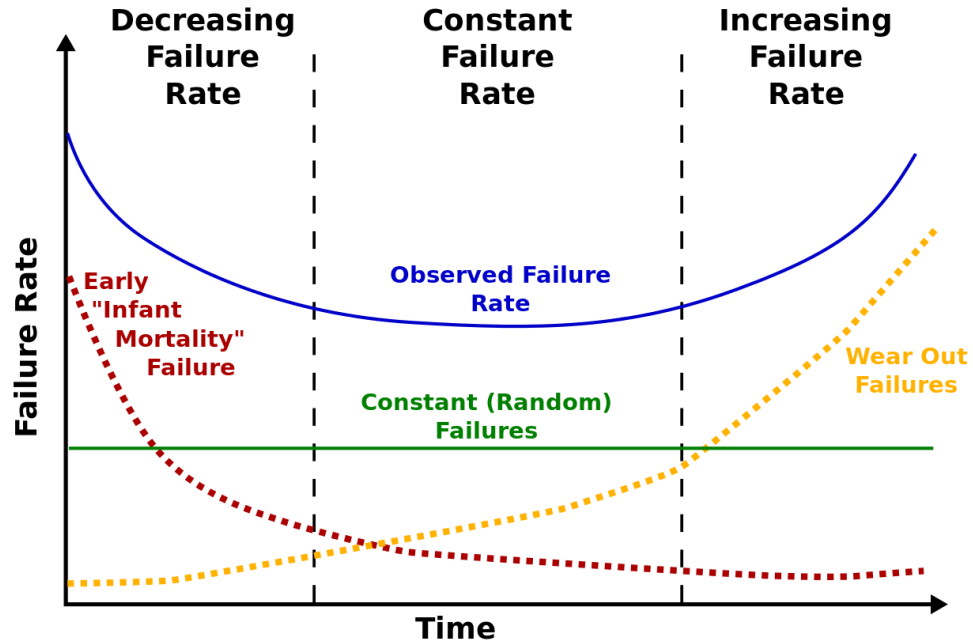


Fig. 5. Bathtub curve describing the causes of different failure types in product reliability [9]

With reduced levelized cost of energy (LCOE), solar energy becomes more economically viable. The LCOE depends on capital investment, operations/maintenance expenses, fuel expenses (nil in the case of renewables), electricity generated, financial discount rate, and system lifetime [10]. To reduce LCOE, the cost of the system (capital and operations/maintenance) should be minimized while increasing the technology efficiency (energy generation) and system reliability (lifetime of the system). All three aspects are equally important in decreasing the LCOE [11]. Studying PV module reliability and understanding the various degradation modes that occur is vital. Solar modules have to undergo, and pass qualification tests as specified by the International Electrotechnical Commission (IEC) standards before they can be sold on the market. These stringent tests

are aimed at addressing design and material issues with modules that contribute to infant mortality failures. While qualification tests address infant-mortality failures, wear-out failures remain under-studied.

In the field, two of the most commonly observed failure modes are encapsulant browning and solder bond degradation [12]. They correspond to charge generation and collection within the solar module, respectively. The initial and mid-life stages of encapsulant browning and solder bond degradation have been well studied. The end-of-life stages of the encapsulant browning and solder bond degradation modes are yet to be explored extensively. Understanding failure mechanisms at different stages of the module's lifetime enables predicting the power output. Accelerated tests are widely used to study PV module reliability. The aim of accelerated tests is to replicate failures seen in the field within a much shorter time frame. This is done by increasing the intensity of stressors modules are exposed to in normal field operation such as temperature, humidity, UV light, but not to the extent that would cause run-away degradations that would not occur in the field.

## 1.4 Motivation and Objective

Module reliability depends on the reliability of its components. With encapsulant browning and solder bond degradation being the most commonly observed field degradation modes, both modes are studied through the correlation between outdoor field testing and indoor accelerated stress testing. The effect of environmental stressors with and without humidity on encapsulant browning of samples with different backsheets and EVA types is investigated. The influence of static temperature and cycling temperature on the integrity of cell interconnects and solder bonds is also investigated. The work presented aims to address the following questions:

- How does the end-of-life stage of **encapsulant browning** manifest itself in modules that have already been field exposed?
  - How does module **temperature** (60°C - 80°C) affect encapsulant browning?
- How does the end-of-life stage of **solder bond degradation** manifest itself in modules that have already been field exposed?
  - How does solder bond **composition** (Sn<sub>62</sub>Pb<sub>36</sub>Ag<sub>2</sub> and Sn<sub>60</sub>Pb<sub>40</sub> at solder joint) affect solder bond degradation?
  - How does **temperature** (85°C, 95°C, and 105°C) affect solder bond degradation?

Accelerated tests were carried out on samples with new materials and material combinations to better understand how encapsulants, backsheets, and different



compositions of cell metallization degrade with exposure to combined stressors such as humidity, temperature, and UV light.

- How does **encapsulant browning** manifest itself in freshly fabricated samples when exposed to accelerated UV light?
  - What is the effect of different **types of EVA encapsulants** (UV Cut and UV Pass) in samples?
  - What is the role of **temperature and humidity** (three temperatures and two humidity levels) in encapsulant browning?
  - What is the effect of **backsheet type** (PET and PVDF) on encapsulant browning and photobleaching?
- How does **solder bond degradation** manifest itself in freshly fabricated samples undergoing thermal cycling with different solder bond compositions?
  - How does solder bond **composition** ( $\text{Sn}_{62}\text{Pb}_{36}\text{Ag}_2$ ,  $\text{Sn}_{60}\text{Pb}_{40}$ ,  $\text{Sn}_{42}\text{Bi}_{58}$ ) affect solder bond degradation?
  - How does **temperature** (85°C, 95°C, and 105°C) affect solder bond degradation?

Chapter 2 goes over existing research found in literature review pertaining to encapsulant browning and solder bond degradation. Chapter 3 details the methodology of testing for and characterizing encapsulant browning and solder bond degradation. Chapter 4, reporting the results, discussion, and related analysis of the testing described in Chapter 3, culminates in the take-aways from experimentation. Chapter 5 summarizes the findings and presents future outlook.

## CHAPTER 2: LITERATURE REVIEW

Prolonged exposure of PV modules to environmental stressors causes degradation in the various components within a module which can lead to secondary degradation mechanisms.

### 2.1 Polymers Used in Solar Modules

Two of the main polymer components used in solar modules are encapsulants and backsheets. They have different but specific functions within a module. The properties and degradation mechanisms of the encapsulant and backsheet vary.

#### 2.1.1 Encapsulants in Solar Modules

Given the wide range of environmental stressors modules are expected to reliably withstand for 20 – 25 years, the encapsulant must meet the criteria listed in TABLE I. Encapsulants, having high transmittance, provide optical coupling between the solar cell and the glass. As a choice of encapsulant, only silicones met the criteria as they are resistant to hydrolysis, thermal oxidation, and UV photo-oxidation. However, when cost was considered, EVA was a clear choice.

EVA in PV applications is a copolymer of ethylene units and vinyl acetate units (~33 wt.%). Two types of EVA used widely in the PV industry are UV cut (UVC) EVA which absorbs light below 360 nm and UV pass (UVP) which allows all incident light to reach the solar cell. The UVC EVA formulation typically includes a UV absorber (Cyasorb UV 531), a UV stabilizer (Tinuvin 770), an anti-oxidant (Naugard P), and a peroxide curing agent (Lupersol 101 or Lupersol TBEC). The UVP EVA formulation omits the UV absorber. Traditionally, modules use UVC EVA both above and below the cell. The trend

has now shifted to using UVP EVA above the cell to circumvent encapsulant browning. The UVC EVA below the cell prevents backsheet degradation due to interaction with the UV light incident on inter-cell regions.

TABLE I: REQUIREMENTS OF ENCAPSULANTS FOR SOLAR MODULE APPLICATION

<b>Characteristic</b>	<b>Specification/Requirement</b>
Glass transition temperature ( $T_g$ )	< -40°C
Total hemispherical light transmission	> 90% of incident light
Hydrolysis	None at 80°C and 100% RH
Water absorption	< 0.5 wt.% at 20°C/100% RH
Resistance to thermal oxidation	Stable up to 85°C
Mechanical creep	None at 90°C
Tensile modulus	< 20.7 MPa at 25°C
Fabrication temperature	< 170°C
Fabrication pressure for lamination	1 atmosphere
Chemical inertness	No reaction with embedded Cu coupons at 90°C
UV absorption degradation	None at wavelengths above 350 nm
Hazing or clouding	None at 80°C and 100% RH
Minimum thickness	0.152 mm
Odor, human hazards	None

EVA is usually crosslinked with the curing agent for use in module lamination. The gel content is the fraction of the polymer that has been crosslinked. A gel content of above 60%, but preferably above 80%, is required for EVA in solar modules to ensure good creep resistance [13]. The degradation modes and their rates are determined by the environmental conditions the solar module experiences in the field/accelerated test. The bonds in the encapsulant and the additives are modified thus changing their optical and mechanical properties. With exposure to UV light, the gel content can increase to about 96% (with browned EVA) but so long as the encapsulant is soft and elastic, it does not pose a problem to module performance [3]. Areas with increased gel content also have very low amount

of the UV absorber [14]. Chromophores impart color to the material and their formation can be reversible or irreversible [15]. The curing temperature, time, and cross-linker concentration dictate the gel content and the chromophores formed during lamination [3]. Longer curing times and higher curing temperatures lead to a greater concentration of chromophores [16]. Freshly laminated transparent polymer encapsulants start to turn yellow and eventually brown with prolonged exposure to UV. Humidity and elevated temperatures enhance encapsulant browning. EVA also undergoes discoloration [17].

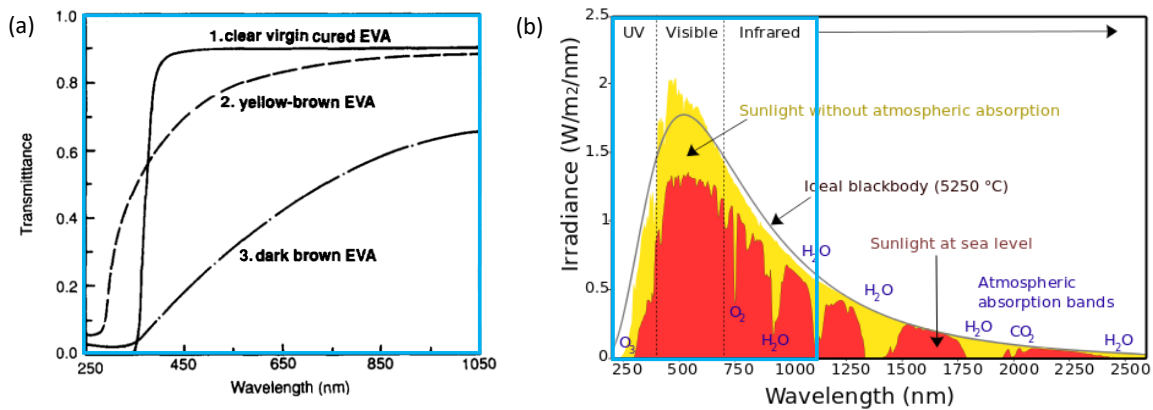


Fig. 6. (a) Transmittance curves of freshly laminated EVA (1), yellowed EVA (2), and dark brown EVA (3). As the encapsulant degrades, more chromophores are formed increasing the light absorption within the polymer layer [14]. (b) represents the solar spectrum at sea level. Even a small drop in transmittance in the 250 nm – 1050 nm range greatly affects the power output [18].

Fig. 6 (a) shows the effect of chromophore formation on transmittance. The sun's irradiance at the sea level is most intense in the visible range. Hence maximizing the absorption in this range is extremely beneficial to increasing cell efficiency. The discoloration is thought to originate from either the degradation of additives in EVA and/or the degradation of the EVA main chain itself [3], [19]. Oxidation of polymers, like any polymer reaction, has three steps: initiation, propagation, and termination. Four main EVA

degradation reactions are shown in Fig. 7 – Fig. 10. EVA degradation also results from formation of polyconjugated polyenes by multistep deacetylations as seen in Fig. 11.

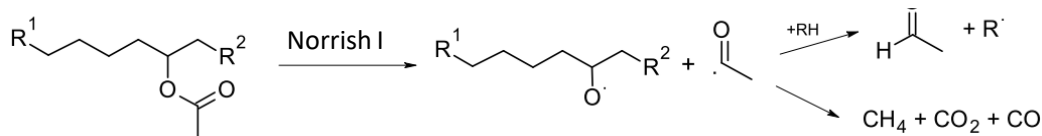


Fig. 7. Equations representing the Norrish I reaction whose products include acetaldehyde or methane, carbon-dioxide, and carbon monoxide [20].

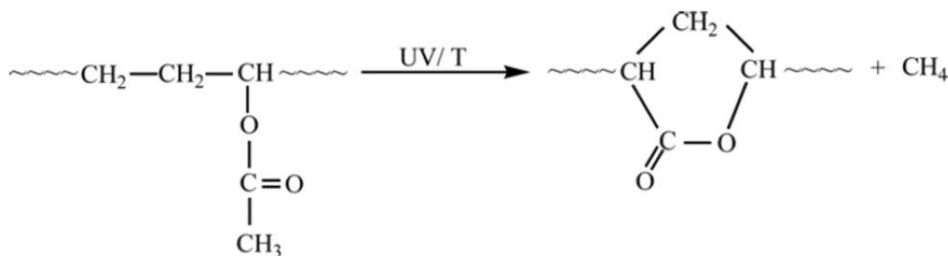


Fig. 8. An EVA reaction that results in lactone and methane formation [21].

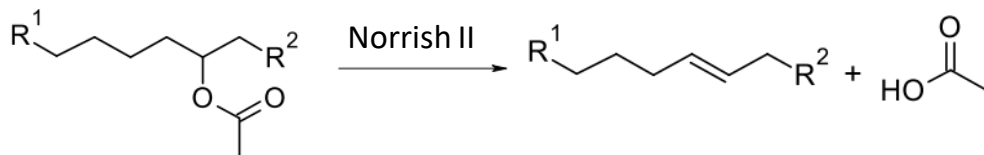


Fig. 9. Equations representing the Norrish II reaction whose products include polyenes and acetic acid [20].

The hydrolysis/deacetylation reaction of EVA in the Norrish II reaction results in acetic acid formation which is a self-catalyst leading to increased rate of encapsulant browning. The generation of acetic acid close to the cell metallization also facilitates faster rates of corrosion [16], [22].

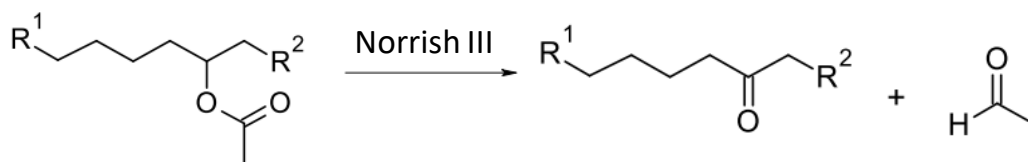


Fig. 10. Equations representing the Norrish III reaction whose products include ketone and aldehyde [20].

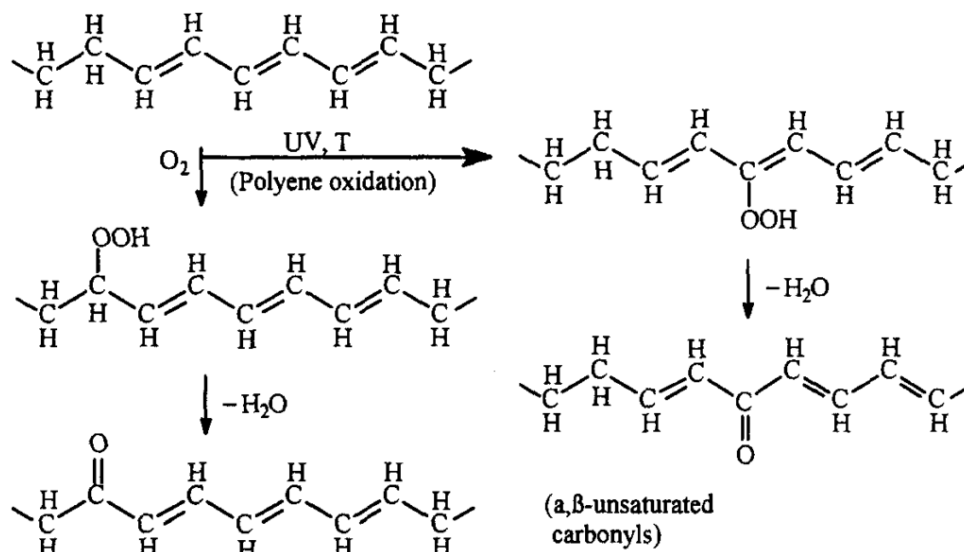


Fig. 11. Formation of conjugated polyenes by multistep deacetylations [3].

The polyenes from the main chain EVA (Fig. 11) and the degradation of the additives result in chromophore formation (Fig. 12). Longer chromophore conjugation lengths lead to darker EVA color (Fig. 13). The discolored EVA absorbs some of the light on its way to the solar cell, thus reducing the short circuit current ( $I_{sc}$ ) and output power ( $P_{max}$ ) [23].

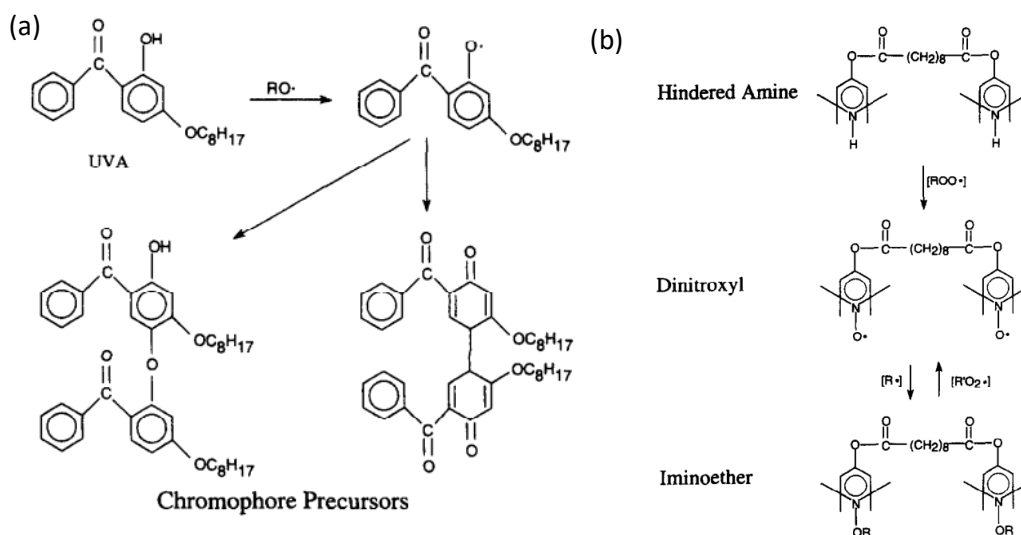


Fig. 12. Reaction of (a) the UV absorber, 2-Hydroxy-4-octoxybenzophenone (Cyasorb 531), with products of peroxide homolysis and (b) the Hindered Amine Light Stabilizer (HALS), the bis(2,2,6,6-Tetramethyl-4-piperidinyl)sebacate (Tinuvin 770) [24].

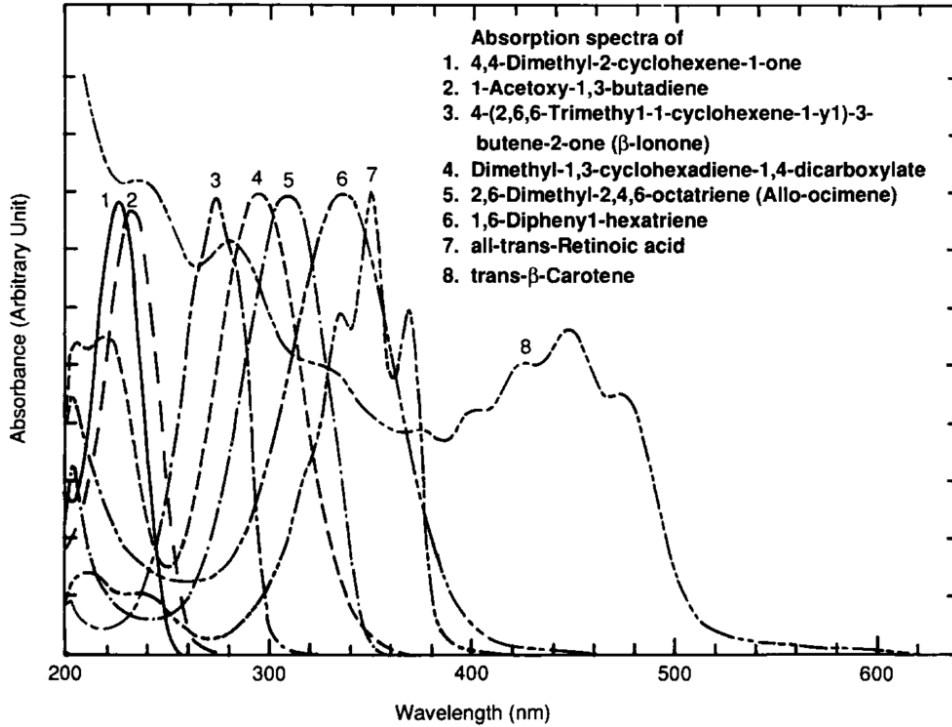


Fig. 13. Absorbance curves of various chromophores formed in EVA. As the conjugation length increases, the absorption peaks shift from shorter to longer wavelengths [14].

During field exposure of modules, a counter-reaction to EVA browning takes place simultaneously: oxygen photobleaching occurring in modules with a permeable polymer backsheet [25]. The oxygen in the ambient air diffuses through the backsheet and bleaches the discolored EVA, in the presence of sunlight [16], [26]–[29]. Cracked cells also enhance this bleaching reaction by creating more pathways for oxygen diffusion [30]. EVA is permeable to oxygen ( $3000 \text{ cm}^2/\text{m}^2 \cdot \text{day}$ ) and water vapor ( $80 \text{ g}/\text{m}^2 \cdot \text{day}$ ) [31]. In addition to transmission rates of EVA, those of the backsheet also play a role in regulating photobleaching of browned EVA. UV light from 310 nm – 370 nm photo-oxidize chromophores to a product without color. While photobleaching can occur with visible light, it is faster with wavelengths closer to 305 nm. The emission spectra of photobleached EVA is similar to fresh cured EVA. However, there is a difference in the gel content and

the UV absorber concentrations which can affect the mechanical properties of the encapsulant [14]. Both EVA browning and photobleaching are temperature dependent reactions. As the module temperature increases, the browning and the photobleaching reaction rates also increase [32]. On the other hand, modules having glass-glass construction will undergo a more intensified browning reaction as oxygen diffusion through the impermeable glass sheet is eliminated [33]. The recent trend in the PV industry is to use UVP EVA above the cell as a solution to encapsulant browning. The absence of UV absorbers would drastically reduce chromophore formation. However, studies have shown that modules with UVP EVA above the cell and UVC EVA below the cell still have some browning/discoloration of the encapsulant as observed from UV fluorescence imaging [34], [35]. This is thought to originate from some additive transfer from the UVC EVA below the cell to the UVP EVA above the cell during lamination in the inter-cell regions due to concentration gradients [24].

Accelerated UV exposure tests and long-term field-aged modules are major data sources to study encapsulant browning. The 15 kWh/m<sup>2</sup> of UV preconditioning test required in the IEC 61215 (qualification standard for terrestrial solar modules) [36] tests only the interfacial bond strength of the encapsulant with the top glass and the silicon cell, but not the bonds or additives within the bulk of material which are associated with the browning reaction. The 15 kWh/m<sup>2</sup> UV dosage is negligible compared to the 8 – 10 years needed for modules to overtly show browning in the field [24], [37].



### 2.1.2 Backsheets in Solar Modules

Backsheets are typically made of three polymer layers held together by epoxy or adhesives. The middle layer acts as an electrical insulator and a permeation barrier and is enclosed by a protective layer (air side) and a layer suited for adhesion to the encapsulant [38]. Backsheets need to be electrically insulating as modules can be part of strings that can reach a total voltage of 1500 V. The outer layer protects against environmental factors (wind, dust, UV from albedo, moisture). The use of a polymer substrate reduces the weight of modules dramatically allowing for easier shipping and handling. One of the most common backsheets used in the PV industry is Polyvinyl Fluoride – Polyethylene Terephthalate – Polyvinyl Fluoride (also known as Tedlar-PET-Tedlar or TPT). Another common alternative is Polyvinylidene Fluoride – Polyethylene Terephthalate – Ethylene Vinyl Acetate (also known as Kynar-PET-EVA or KPE) both shown in Fig. 14.

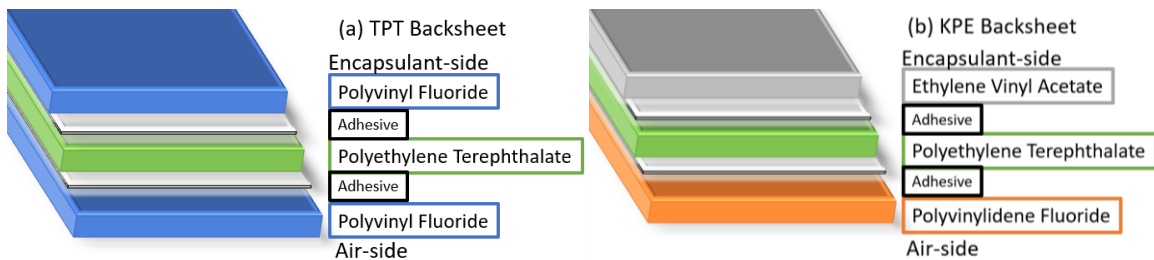


Fig. 14. Layers in TPT and KPE backsheets commonly used in PV modules. TPT backsheets are typically 0.34 mm thick and KPE backsheets are 0.33 mm thick.

The physical and chemical properties of the backsheets differ with the materials used and the environmental factors. Light in the 300 nm – 350 nm range is absorbed by PET leading to discoloration, embrittlement, and cracking [39], [40]. Typically, backsheets allow some diffusion of water vapor and oxygen that lead to changes in the materials of the PV module and their properties.

The oxygen transmission rate (OTR) through the backsheet can be described by Fick's law

$$\frac{\partial c}{\partial t} = D \frac{\partial^2 c}{\partial x^2} \quad \text{Eq. 1}$$

where  $c$  is the concentration,  $D$  is diffusivity,  $t$  is time, and  $x$  is the position within the material [41]. With increased temperature, the amount of oxygen diffusing increases. Oxygen that diffuses through the backsheet photobleaches browned EVA by breaking up the conjugated double bonds thus increasing its transmittance [38].

Water vapor enhances delamination and encapsulant browning especially when combined with other environmental factors. The water vapor transmission rate (WVTR) can be described as

$$WVTR(t) = \frac{DC_s}{l} \left[ 1 + 2 \sum_{n=1}^{\infty} (-1)^n e^{\left( \frac{-Dn^2 \pi^2 t}{l^2} \right)} \right] \quad \text{Eq. 2}$$

where  $D$  is diffusivity,  $C_s$  is saturation concentration,  $l$  is sample thickness [42]. In the field, water vapor in the PV module stabilizes between 38% - 58% based on climate for a PET based backsheet and EVA encapsulant [43]. The water vapor transmission rate for TPT and KPE backsheets used in this work are 2.3 g/m<sup>2</sup>•day and 2.0 g/m<sup>2</sup>•day, respectively. The OTR and WVTR dictate the rate of oxygen photobleaching of browned EVA and hydrolysis of EVA.

## 2.2 Module Metallization in Solar Modules

Solder bond degradation and encapsulant browning are two of the most dominant degradation modes seen in field-aged modules [6], [29]. Ribbons connect cells within PV modules and conduct current generated to the electrical terminals in the junction box. These ribbons consist of a copper (Cu) core covered with a thin (10  $\mu\text{m}$  – 30  $\mu\text{m}$ ) layer of solder. At solder joints, at least five materials are present: silicon (Si), silver (Ag), Cu, lead (Pb), and tin (Sn). Solders are primarily used to bond two or more components and must allow for expansion, contraction, heat dissipation, and electrical signal transmission [44]. Alloying elements improve the thermal and mechanical properties of solders which can have melting temperature ( $T_M$ ) as low as 90°C [45]. Solder are typically alloys chosen for their low melting point. In the electronics and solar industries, Sn<sub>60</sub>Pb<sub>40</sub> is a popularly used, inexpensive, and reliable solder with a low  $T_M$  of 188°C. This composition is close to its eutectic composition of Sn<sub>63</sub>Pb<sub>37</sub>, which has a  $T_M$  of 183°C [44]. A lamellar structure is formed when Sn<sub>60</sub>Pb<sub>40</sub> solder cools down which improves fatigue life [46]. Due to increased awareness of Pb toxicity, lead-free alternatives are being explored. Most of the solder bond degradation data being collected at various power plants and from accelerated tests conducted across the world is for Sn<sub>60</sub>Pn<sub>40</sub> solder systems.

Solder bonds degradation is mainly influenced by humidity and heat. In the presence of humidity, corrosion, and crack formation are possible degradation mechanisms. Under dry conditions, solder bonds experience thermomechanical fatigue (TMF) and intermetallic compound (IMC) formation (Fig. 15) [47]–[50] due to elevated fluctuating and static operating temperatures. Sources of thermal stress include heat generation during daytime

operation, daily temperature cycles, seasonal temperature cycles and cloud temperature cycles. Module components like glass, encapsulant, cells, and backsheet are affected by thermal stress [4]. The physical and chemical changes in the solder material and at the solder/metallization interfaces due to thermal stresses result in increased series resistance ( $R_s$ ), thus decreased fill factor (FF), and output power ( $P_{max}$ ).

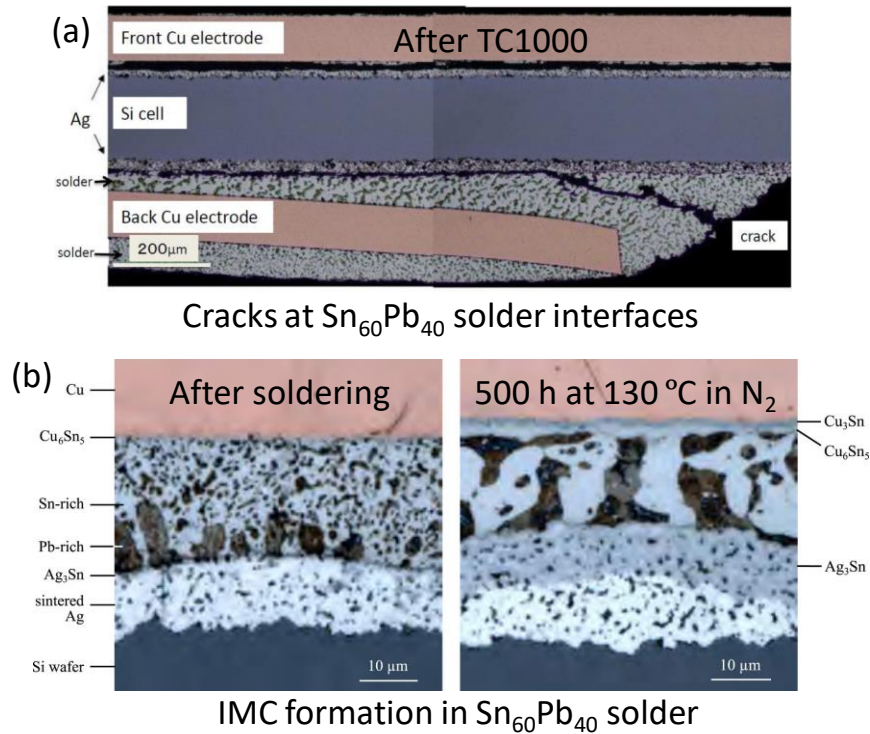


Fig. 15. SEM image showing effects of (a) TMF [51] and (b) IMC formation and phase coarsening induced due to thermal cycling and static elevated temperatures, respectively [52].

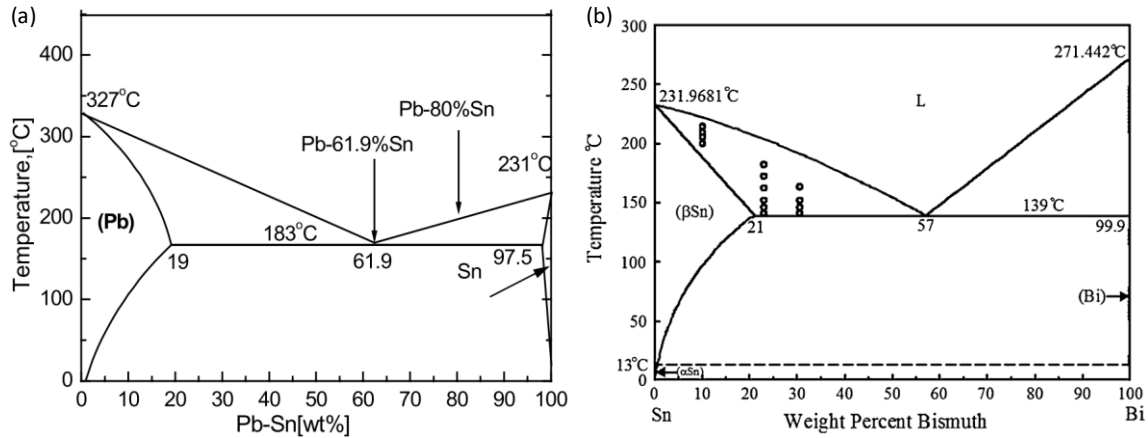


Fig. 16. Phase diagrams of (a) SnPb [53] and (b) SnBi [54] showing the main phases.

The  $\text{Sn}_{60}\text{Pb}_{40}$  alloy has a melting temperature of  $188^\circ\text{C}$  and the  $\text{Sn}_{42}\text{Bi}_{58}$  solder has a melting temperature of  $138^\circ\text{C}$ . In this work, the  $\text{Sn}_{60}\text{Pb}_{40}$ ,  $\text{Sn}_{62}\text{Pb}_{36}\text{Ag}_2$  and  $\text{Sn}_{42}\text{Bi}_{58}$  the systems are explored. Therefore the calculations and information presented pertain to these systems. A near-eutectic composition is chosen for solders due to their desirable mechanical and thermal properties.

In field operation, the module temperature can fluctuate drastically with the ambient temperature from day to night (depending on location). As the module warms up and cools down in the mornings and evenings, the solder bonds experience TMF [47]–[50]. TMF can be induced by cyclic thermal loads which introduces creep, shear, and tensile stresses leading to crack formation and growth [43]. The different metals and IMCs formed at the site of solder bonds experience non-uniform expansion and contraction owing to differences in coefficients of thermal expansion (CTE). The CTEs of different solders and IMCs are listed in TABLE II.

TABLE II: THERMAL PROPERTIES OF MATERIALS AT A SOLDER BOND.

Material	Coefficient of Thermal Expansion ( $\mu\text{m}\cdot\text{m}^{-1}\cdot\text{K}^{-1}$ )	Melting Temperature ( $^{\circ}\text{C}$ )
Si	2.6 <sup>a</sup>	1414 <sup>h</sup>
Ag	18.9 <sup>a</sup>	961 <sup>h</sup>
Sn	22.0 <sup>a</sup>	231 <sup>h</sup>
Pb	28.9 <sup>a</sup>	327 <sup>h</sup>
Cu	16.5 <sup>a</sup>	1085 <sup>h</sup>
Bi	13.4 <sup>a</sup>	271 <sup>h</sup>
Sn <sub>60</sub> Pb <sub>40</sub>	24.7 <sup>b</sup>	188 <sup>i</sup>
Sn <sub>62</sub> Pb <sub>36</sub> Ag <sub>2</sub>	25 – 28 <sup>c</sup>	180 <sup>j</sup>
Sn <sub>42</sub> Bi <sub>58</sub>	13.8 <sup>d</sup>	138 <sup>d</sup>
Cu <sub>3</sub> Sn	18.2 <sup>e</sup>	676 <sup>k</sup>
Cu <sub>6</sub> Sn <sub>5</sub>	16.3 <sup>f</sup>	415 <sup>k</sup>
Ag <sub>3</sub> Sn	20.0 <sup>g</sup>	261 <sup>l</sup>
Ag Busbar	10.4 <sup>m</sup>	Not applicable
Glass	9 <sup>n</sup>	Not applicable
EVA	180 <sup>n</sup>	90 – 120 <sup>o</sup>

<sup>a</sup>[55] <sup>b</sup>[50] <sup>c</sup>[56] <sup>d</sup>[57] <sup>e</sup>[58] <sup>f</sup>[59] <sup>g</sup>[60] <sup>h</sup>[61] <sup>i</sup>[52] <sup>j</sup>[62] <sup>k</sup>[63] <sup>l</sup>[64] <sup>m</sup>[65] <sup>n</sup>[66] <sup>o</sup>[67]

The effects of alloying metals to form solders are highlighted in the reduced CTEs and melting temperatures when compared to the elements. Due to the low melting temperatures (high homologous temperatures), a major failure mode of solder joints is creep [68]. Creep is a time dependent and permanent deformation occurring due to a constant stress [44]. The homologous temperature ( $T_H$ ) is the ratio of the material's temperature to the material's melting point in Kelvin:  $T_H = T / T_M$  and is useful in determining the creep rate. Creep is observed when the homologous temperature ( $T_H = T / T_{\text{MELTING}}$ , both in Kelvin) is above 0.4 to 0.5 [68], [69]. Solders experience creep even at 25 $^{\circ}\text{C}$  ( $T_H = 0.65$  for Sn<sub>60</sub>Pb<sub>40</sub>). There are three types of creep damage: cracks, void nucleation and growth, and microstructural degradation. Cracks are formed at lower temperatures whereas voids can be formed under most conditions. Localized microstructure weakening occurs when recrystallization localizes the creep strain [70]. It would be erroneous to overlook the effect of

microstructure on creep and fatigue lifetime of components [50]. Freshly solidified solder with a fine microstructure has better creep resistance than older solder with a coarser microstructure [71]. Coarsening of the phase microstructure and a reduction in the mechanical properties has been reported in solders kept at room temperature for 450 days [68]. Minimizing creep improves the fatigue life of solders [72]. The creep curve shown in Fig. 17 has three stages. In primary creep, the decrease in the strain rate observed is usually caused by work hardening which restricts deformation. In the second stage or steady-state creep, plastic deformation dominates for metals that are above  $T_H=0.5$ . This is the longest stage of creep. Strain hardening decreases the strain rate and deformation speed whereas the associated recovery and recrystallization accelerates the creep rate. The constant creep rate is a balance between strain hardening and recovery. In the third stage, the creep rate accelerates to result in failure/rupture which can be attributed to microstructural changes such as grain boundary separation, nucleation and growth of cracks, voids, cavities [44], [68].

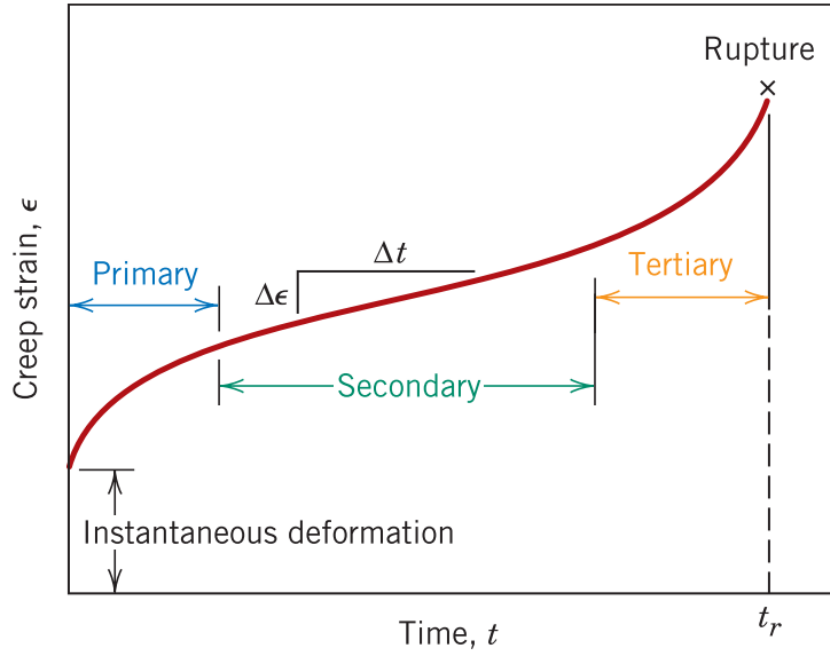


Fig. 17. A typical creep curve at constant stress and elevated temperature [44].

The x-axis of the creep deformation map can be determined calculating the  $T_H$  of the solders under consideration as shown in TABLE III.

TABLE III:  $T_H$  OF SOLDERS USED IN THIS WORK AT TEMPERATURES USED IN THERMAL CYCLING.

Temperature Condition	Homologous Temperature		
	Sn <sub>62</sub> Pb <sub>36</sub> Ag <sub>2</sub>	Sn <sub>60</sub> Pb <sub>40</sub>	Sn <sub>42</sub> Bi <sub>58</sub>
-40°C	0.51	0.51	0.57
0°C	0.60	0.59	0.66
25°C	0.66	0.65	0.73
85°C	0.79	0.78	0.87
95°C	0.81	0.80	0.90
105°C	0.83	0.82	0.92

To determine the y-axis ratio of  $\sigma / E$ , the stress between the different materials at the solder joint can be calculated as shown below [73].

$$\sigma = E\varepsilon \Rightarrow \sigma(T) = (\alpha_1 - \alpha_2) \left( \frac{E_2}{1 - \nu_2} \right) (T - T_i) \quad \text{Eq. 3}$$



where  $\sigma$  is the stress,  $E$  is the Young's Modulus,  $\varepsilon$  is the strain.  $\alpha_1$  and  $\alpha_2$  are the CTEs of the two layers,  $\nu$  is the Poisson's ratio,  $E_2$  is the Young's Modulus of layer 2,  $T$  is the temperature (K) and  $T_i$  is the initial temperature (K). Based on Eq. 3, the  $\sigma$  and the  $\sigma/E$  was calculated for the different materials at the solder joint. The  $\sigma/E$  range was calculated to be between  $1.39 \times 10^{-3} - 2.96 \times 10^{-3}$  which implies the solder joint can experience dislocation creep.

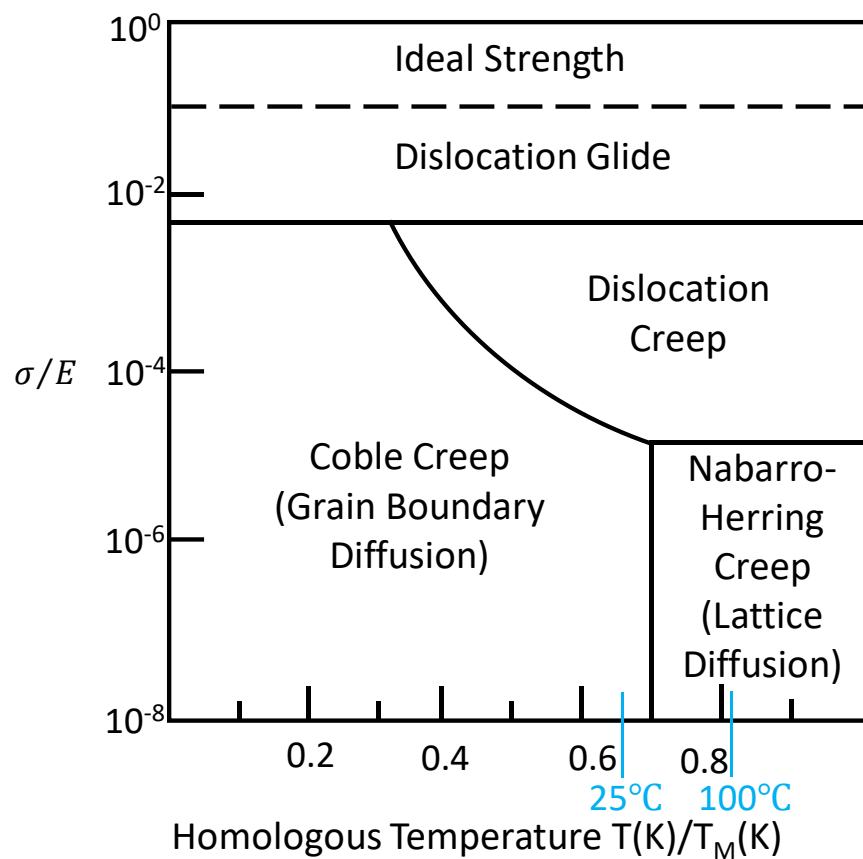


Fig. 18. Creep deformation map of solder alloys. With the operational temperature of solders being above  $0.65 T_H$ , the grain boundary, lattice diffusion, and dislocation creep is dominant [68].

The other degradation mode is driven by static elevated temperatures (during daytime) that cause phase segregation, grain coarsening, and IMC formation [52]. Diffusion driven IMC formation results in new brittle compounds that lead to cracking [51]. During the

soldering of cell interconnects, the elevated soldering temperatures induce the formation of a thin intermetallic layer (0.5  $\mu\text{m}$  to 2  $\mu\text{m}$ ) between the Cu and the Sn [5]. Exposure to elevated temperatures results in IMC growth during operation. A thicker IMC layer accumulates creep and affects the thermo-mechanical reliability of solder joints [72]. IMC formation when combined with TMF, leads to cracking and makes for a fatigue environment [46], [51]. Phase segregation occurs to reduce the overall system energy and reach equilibrium. Grain coarsening at solder bonds is induced by static thermal aging at elevated temperatures and accelerated by cycling thermal testing. The process hardens the solder joint and significantly affects creep [50]. Fick's law, which dictates the diffusion of metal atoms at the solder bonds that result in IMC formation, is dependent on time, distance, and the diffusion constant.

$$\bar{x}^2 = 2Dt \text{ where } D = D_0 \exp\left(-\frac{Q}{RT}\right) \quad \text{Eq. 4}$$

In this equation,  $x$  is the IMC layer thickness,  $t$  is the time, and  $D$  is the diffusion constant. Each solvent-solute pair has a diffusion coefficient. The new compounds formed are brittle and lead to cracking. The different IMCs formed experience non-uniform expansion and contraction owing to differences in CTEs and can cause adhesion loss [74]. A single phase matrix with a fine dispersion of lattice pinning particles is most beneficial to withstand fatigue since it would undergo least microstructural change [46].

Trace amounts of silver is added to the standard Sn<sub>60</sub>Pb<sub>40</sub> solder to improve its mechanical properties to suppress grain coarsening and limit the diffusion of Ag from the

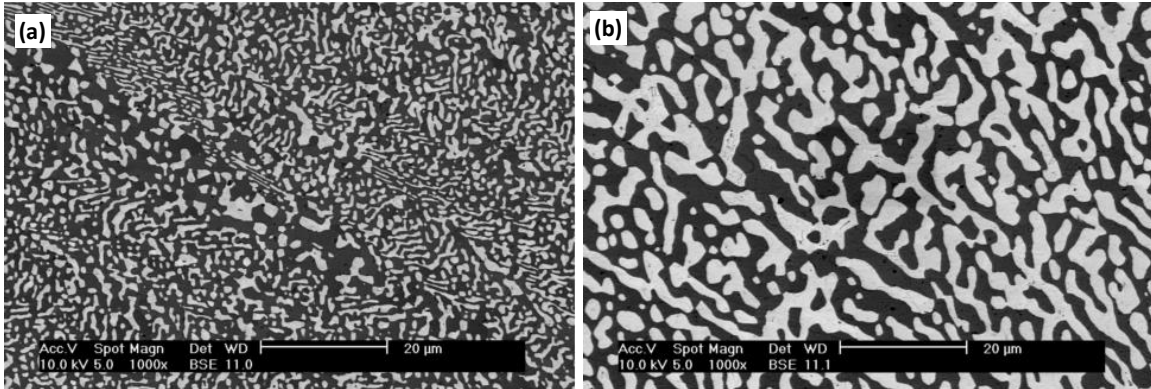


Fig. 19. Optical micrographs showing grain coarsening in (a) sample quenched in liquid nitrogen. (b) by aging at 150°C for 15 hours, the grain size increased significantly [75].

cell to the solder [52], [76], [77]. The activation energy ( $E_a$ ) for dissolution of Ag (from the busbar) in  $\text{Sn}_{60}\text{Pb}_{40}$  solder is 0.65 eV whereas that for  $\text{Sn}_{62}\text{Pb}_{36}\text{Ag}_2$  solder is 1.02 eV [77]. Despite the advantages of adding Ag, due cost considerations and a lack of durability concerns,  $\text{Sn}_{60}\text{Pb}_{40}$  is the popular solder choice for module manufacturers. During soldering of  $\text{Sn}_{60}\text{Pb}_{40}$ , a 0.5  $\mu\text{m}$  thin layer of  $\text{Cu}_6\text{Sn}_5$  and  $\text{Ag}_3\text{Sn}$  are formed between the Cu-Sn and the Ag-Sn interfaces, respectively. After 500 hours at 130°C, the  $\text{Cu}_6\text{Sn}_5$  layer had grown to 1.5  $\mu\text{m}$  whereas the  $\text{Ag}_3\text{Sn}$  layer had grown to 10  $\mu\text{m}$  [52]. Creep, IMC formation and TMF are detrimental to the reliability of the solder-metallization system in modules. It is important to study the  $\text{Sn}_{60}\text{Pb}_{40}$  solder,  $\text{Sn}_{62}\text{Pb}_{36}\text{Ag}_2$  solder,  $\text{Sn}_{42}\text{Bi}_{58}$  solder systems due to their popularity in usage.

To induce TMF and creep, a test with a cyclic thermal profile with a high  $\Delta T$  is most suited. The cycling temperatures causes non-uniform expansion and contraction of the materials at the site of the solder bond. To induce IMC formation, solder joints are aged isothermally for extended periods of time. With higher temperatures, more diffusion can

be seen. However, the testing conditions should be maintained such that runaway mechanisms are not induced.

One of the ways to detect the infant mortality issues in fresh PV modules, cell interconnect ribbons, and solder bonds is through tests defined in IEC 61215 (design qualification and type approval standard for terrestrial PV modules) [36]—thermal cycling and damp heat (TC200 and DH1000). Correlating the TC200 or DH1000 test durations of fresh modules directly to years of field exposure is not practically possible. This is because life-limiting degradation modes a module experiences in the field are dependent on several factors which are influenced by the wear out properties of materials, their interfaces, and field-specific conditions—and not just the module design itself. When field-exposed modules undergo accelerated testing, the normal-life degradation experienced thus far moves to wear-out failure degradation. Field-specific end-of-life (last 5 – 10 years of a module’s life) degradation and failure modes can be replicated with accelerated stress testing of modules that have already been exposed to specific field conditions. The  $E_a$  calculated from accelerated stress testing of fresh modules pertains to early-life and normal life degradations and not end-of-life degradations.

The  $E_a$  for TMF and IMC formation can be calculated from the slope of an Arrhenius plot with the y-axis being TMF damage (0.12 eV) [48], creep (0.46 eV) [50], and IMC layer thickness measured via electron microscopy (0.89 eV – 1.34 eV) [52]. Each data point on the Arrhenius plot represents solder bond degradation at a specific temperature (x-axis). Based on DH1000 testing, an  $E_a$  value of 0.89 eV has been calculated by Kimball [78] for solder bond degradation.

## CHAPTER 3: EXPERIMENTAL METHODOLOGY

### 3.1 Characterization Methods

TABLE IV: LIST OF MODULE-LEVEL CHARACTERIZATION TECHNIQUES USED ALONG WITH THEIR SIGNIFICANCE

MODULE LEVEL	Method	Information Obtained	Significance	Relevant to	
				Encapsulant Browning	Solder Bond Degradation
	UV Fluorescence (UVF) imaging	Extent of encapsulant browning	Quickest way to detect encapsulant browning and delamination	✓	
	Light I-V (LIV)	Electrical performance parameters	Electrical parameters of the module for degradation rate determination	✓	✓
	Dark I-V (DIV)	Diode parameters and parasitic resistances	Enables calculation of series and shunt resistances		✓
	Electroluminescence (EL) imaging	Dead cell areas and poor metallization	Identifies electrically inactive and less-active areas		✓
	Indoor Infrared (IR) imaging	Heat profile of the module with injected carriers	Reveals hotspot issues in dark conditions		✓
Outdoor IR imaging	Heat profile of the module with generated carriers	Reveals hotspot issues under light conditions	✓		

	Colorimetry	Yellowness Index (YI)	Quantifies the intensity of encapsulant browning	✓	
	<b>Method</b>	<b>Information Obtained</b>	<b>Significance</b>	<b>Relevant to</b>	
				<b>Encapsulant Browning</b>	<b>Solder Bond Degradation</b>
	Spectral Reflectance	Light reflected from the glass, encapsulant, and cell is measured	Changes in reflectance can be indicative of the reflectance status of the encapsulant and interfaces	✓	
	Scanning Electron Microscopy (SEM)	Highly magnified images, layer thicknesses, and areas	Microstructural features indicate changes in morphology		✓
	Energy Dispersive X-ray Spectroscopy (EDXS)	Compositional analysis through line-scans and area-maps	Formation of intermetallic compounds and phase segregation track degradation in solder		✓

TABLE V: LIST OF CELL-LEVEL CHARACTERIZATION TECHNIQUES USED ALONG WITH THEIR SIGNIFICANCE

C E L L  L E V E L	Method	Information Obtained	Significance	Relevant to	
				Encapsulant Browning	Solder Bond Degradation
	Quantum Efficiency (QE) Measurements	Number of carriers collected divided by photons injected	The local cell QE can help deconvolute cell-level/module-level degradation mechanisms	✓	✓
	Solar Simulator	LIV parameters of $I_{sc}$ , $V_{oc}$ , $I_{mp}$ , $V_{mp}$ , FF, and $P_{max}$	Individual cells' electrical data within a module could deconvolute packaging issues	✓	
		DIV parameters of $R_s$ and $R_{sh}$	The $R_s$ and $R_{sh}$ of cells can be indicative of solder bond degradation		✓

### 3.1.1 Ultra-violet Fluorescence (UVF) Imaging

Encapsulant browning is difficult to detect visually unless severe. The quickest method to objectively detect encapsulant browning is through UVF imaging. This method was first reported in 2000 [79]. The chromophores formed in the encapsulant fluoresce when UV light between 375 nm – 395 nm is incident. The chromophores absorb the UV light and get excited. They emit light in the visible range when they get de-excited as shown in Fig. 20.

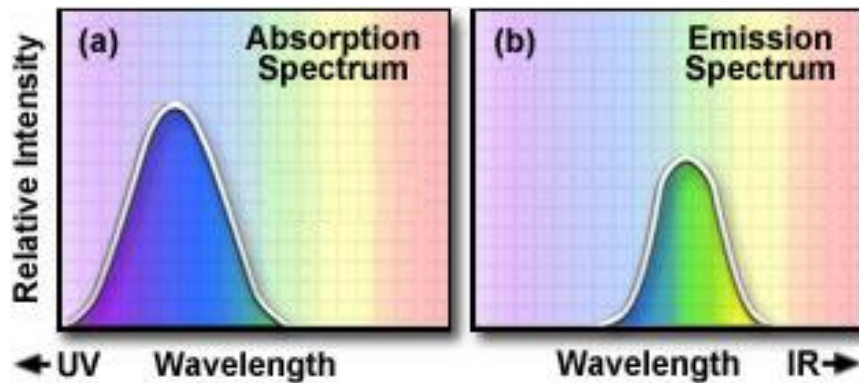


Fig. 20. Schematic representing the (a) absorption and (b) emission spectra of chromophores [80].

Fig. 21 shows a schematic of the UVF imaging set-up along with an image of the set-up at our lab. Two arrays of 15 UV Beast lamps each were angled at  $45^\circ$  towards the module surface to minimize any glare/reflection from the module. The visual photograph was taken perpendicular to the module plane. The set-up provides a uniform and bright light source, making UVF imaging fast, non-contact and low cost. The system can be modified to image large areas in PV power plants.



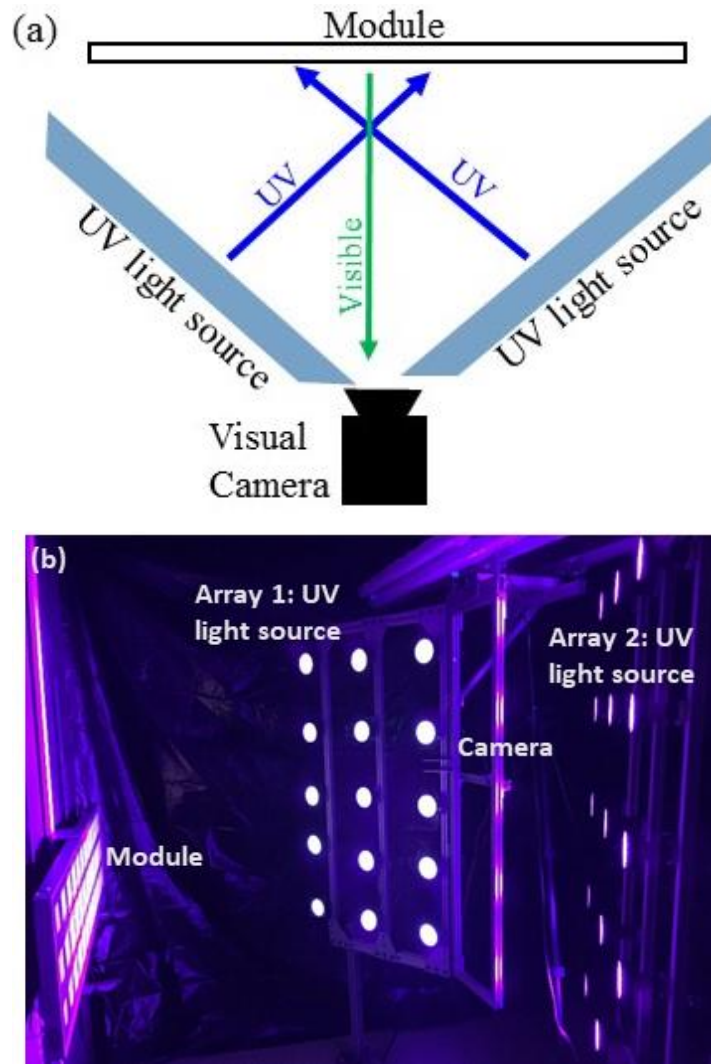


Fig. 21 (a) Schematic of UVF imaging set-up with two UV light source arrays angled towards the module. The module emits visible light. (b) Photograph of the set-up with the UV arrays.

### 3.1.2 Light current-voltage (LI-V) Curve Tracing

Light I-V curves are the most important tool to identify the reliability and durability issues along with other installation issues. In addition to performance parameters, the shape of the IV curve provides information about the status of the module. In Fig. 22, the different dotted lines are indicative of issues with the module/string.

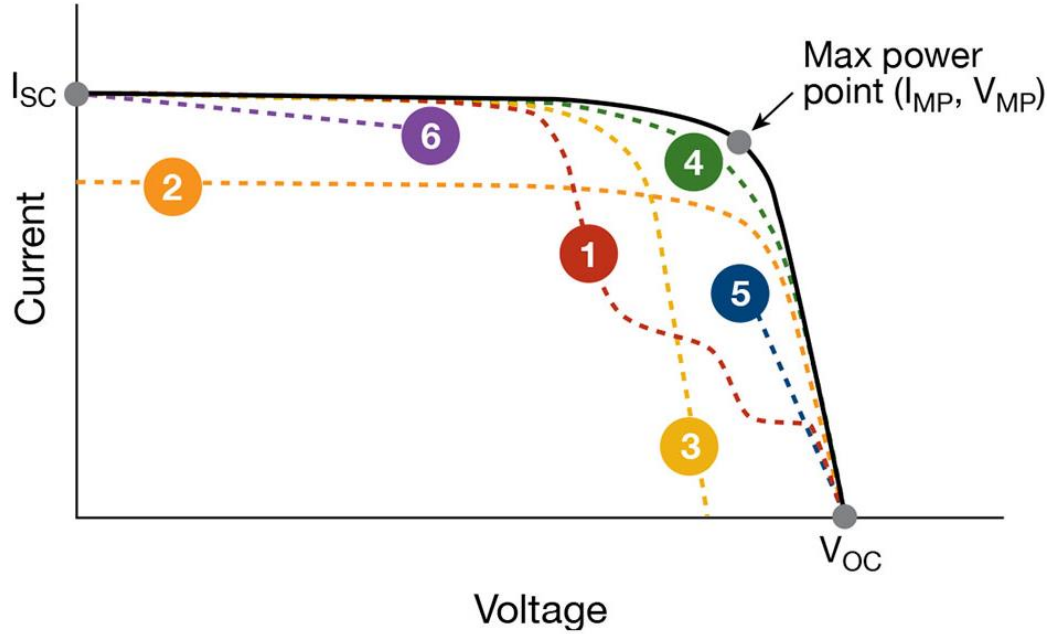


Fig. 22 A typical IV curve with some common anomalies (dotted lines) highlighted in a graph by Solmetric [81].

TABLE VI: INTERPRETATION OF I-V CURVE SHAPES BASED ON FIG. 22

Curve	Interpretation
1	Partial shading, mismatched modules, cracked cells, non-uniform soiling
2	Low $I_{sc}$ that can be caused by from uniform soiling
3	low $V_{oc}$ that can be caused by shorted bypass diode
4	Rounder knee that could indicate cell degradation
5	Low $V_{mp}/V_{oc}$ ratio that can be caused by increased series resistance
6	Low $I_{mp}/I_{sc}$ ratio that can be caused due to slight current mismatch in modules, tapered shading, or soiling across modules

For modules in this work, I-V curves were taken at different module temperatures to aid the calculation of temperature coefficients. The modules were first cooled to about 15°C and then placed on a two-axis tracker facing the sun. As the module temperature increases, a series of curves were taken at irradiances greater than 800 W/m<sup>2</sup>. Two calibrated reference cells were used as irradiance sensors and mounted coplanar to the test modules. The interpolation method of translation mentioned in the Solar ABCs report was used [82]. I-V curves were recorded from 20°C – 35°C to obtain temperature coefficients and the

curve closest to 25°C was translated to STC. For all IV curves in this work, a DayStar IV curve tracer, a calibrated reference cell from PV Measurements, and another calibrated reference cell from IMT Solar were used with IVPC software to obtain the curves. T-type thermocouples with an accuracy of  $\pm 1^\circ\text{C}$  were used to measure the module and ambient temperature.

### 3.1.3 Dark Current-Voltage (DI-V) Curve Tracing

Dark I-V characterization sheds light on the junction quality, grid, and contact resistances of a module [83].

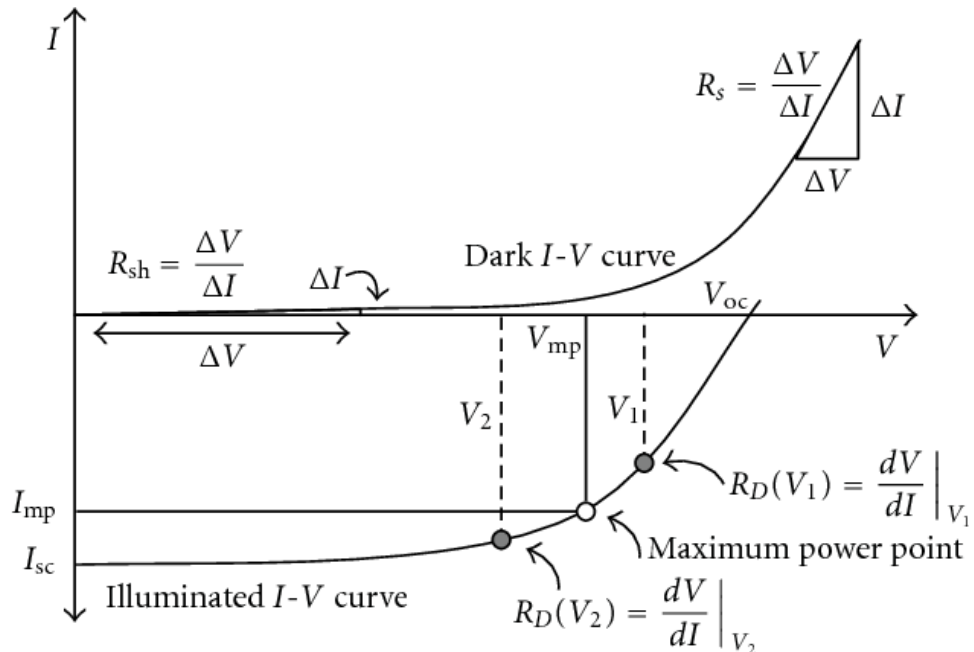


Fig. 23. Schematic of dark I-V and light I-V [84]. The inverse slope at  $V_{oc}$  gives the series resistance ( $R_s$ ) and that at  $I_{sc}$  gives shunt resistance ( $R_{sh}$ ).

The series resistance ( $R_s$ ) and shunt resistance ( $R_{sh}$ ) of a module can be calculated as the inverse of the slopes near the open-circuit voltage ( $V_{oc}$ ) and the short-circuit ( $I_{sc}$ ), respectively (Fig. 23). The module is connected in forward bias to a current-limited DC power supply. Current equivalent to the module  $I_{sc}$  is set on the power supply and the

voltage is increased slowly. A Kepco power supply (KLP 75-33) was used with a current shunt to measure the current flowing through the module in terms of a voltage drop.

#### 3.1.4 Electroluminescence (EL) Imaging

Electroluminescence imaging is based on radiative recombination of excited charge carriers in the cells. It allows for detection of defects such as cracks, metallization degradation, and junction shunting that are not seen in the visual photographs (Fig. 24). Current equivalent to the module  $I_{sc}$  was injected into the module in forward bias with a current-limited DC power supply (Kepco KLP 75-33). Images from an NIR sensitive Sensovation camera (HR-830) were obtained with 60s – 180s exposure.

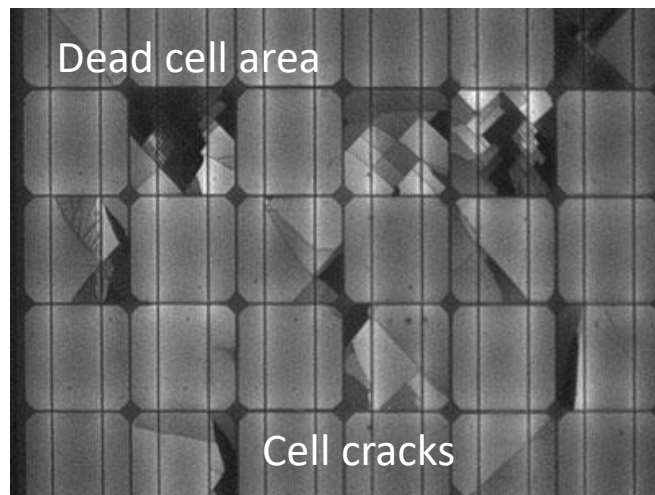


Fig. 24. Typical EL image showing cell cracks, isolated dead-cell regions, and cell issues [85].

#### 3.1.5 Infra-red (IR) Imaging

IR imaging allows to detect defects such as hot cells and hot spots that are not visible otherwise (Fig. 25). The difference between indoor and outdoor IR imaging is in the direction of electron flow. To take indoor IR images, current equivalent to the  $I_{sc}$  was

passed through the modules for 5 minutes after which the image was taken with an infrared camera. For outdoor IR, the short-circuited module is placed in the sun and images are taken after 5 minutes. Here, the electrons generated in the cell and go into the metallization of the cell. For both types of IR imaging, Fluke Ti55 was used.

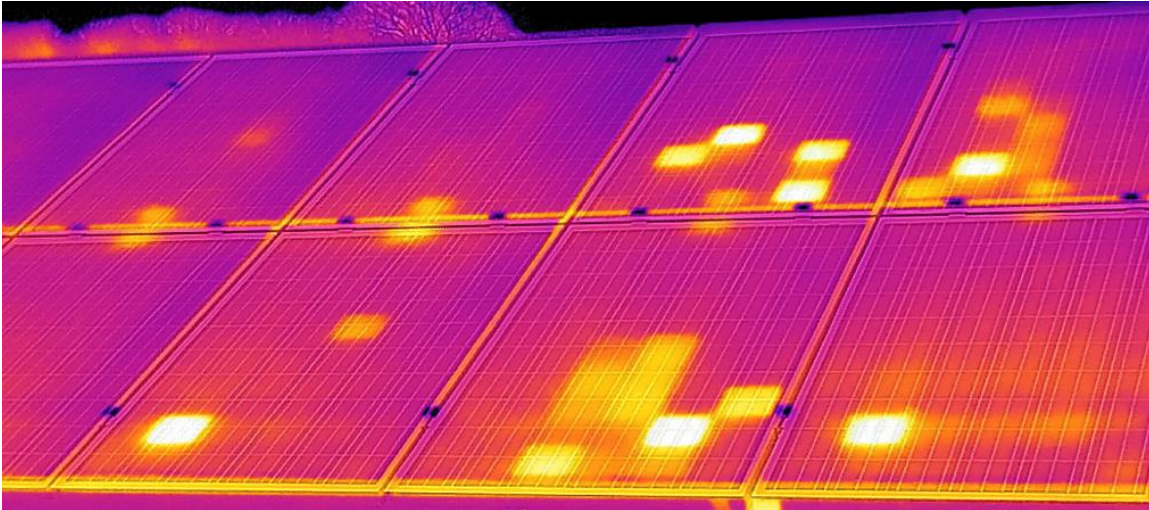


Fig. 25. IR imaging highlighting relatively hotter cells that could indicate issues with cell metallization [86].

### 3.1.6 Colorimetry

Color can be measured as a combination of its individual components by a technique known as colorimetry. The most common example is colors expressed as varying levels of red, green, and blue on a scale between 0 - 255. Black is (0,0,0) whereas white is (255, 255, 255). Other common color spaces include CIE, HSV, XYZ, Lab, and Lch. In this work, a yellowness index (YI) was calculated by the colorimeter based on the XYZ values as listed below (Fig. 26).

$$YI = \frac{(100(C_x X - C_z Z))}{Y} \quad \text{Eq. 5 [88]}$$

An X-Rite Ci60 series colorimeter was used to measure the YI after being calibrated with a black and a white reference.

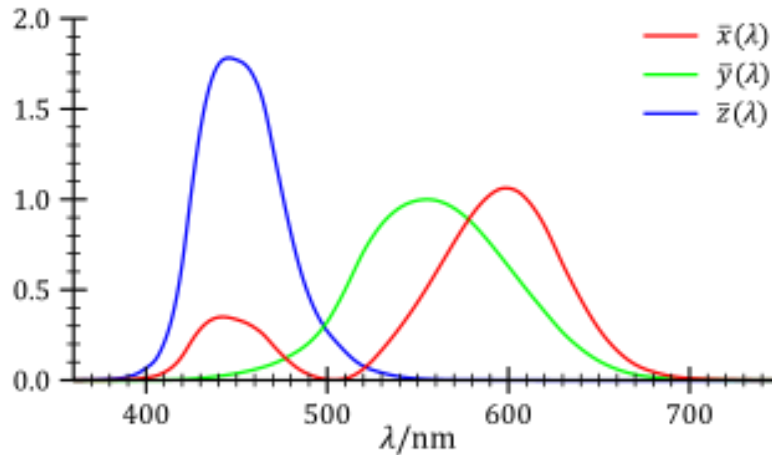


Fig. 26. Components of the X, Y, and Z color space [89].

### 3.1.7 Spectral Reflectance Measurements

Spectral reflectance measurements serve as an indicator for light being reflected from the solar cell through the glass and encapsulant. Reflectance measurements were obtained for the same spots as that of the QE measurements. Reflectance was measured using a handheld UV-Vis-Near IR Spectrophotometer of ASU-PRL on the various spots of each module. Reflectance plots were obtained for each of the pre-determined spots by taking the median of ten measurements to reduce the error margin. These measurements provide us with a relative reflectance across the UV-Vis-Near IR spectrum giving us information on spot-dependent browning level and  $I_{sc}$  drop. A sharp drop below 400 nm is indicative of

presence of cerium oxide material in the glass, which acts as a UV absorber reducing the browning rate of encapsulant.

### 3.1.8 Scanning Electron Microscopy and Energy Dispersive X-ray Spectroscopy

Optical microscopes facilitate magnified imaging of samples but the feature size detectable ( $\sim 0.2 \mu\text{m}$ ) is limited by the wavelength of light. Since scanning electron microscopes (SEM) use an electron beam, much smaller feature sizes can be imaged (sub nanometer). SEM is vital in examining materials at a micro-scale. Changes in bulk material properties can be linked to microstructural changes. Once prepared by mounting and polishing, samples are imaged by a focused electron beam rastering the area of interest.

Energy dispersive X-ray spectroscopy (EDXS) is a method of detecting elements in samples. The primary electrons from the rastering beam knock out electrons from the atoms of the sample emitting X-rays. A detector is able to identify the atoms from the sample based on X-ray energy levels unique to elements. EDXS surface maps can be obtained by rastering the beam across the sample. By calibrating the X-ray emission to standard samples, the atomic composition analysis can be performed. Imaging and EDXS compositional analysis were performed on a ZEISS AURIGA microscope, equipped with an Oxford Instruments X-Max<sup>N</sup> spectrometer.

### 3.1.9 Quantum Efficiency (QE) Measurements

The efficiency of a module is dictated by the cell with lowest efficiency. Even within a cell, local efficiency differences can be identified by quantum efficiency (QE) measurements. QE, being the ratio of electrons collected to the incident photons, reveals the status of the measurement spot on the cell with respect to individual wavelengths (Fig.

27). The equipment available at ASU-PRL is a one of a kind that allows the QE of a cell within a module to be measured without the need of cutting backsheet to access the cell individually.

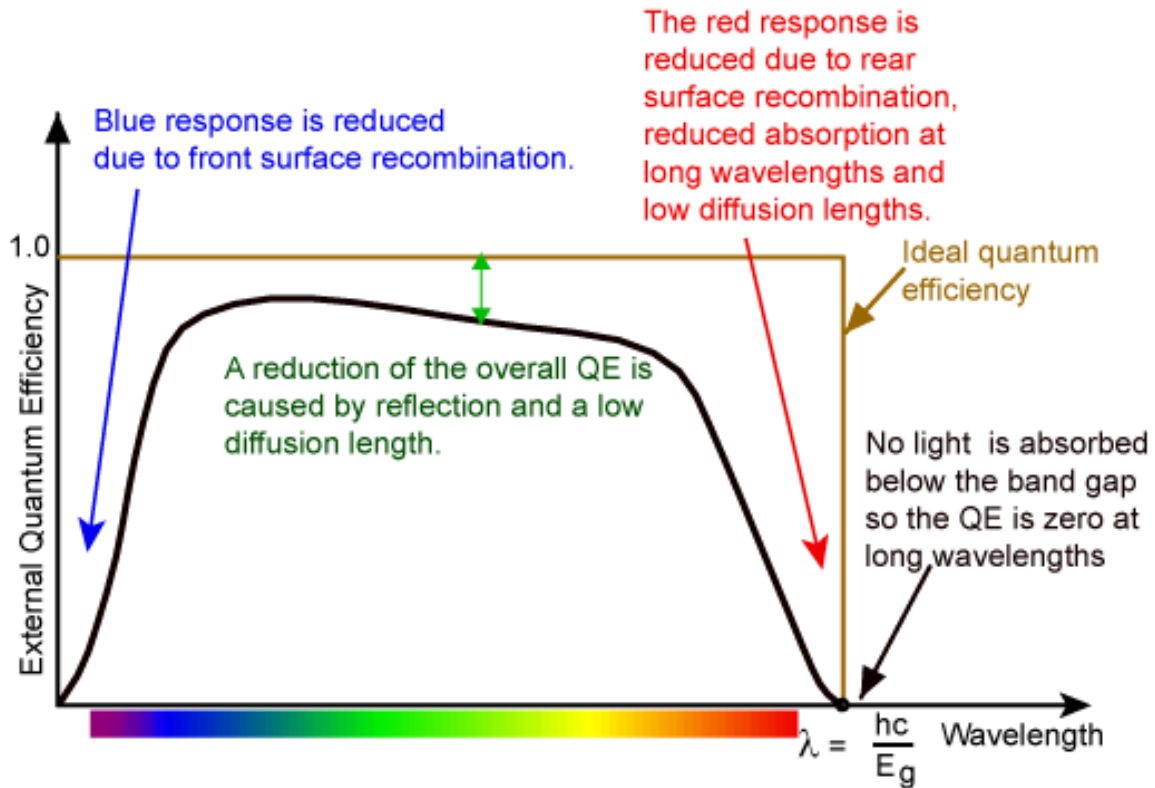


Fig. 27. Representative QE curve of a typical solar cell [87].

When the low power density monochromatic beam spot is on a specific cell in the module, that cell is forward biased, but the surrounding cells are reverse biased. To counter the reverse biasing, a light bias of  $200\text{W}/\text{m}^2$  is used to forward bias the surrounding cells. This in turn results in the cell of interest being reverse biased due to very low power density of the monochromatic light. To counter the reverse biasing of the cell of interest, a bias voltage is applied across the whole module. This causes the whole module to be in forward bias allowing the electricity generated from the spot to be measured. The current generated



in the module due to the bias lights is constant. A chopping wheel is used in the pathway of the beam. The electricity generated from the beam in the cell of interest to be discrete allowing for easier identification. From this, the QE can be calculated as the number of photons incident on the module is known.

### 3.1.10 Cell-level LI-V and DI-V Measurements

The performance of a module is limited by the least performing cell in the string. For individual cells within modules and 9-cut-cell samples, I-V measurements were obtained with a class AAA PV Measurements solar simulator as seen in Fig. 28.

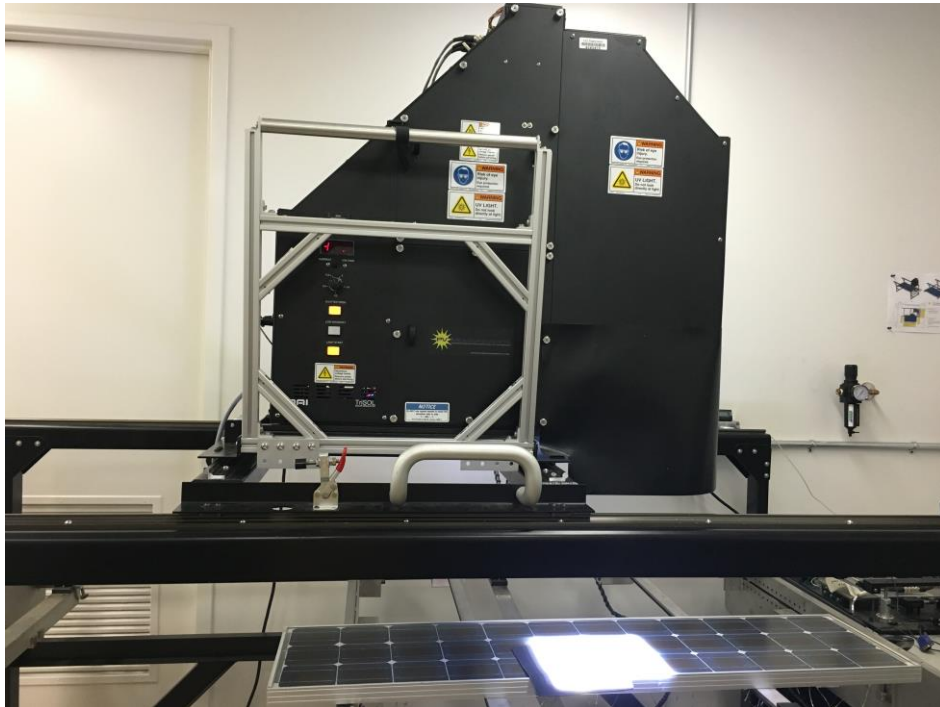


Fig. 28. Image of the class AAA continuous solar simulator at PRL in use. The incident beam is centered on the cell.

A method of individually accessing multiple cells within a module was used in this work. While invasive, the method does not damage the cell or the module. It increases the number of data points for each condition set leading to statistical significance. The ribbon

between two cells was identified and marked on the backsheet. The backsheet and the back-EVA layer of the module was cut with a scalpel and melted away with a soldering iron to reveal the cell interconnect. The cell interconnects, after being cleaned by flux, were soldered to ribbons as seen in Fig. 29b-1. With two busbars in each cell, two ribbons were soldered. After allowing for strain relief (Fig. 29b-2), these ribbons were in turn soldered to each other to form one point (Fig. 29b-3) for consistency in all cell-level measurements. The exposed areas were then sealed with silicone sealant to prevent humidity ingress.

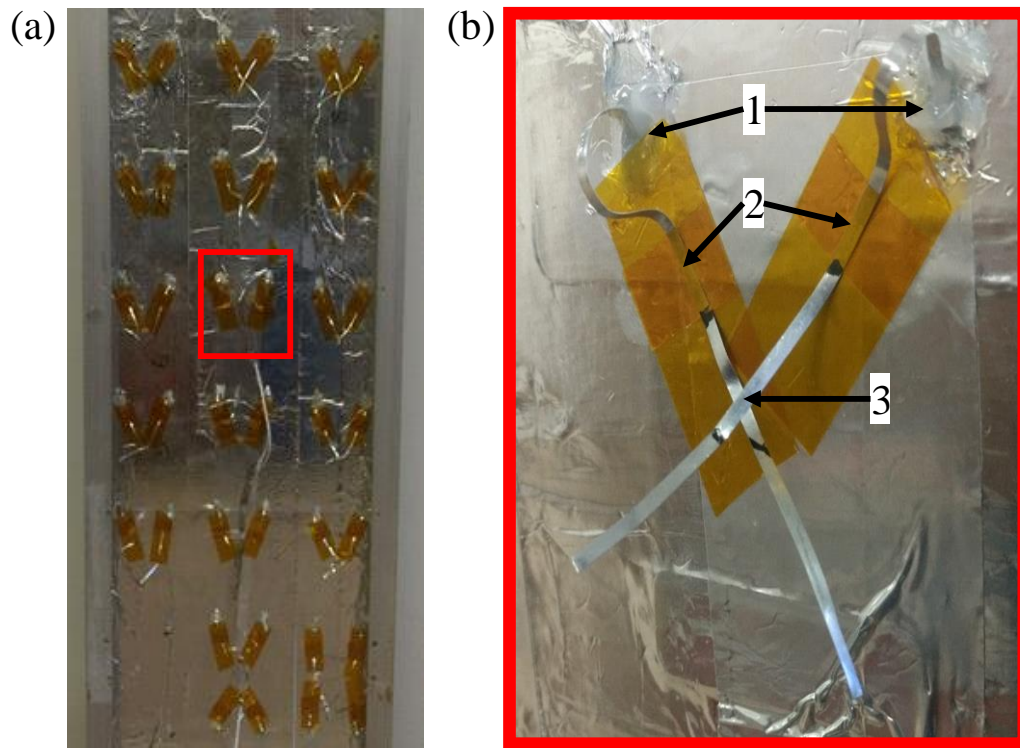


Fig. 29. (a) Image of the backside of a module with cells cut. (b) Close up of one cell where (1) the Al tape, backsheet, and back EVA were cut to access the cell interconnect. After soldering the ribbons, the site was covered with silicone paste to prevent moisture ingress. (2) The soldered ribbons were taped down on Kapton tape (used for insulation) to give strain relief. (3) The two positive/negative ribbons from each cell were soldered together to have one point used for consistent measurements.

### 3.2 Activation Energy Calculation

Models used in calculations and analyzing the data obtained are presented here. The Arrhenius model was used extensively in this work to calculate the  $E_a$ .

#### 3.2.1 Arrhenius Model

Every temperature dependent chemical reaction has a minimum required energy for completion known as the activation energy ( $E_a$ ). Many chemical reactions are exponentially dependent and can be expressed as

$$\text{Arrhenius model: } f(T) = A \exp\left(-\frac{E_a}{kT}\right) \quad \text{Eq. 6}$$

where  $k$  is the Boltzmann constant,  $A$  is the pre-exponential factor,  $E_a$  is the activation energy and  $T$  is the absolute temperature. The  $E_a$  can be calculated from the slope of the  $\ln$  (degradation rate) against inverse absolute temperature [90], [91] (Fig. 30). Based on the Arrhenius model, the  $E_a$  for encapsulant browning and solder bond degradation can be calculated. Each data point represents the natural log of the average of  $I_{sc}$  or  $R_s$  data from multiple cells in multiple temperature zones within a single module.

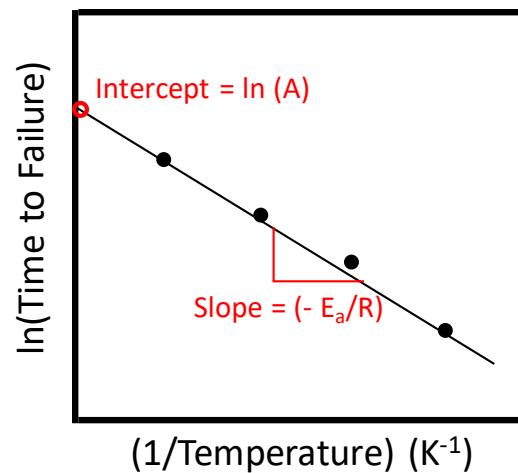


Fig. 30. Representative Arrhenius plot from which the activation energy can be calculated.

### 3.3 Qualification tests as prescribed in IEC 61215

The qualification tests regarding photovoltaic module reliability in the International Electrotechnical Commission (IEC) standards [92] identify design, material, and process flaws, which lead to infant mortality failures.

#### 3.3.1 UV Pre-Conditioning [92]

The standard mandates a 15 kWh/m<sup>2</sup> UV exposure on the glass superstrate that aims at testing the interfacial bonds between the glass, encapsulant, and the cell. The module temperature should be 60°C ± 5 during the test with the irradiance between 280 nm – 400 nm not to exceed 250 W/m<sup>2</sup>. Between 3% - 10% of the wavelength band should be in the 280 nm – 320 nm range.

#### 3.3.2 Thermal Cycling (TC200) [92]

Thermal cycling aims to identify issues with the module metallization. A cycle has the following features i) goes from a low temperature of -40°C till a high of 85°C to mimic extreme temperatures, ii) has a minimum dwell time of 10 minutes at -40°C and at 85°C to ensure thermal equilibration, iii) injected I<sub>sc</sub>-equivalent current to mimic normal operating conditions, and iv) has a maximum cycle time of 6 hours, and v) a maximum ramp rate of 100°C/hour to ensure realistic ramping rates and cycling times.

### 3.4 Accelerated Stress Testing to Induce Encapsulant Browning and Solder Bond

#### Degradation in Field-Aged Modules

##### 3.4.1 Studying Encapsulant Browning in Field-Aged Modules

Encapsulant browning is a degradation mechanism that can be hard to detect visually unless severe. To study it, encapsulant browning needs to be replicated in controlled conditions. The three main factors that affect encapsulant browning are UV light, humidity, and temperature. In our approach, multiple experiments were carried out with field-aged modules and fabricated coupons to investigate the effect of each of the factors on encapsulant browning. The overall goal of the project was to determine the acceleration factor for UV tests that would help predict browning rates for other climates.

##### Methodology

The first step in this project was to create databases with which the results of the experiments could be compared. Two databases—an accelerated testing and a field test—were curated with the help of the Dr. Dirk Jordan of the National Renewable Energy Laboratory (NREL) in Colorado. The databases are available for public access on the ASU PRL website. The **accelerated testing** database contains information of 236 modules from 29 manufacturers that underwent TC200 and DH1000 tests. The **field test database** includes information from two climate types (hot dry and cold dry) for close to 1500 modules. The field database also includes 6100 data points curated by NREL from 71 literature sources. Only data from sites older than 10 years have been considered due to two reasons: to decrease the influence of nameplate tolerances on degradation rate

calculation and to decrease the measurement uncertainty on degradation rate calculation. The parameters/elements present in the accelerated and field test databases are listed below.

TABLE VII: SUMMARY OF THE FIELDS OF THE ACCELERATED AND THE FIELD DATABASES. GREY BOXES INDICATE INAPPLICABLE OR UNAVAILABLE DATA

	Element/Parameter	Accelerated database		Field database
		DH1000	TC200	ASU
1	Accelerated test name	✓	✓	
2	Percent degradation after stress test	✓	✓	
3	Annual degradation rate in the field			✓
4	Technology type	✓	✓	✓
5	Construction type	✓	✓	✓
6	Field classification name			✓
7	Nameplate rating data	✓	✓	✓
8	Measurement uncertainty	✓	✓	✓
9	Nameplate deviation from measured data	✓	✓	
10	Manufacturer name	✓	✓	✓
11	Manufactured year	✓	✓	✓
12	Tested year	✓	✓	✓
13	Installed year			✓
14	Visual defect name	✓	✓	✓
15	Framed/ frameless	✓	✓	✓
16	Encapsulant type	✓	✓	✓
17	Backsheet type	✓	✓	✓

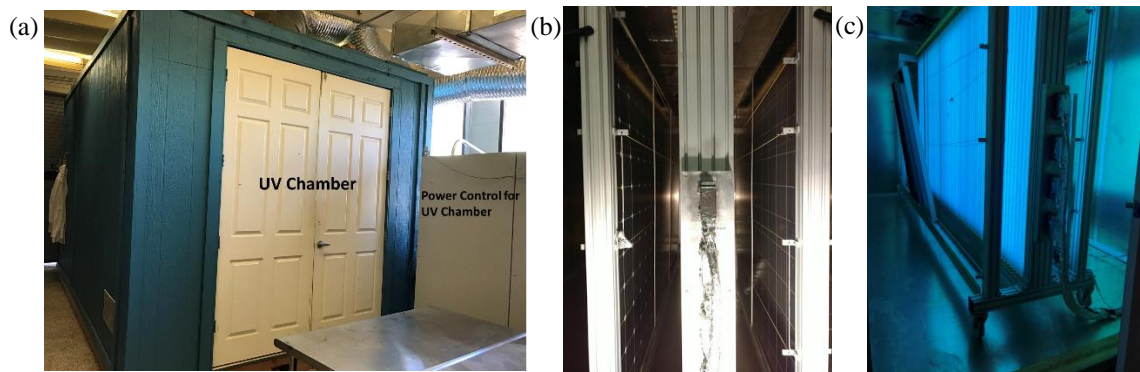


Fig. 31. (a) Photograph of the outside of the UV chamber along with the power controller. Photograph inside the UV chamber (b) without the UV lamps on and (c) with the UV lamps on.

ASU-PRL procured and commissioned a walk-in UV chamber to enable exposure of commercial sized modules to UV light as shown in Fig. 31. To study browning in the end-of-life stages of modules, field-aged modules were exposed to UV light to induce further browning. For the accelerated UV exposure, modules from two manufacturers were considered: MSX 60 of Solarex and M55 module of Siemens. The polycrystalline Si MSX 60 modules and the monocrystalline Si M55 modules were exposed in Mesa, Arizona for 21 and 18 years, respectively. Three Solarex modules (MSX 60, exposed in Arizona for 21 years), three Siemens modules (M55, exposed in Arizona for 18 years) were obtained. One fresh module of the same construction from each manufacturer were also included in the test. The eight modules that were exposed to  $450 \text{ kWh/m}^2$  of UV dosage can be divided into two categories based on manufacturer. Each category had a fresh module and three field-aged modules. All field-aged modules had aluminium (Al) tape on the backsheet to prevent oxygen diffusion and hence oxygen photobleaching. To measure the module temperature, K-type thermocouples ( $\pm 2^\circ\text{C}$ ) were placed on the module backsheet below the Al tape and the foamboard as shown in Fig. 32.

All eight modules were characterized with various non-destructive methods before, during, and after exposure to  $450 \text{ kWh/m}^2$  of UV dosage between 300 nm – 400 nm at elevated temperatures. The Qualification Plus guidelines suggests  $225 \text{ kWh/m}^2$  of UV dosage for encapsulants. Double the recommended exposure was chosen for our experiments to truly bring out end-of-life failure mechanisms.

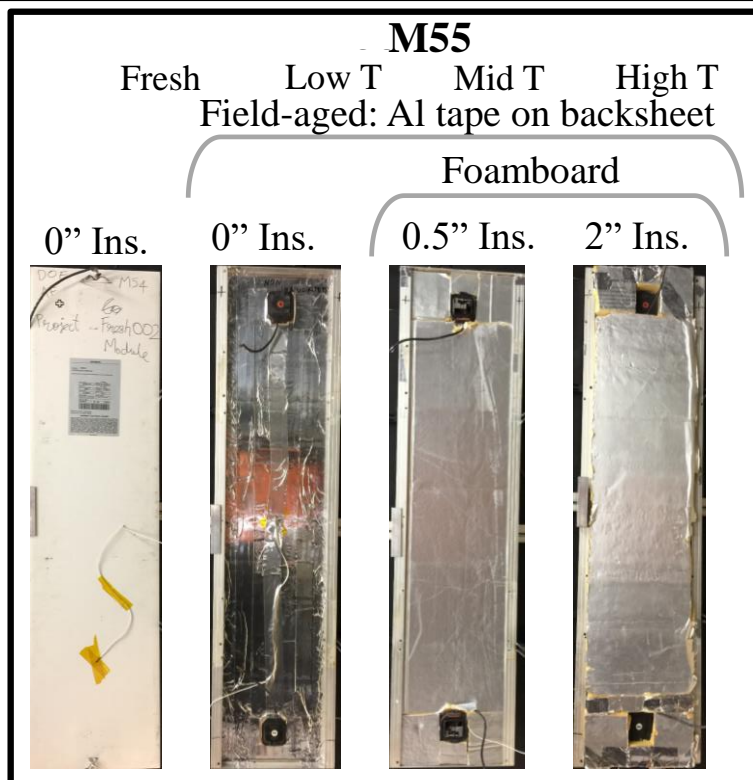
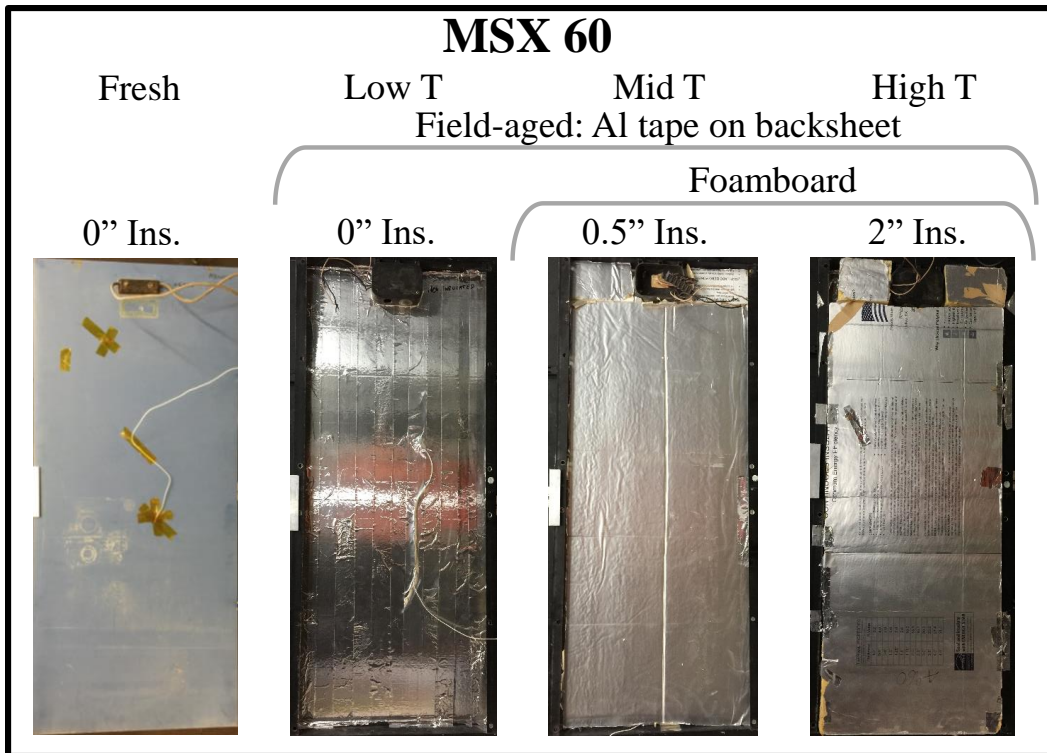


Fig. 32. Images of the prepared (a) MSX 60 and (b) M55 modules that underwent 450 kWh/m<sup>2</sup> of UV exposure.



To maintain consistency throughout the project, a system of identifying the cells and spots was established. For all the characterizations carried out, the junction box was consistently placed to the right. An alphanumeric grid was used to identify the cells as seen in Fig. 33.

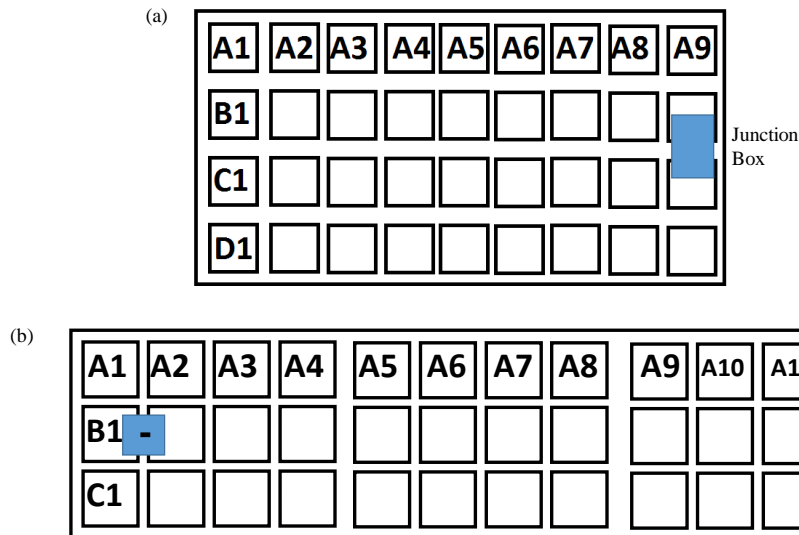


Fig. 33. Schematic showing the alphanumeric system used to identify cells in the modules. For (a) MSX 60, the junction box was placed to the right during imaging characterizations. For (b) M55 modules, the positive junction box was maintained on the right during imaging characterizations.

Intermediate characterizations help track the extent of degradation during the course of the accelerated stress testing. One data point per temperature can be obtained with each module maintained at a different temperature. To increase the data points, after 326 kWh/m<sup>2</sup> of UV dosage, about 16 cells from each of the six field-aged modules were individually accessed. The individual cells of the field-aged modules were measured, and the UV exposure was continued until 450 kWh/m<sup>2</sup> was achieved. After the UV exposure all the characterizations (except QE) were repeated.

## Encapsulant Browning Degradation Rate Prediction

The data from the multiple cells in each of MSX 60 and M55 modules were used to calculate an  $E_a$  based on the Arrhenius plot Fig. 30. The  $E_a$  was used in calculating the acceleration factor (AF) which is a ratio of the degradation rates in accelerated tests to that in the field or between two fields.

$$AF = \frac{Rd. I_{sc} (ACC. TEST)}{Rd. I_{sc} (FIELD)} \quad \text{Eq. 7}$$

$$AF = \frac{Rd. I_{sc} (FIELD 1)}{Rd. I_{sc} (FIELD 2)} \quad \text{Eq. 8}$$

For predicting the degradation rates, the Arrhenius model is modified to include a UV term

$$\text{Modified Arrhenius model: } f(T, UV) = A \exp\left(-\frac{E_a}{kT}\right) UV^n \quad \text{Eq. 9}$$

where A is the pre-exponential factor,  $E_a$  is the activation energy, k is the Boltzmann's constant, T is the temperature in Kelvin, UV is the UV irradiance in  $W/m^2$ . n is the UV exponential factor and is taken as 0.6 [93]. The modified Arrhenius model accounts for the UV light stressor. The AF can be defined in two ways: 1) the ratio of the time to failure in the field test to the time to failure in another field or 2) the ratio of the stress rate in the accelerated test to the field test.

### Accelerated Test to Field (A2F) Approach

Using the  $E_a$  obtained, the degradation rate for the field can be predicted based on

$$AF = \left( \frac{UV_{ACC}}{UV_{FIELD}} \right)^m \exp \left( -\frac{E_a}{k} \left( \frac{1}{T_{ACC}} - \frac{1}{T_{FIELD}} \right) \right) \quad \text{Eq. 10}$$

where the  $m$  is taken as 0.6. The calculated  $AF$  was equated to the ratio of  $I_{sc}$  drop in the accelerated test to the  $I_{sc}$  drop in the field. A degradation rate can be predicted for each module that underwent testing based on module  $I_{sc}$  drop during the test, module temperature during the test, and weather data.

### Field to Field (F2F) Approach

The calculated  $E_a$  was used to predict the degradation rate for one field based on the conditions of another. The Arizona field conditions were considered to be the accelerated environment for encapsulant browning.

$$AF = \left( \frac{UV_{AZ}}{UV_{FIELD}} \right)^m \exp \left( -\frac{E_a}{k} \left( \frac{1}{T_{AZ}} - \frac{1}{T_{FIELD}} \right) \right) \quad \text{Eq. 11}$$

Using this approach, the degradation rate was predicted for New York and validated with measurements from modules exposed in New York.

### 3.4.2 Studying Solder Bond Degradation in Field-Aged Modules

Solder bond degradation affects the power output of a module. To study it, solder bond degradation needs to be replicated in controlled conditions. The two main solder bond degradation mechanisms are i) thermomechanical fatigue (TMF) caused due to different CTEs of the different materials and ii) intermetallic compound (IMC) formation driven by diffusion. As part of the Correlation of Qualification Testing with Field Degradation project, field-aged modules were stress tested in a modified thermal cycling test. A modified thermal cycling test aimed at inducing both degradation mechanisms was carried out. The overall goal of the project was to determine the acceleration factor for thermal cycling tests that would help predict the solder bond degradation rates.

#### Methodology

Two glass/backsheets construction, field-aged modules were used in the study. The Solarex MSX60 module with 36 polycrystalline silicon cells was field-aged for 21 years in Phoenix, Arizona. The Siemens M55 module with 36 monocrystalline silicon cells was field-aged for 18 years in Phoenix, Arizona. The MSX60 module has the standard  $\text{Sn}_{60}\text{Pb}_{40}$  solder-coated ribbon with a layer of additional  $\text{Sn}_{62}\text{Pb}_{36}\text{Ag}_2$  solder where the ribbon was hand-soldered to the Ag busbars (both front and back). This information was obtained through personal communication with a high-level ex-employee of Solarex. The M55 module has no Ag in its solder with its ribbons coated with the standard  $\text{Sn}_{60}\text{Pb}_{40}$  solder.

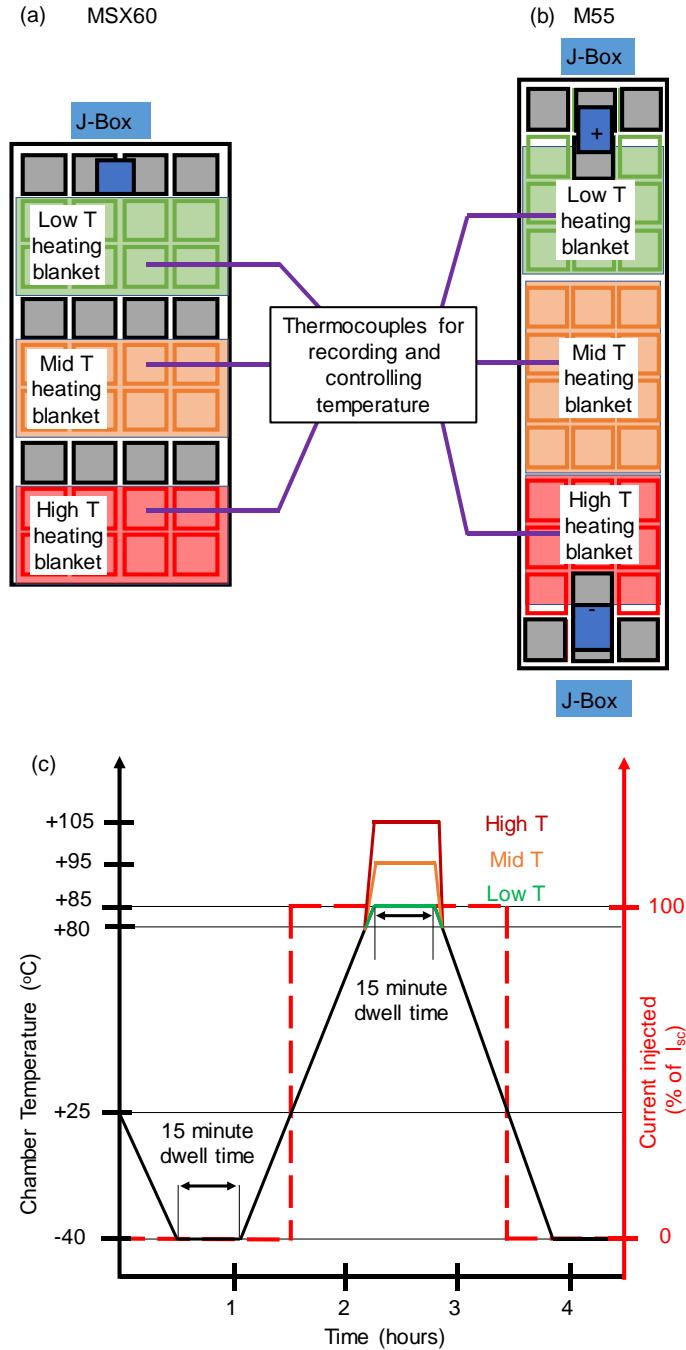


Fig. 34. Schematic representing the Low T, Mid T, and High T zones of the (a) MSX60 module and the (b) M55 module. The grey boxes represent cells not covered by the blankets and are excluded from data analysis. Six temperature controllers with six attached thermocouples were used to control the six individual heating blankets. (c) The temperature and current injection profiles of the modified thermal cycling test. Three zones in each module were maintained at different temperatures during the 15-minute dwell time using three thermally-separated but individually-controlled thermal blankets. Current equivalent

to the module  $I_{sc}$  was injected into the module when the chamber temperature was above 25°C.

The test modules were placed in a walk-in environmental chamber capable of controlling various ambient temperature and humidity levels. Each module was divided into three sections: low temperature (Low T), middle temperature (Mid T), and high temperature (High T) zones Fig. 34a and b. The backsheet of each zone was in contact with an electric heating blanket with feedback from the K-type thermocouples to help maintain multiple temperature sections with proportional-integral-derivative (PID) controllers. The thermal and current injection profiles of the modified TC test is shown Fig. 34c. The temperature settings of the electric blankets were adjusted to achieve 85°C, 95°C, and 105°C for the Low T, Mid T, and High T zones, respectively for both modules. Additionally, current equivalent to the short-circuit current ( $I_{sc}$ ) of the module was passed through the modules when the chamber temperature was above 25°C. The MSX60 module underwent TC800 whereas the M55 module underwent TC400 due to time constraints and this is considered in the interpretation of results.

Both modules were characterized extensively before, during, and after the modified-TC test with module-level light current-voltage (I-V), dark I-V, electroluminescence (EL) imaging, and outdoor infrared (IR) imaging. For EL imaging, the current equivalent to the module  $I_{sc}$  (at the start of modified TC) was injected and the image was captured over a 60 s exposure time. For outdoor IR imaging, the modules were placed on a two-axis tracker normal to the sun under short-circuit conditions for five minutes before taking images. All cells in both modules were accessed individually and their  $R_s$  values were determined with dark I-V. The method of individually accessing cells has been elaborated upon in a previous

paper [94]. With more data points per temperature zone, the statistical confidence in the test results increases. The cell-level measurements were used to calculate the  $E_a$  for solder bond degradation.

After the TC testing, busbar-solder samples from both modules and all three temperature sections were cut with a Dremel tool. To fully explain the reported observations, spots of interest on the busbars were chosen based on EL images. The samples were encased in epoxy, polished, and Au/Pd coated for SEM imaging and EDXS analysis. Images were obtained on a ZEISS AURIGA microscope, equipped with an Oxford Instruments X-Max<sup>N</sup> spectrometer. Images were taken at a working distance of 8 mm and operating voltage 15 kV. ImageJ was used to analyze the Scanning Electron Microscopy (SEM) images and Energy Dispersive X-ray Spectroscopy (EDXS) maps [95].

#### Solder Bond Degradation Rate Prediction

Using the cell level data, an  $E_a$  was calculated through the Arrhenius model. The  $E_a$  was used to calculate the AF from the Field environmental factors obtained from the TMY database [96].

### 3.5 Accelerated Stress Testing to Induce Encapsulant Browning and Solder Bond

#### Degradation in Freshly Fabricated 9-cut-cell Samples

With modules being used for testing, each module yields one data point. To increase the number of data points available, individual cells were accessed. To study the initial stages of encapsulant browning from UV exposure in samples with different module components, one-cell samples were used. Each one-cell mini-module yields one data point. To increase the data points available, one cell was cut into nine pieces and soldered as shown in Fig. 35. The laminate stack of the samples is as follows: i) a 203.2 mm x 203.2 mm Solite tempered glass superstrate, ii) UV-cut or UV-pass EVA, iii) mono-crystalline silicon cell (156 mm x 156 mm) with three busbars was cut into nine pieces (52 mm x 52 mm) and soldered for individual access, iv) UV-cut or UV-pass EVA, and v) a polymer backsheet (either TPT or KPE). The nine cell pieces had an average spacing of 11 mm – 12 mm between each other and the edge of the glass. The samples were laminated at 150°C in vacuum for 20 minutes.

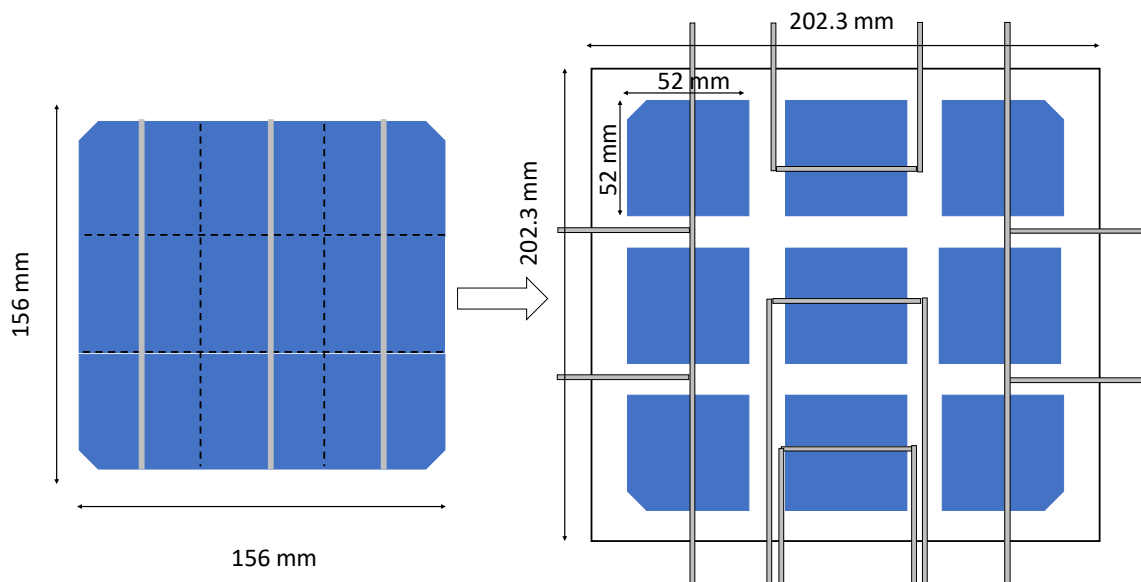




Fig. 35. Maximizing data points available from one cell by cutting the cell and then laminating it individually.

The 9-cut-cell samples were used in four studies with different components in the laminate stack. The EVA type (UV-cut or UC-pass), the cell interconnect type ( $\text{Sn}_{62}\text{Pb}_{36}\text{Ag}_2$ ,  $\text{Sn}_{60}\text{Pb}_{40}$ ,  $\text{Sn}_{42}\text{Bi}_{58}$ ), and the backsheets type (TPT or KPE) were different for each of the four projects presented. The samples were exposed to a combination of accelerated UV irradiance (UV), elevated temperatures (T), and relative humidity (RH). Studies were carried out with varying encapsulant, backsheets, solder type, and stressor combinations.

All samples were characterized before, during, and after exposure to stressors via i) UVF imaging, ii) LI-V and DI-V measurements, iii) reflectance, iv) colorimetry measurements, v) EL imaging, vi) IR imaging, and vii) visual imaging. For colorimetry and reflectance measurements, 18 spots per 9-cut-cell sample were measured as shown in Fig. 36.

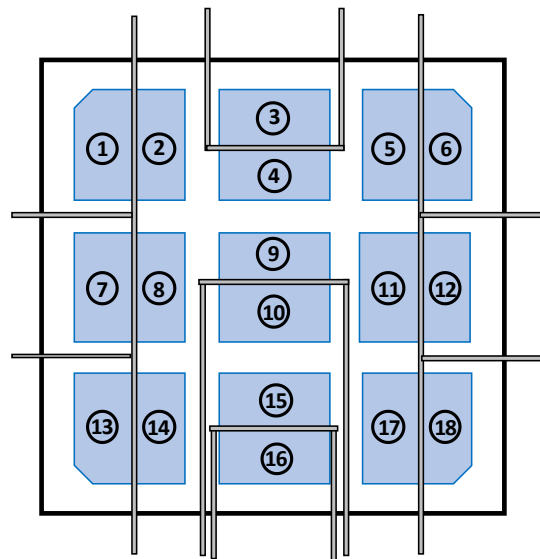


Fig. 36. Schematic showing the spots where colorimetry and reflectance measurements were obtained for all 9-cut-cell samples

3.5.1 Studying Encapsulant Browning in 9-cut-cell Samples UV-T exposure of 9-cut-cells with either UV-cut and UV-pass EVA above and below the cell [97]

Two sets of four 9-cut-cell samples with a glass/TPT backsheet construction were fabricated for this project. Two 9-cut-cell samples of each type were designated as control modules and remained unexposed to stressors. Six 9-cut-cell samples (three from each EVA type) were stress tested in an accelerated UV chamber at multiple temperatures through passive heating. Characterizations were carried out before, during, and after the UV exposure.

TABLE VIII: SUMMARY OF SAMPLE PARAMETERS AND STRESSORS OF ACCELERATED UV EXPOSURE AT ELEVATED TEMPERATURES

Parameter		Details	
		Set 1	Set 2
Sample	Encapsulant above cell	UV Cut	UV Pass
	Metallization	Sn <sub>60</sub> Pb <sub>40</sub>	Sn <sub>60</sub> Pb <sub>40</sub>
	Encapsulant below cell	UV Cut	UV Pass
	Backsheet type	TPT	TPT
Stressor	Accelerated UV	800 kWh/m <sup>2</sup>	
	Elevated Temperature	Yes	Yes
	Relative Humidity	No	No

9-cut-cell samples with UVC EVA (UVC1, UVC2, and UVC3) or UVP EVA (UVP1, UVP2, and UVP3) were exposed to accelerated UV light with a T-type thermocouple attached to the backsheet (below the middle cell) to monitor the temperature. The backsheet and the 9-cut-cell sample edges were covered with aluminium (Al) tape to prevent oxygen diffusion through the backsheet. To obtain multiple temperatures, foamboards of different thicknesses were placed on the Al tape attached to the backsheet (Fig. 37). The UVC1 and UVP1 samples had Al tape but no insulation on the backsheet. The UVC2 and UVP2

samples had Al tape and 0.5” thick insulating foamboard on the backsheet. The UVC3 and UVP3 samples had Al tape and 2” thick insulating foamboard on the backsheet.

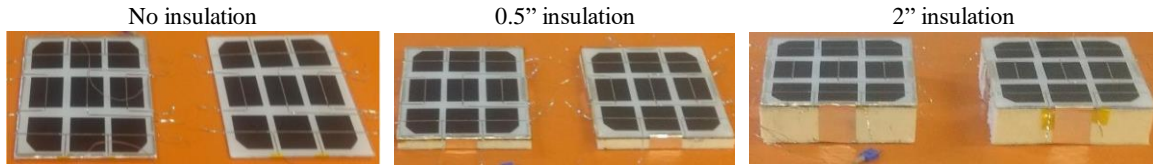


Fig. 37. Images of samples with no insulation on the UVC1 and UVP1 9-cut-cell samples, half-inch thick foamboard insulation on the UVC2 and UVP2 9-cut-cell samples and two-inch thick foamboard insulation on the UVC3 and UVP3 9-cut-cell samples.

The advantages to the above approach include i) in one walk-in UV chamber, multiple temperatures were obtained via passive heating while other samples underwent regular UV exposure, ii) all the data required was obtained in one experiment, and iii) multiple cells per sample increases the statistical significance in the results and the confidence in analysis

The samples were exposed to a total of 800 kWh/m<sup>2</sup> of UV dosage with the following characterizations every 200 kWh/m<sup>2</sup> i) UVF imaging, ii) LI-V and DI-V measurements, iii) reflectance, and iv) colorimetry measurements. The I<sub>sc</sub> measurements for all six samples were taken after 600 kWh/m<sup>2</sup> and not after 800 kWh/m<sup>2</sup> due to unavailability of the solar simulator.

3.5.2 Combined UV-T-RH Accelerated Testing of PV Modules: Reliability of UV-Cut and UV-Pass EVA Encapsulants [98]

Two sets of four 9-cut-cell samples with a glass/TPT backsheet construction were fabricated for this project. Six 9-cut-cell samples from both sets were stress tested in an accelerated UV chamber at multiple temperatures while being exposed to relative humidity. Two samples of each type were designated as control modules. Characterizations were carried out before, during, and after the UV exposure.

TABLE IX: SUMMARY OF SAMPLE PARAMETERS AND STRESSORS OF ACCELERATED UV EXPOSURE AT ELEVATED TEMPERATURES WITH HUMIDITY

Parameter		Details	
		Set 1	Set 2
Sample	Encapsulant above cell	UV Cut	UV Pass
	Metallization	Sn <sub>60</sub> Pb <sub>40</sub>	Sn <sub>60</sub> Pb <sub>40</sub>
	Encapsulant below cell	UV Cut	UV Cut
	Backsheet type	TPT	TPT
Stressor	Accelerated UV	200 kWh/m <sup>2</sup>	
	Elevated Temperature	Yes	Yes
	Relative Humidity	Yes	Yes

Each of the six samples in the accelerated stress test had a T-type thermocouple attached to the backsheet (below the middle cell) to monitor the temperature. To maintain the samples at different temperatures, electric heating blankets were used along with a steam generator to maintain the humidity level based on the feedback from a humidity sensor as shown in Fig. 38.

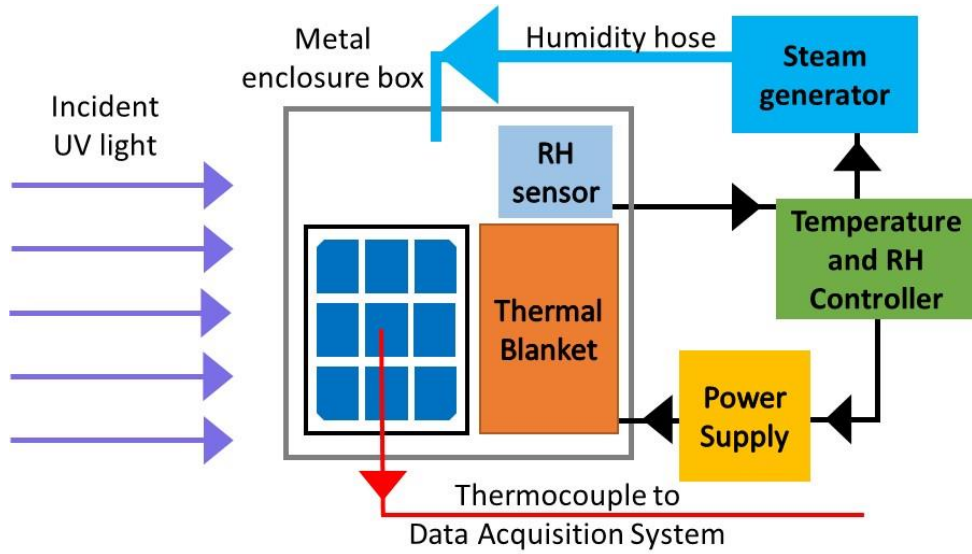


Fig. 38. Concept of the set-up with UV and RH exposure at elevated temperatures.

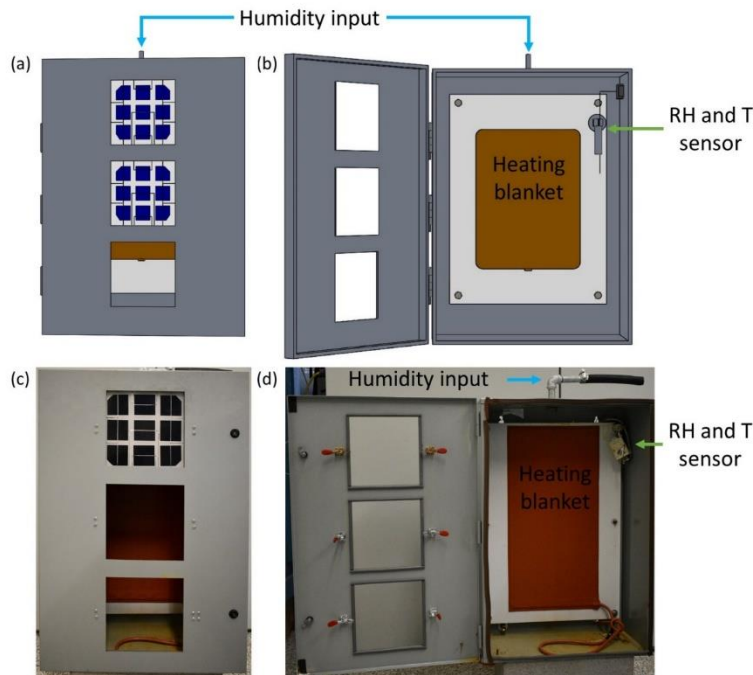


Fig. 39. (a) and (b) Model of the UV-T-RH setup along with (c) and (d) images of the setup.

The sealed metal enclosure box in Fig. 39 prevents humidity from escaping into the UV chamber and corroding the UV lamp terminals. There are several advantages to this

unique approach: i) In one walk-in UV chamber, multiple temperatures were obtained via active heating while other samples underwent UV exposure, ii) All the data required was obtained in one experiment, iii) Multiple cells per sample increases the statistical significance in the results and the confidence in analysis, iv) 9-cut-cell samples are exposed simultaneously to elevated temperatures, concentrated UV light, and humidity during the test

The samples were exposed to 200 kWh/m<sup>2</sup> of UV dosage with the following characterizations carried out before and after the exposure i) UVF imaging, ii) LI-V and DI-V measurements, iii) colorimetry measurements, and iv) reflectance measurements.

### 3.5.3 Combined UV-T-RH Accelerated Testing of 9-cut-cell Samples

Two sets of ten 9-cut-cell samples were fabricated each set with a different backsheets. All samples had metallization with three different solder bond compositions and UV Pass EVA above the solar cells and UV Cut EVA below the solar cells. One sample from each set was designated as the control module.

TABLE X: SUMMARY OF SAMPLE PARAMETERS AND STRESSORS OF ACCELERATED UV EXPOSURE AT ELEVATED TEMPERATURES WITH HUMIDITY

Parameter		Details	
		Set 1	Set 2
Sample	Encapsulant above cell	UV Pass	UV Pass
	Metallization	Pb <sub>40</sub> Sn <sub>60</sub> , Pb <sub>36</sub> Sn <sub>62</sub> Ag <sub>2</sub> , Sn <sub>42</sub> Bi <sub>58</sub>	
	Encapsulant below cell	UV Cut	UV Cut
	Backsheet type	TPT	KPE
Stressor	Accelerated UV	225 kWh/m <sup>2</sup>	
	Elevated Temperature	Yes	Yes
	Relative Humidity	Yes	Yes

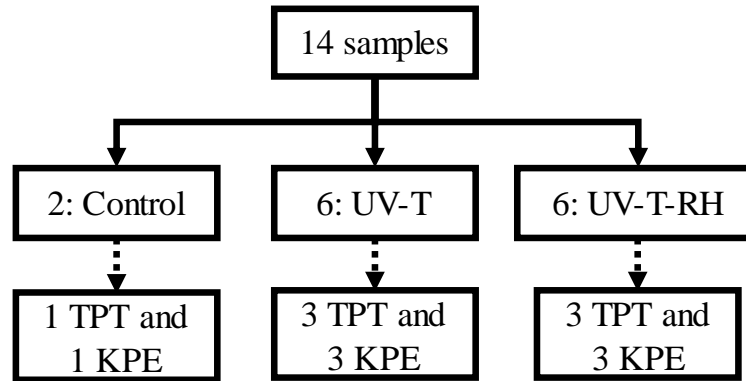


Fig. 40. Distribution of samples for accelerated UV exposure at elevated temperatures with and without humidity.

Samples within each set of six were maintained at three temperatures to aid in calculation of activation energies for encapsulant browning and solder bond degradation. The six samples that underwent UV-T exposure consisted of three samples with TPT backsheets and three samples with KPE backsheets. Heating blankets were used to maintain

three temperatures. Each temperature blanket is for one set of samples with TPT and KPE backsheets. A similar sample set UV-T-RH exposure. All samples underwent the following characterizations before and after accelerated testing i) EL imaging, ii) Indoor IR imaging, iii) LI-V and DI-V, iv) colorimetry, v) reflectance measurements, vi) UVF imaging, and vii) visual imaging.



### 3.5.4 Studying Solder Bond Degradation in 9-cut-cell Samples

One set of six samples described in the previous section underwent the modified thermal cycling profile in Fig. 34c. Heating blankets were used to maintain sample temperatures at 85°C, 95°C, and 105°C for the Low T, Mid T, and High T conditions.

TABLE XI: SAMPLE PARAMETERS AND STRESSORS THERMAL CYCLING

Parameter		Details	
		Set 1	Set 2
Sample	Encapsulant above cell	UV Pass	UV Pass
	Metallization	Pb <sub>36</sub> Sn <sub>62</sub> Ag <sub>2</sub> , Pb <sub>40</sub> Sn <sub>60</sub> , and Sn <sub>42</sub> Bi <sub>58</sub>	
	Encapsulant below cell	UV Cut	UV Cut
	Backsheet type	TPT	KPE
Stressor	Cycling Temperature	500 modified thermal cycles from -40°C to 85°C, 95°C, 105°C for 15 minutes for Low T, Mid T, and High T	
	Static Temperature		

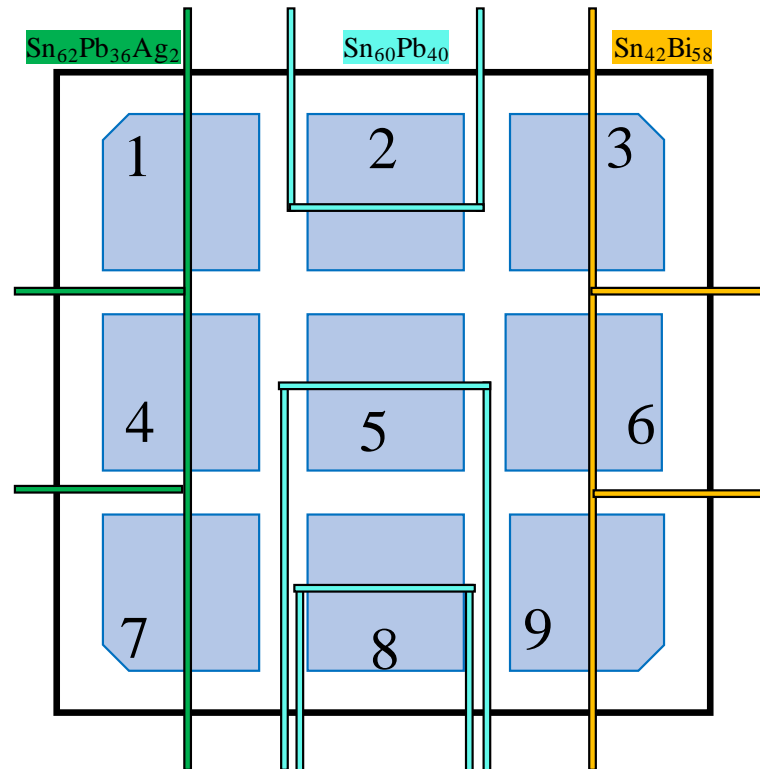


Fig. 41. Schematic showing the three solder types in each 9-cut-cell sample used for accelerated testing.

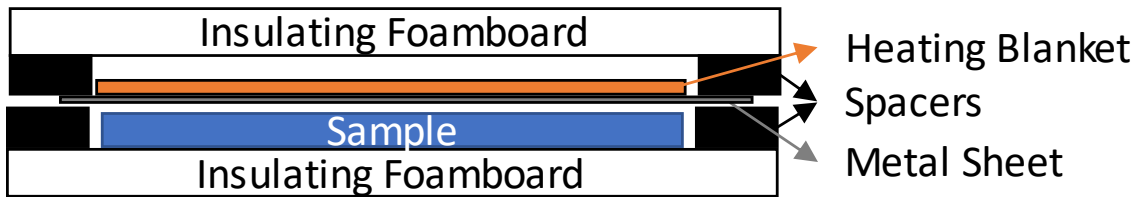


Fig. 42. Representation of arrangement of samples during the thermal cycling test

The parameters in TABLE XI and Fig. 41 highlight the design aspect of having multiple solder compositions within one sample. During testing, the samples were arranged as shown in Fig. 42. Foamboard was used as a base so the samples would not come in contact with the chamber floor. A silicone heating blanket was placed on a thin metal sheet resting on spacers. Radiative heating was used to maintain the samples at elevated temperatures during the hot dwell time of the thermal cycles. The foamboard above the heater prevents heat loss to the ambient in the Thermotron chamber. No current was injected in the samples during testing. All samples underwent the following characterizations before and after accelerated testing i) EL imaging, ii) Indoor IR imaging, iii) LI-V and DI-V, iv) colorimetry, v) reflectance measurements, vi) UVF imaging, and vii) visual imaging.

## CHAPTER 4: RESULTS AND DISCUSSION

### 4.1 Accelerated Stress Testing to Induce Encapsulant Browning and Solder Bond

#### Degradation in Field-Aged Modules

##### 4.1.1 Studying Encapsulant Browning in Field-Aged Modules

The field and the accelerated test databases can be found on the [ASU-PRL website](#). The approach of using passive heating to obtain multiple temperatures in accelerated UV testing was demonstrated (Table V). The combination of solar gain from the UV lamps and the thermal insulation on the backsheet allowed the field-aged modules to be maintained at different temperatures. As the insulation thickness on the module backsheet increased, more heat was retained, and a higher module temperature was obtained in the Mid T and the High T modules. The small temperature differences between Low T, Mid T, and High T modules in the M55 set can be attributed to their form factor. This unique passive heating approach saves both resources and time while data at multiple temperatures were obtained simultaneously with a single UV chamber run.

TABLE XII: TEMPERATURES OF MSX 60 AND M55 MODULES DURING THE 450 kWh/m<sup>2</sup> UV ACCELERATED TEST

	<b>Module</b>	<b>Avg. Temperature (°C)</b>	<b>Std. Dev. (°C)</b>
<b>MSX 60</b>	Fresh: No insulation	67.2	3.8
	Low T: No insulation	60.5	6.4
	Mid T: 0.5" insulation	76.8	5.5
	High T: 2" insulation	84.9	5.9
<b>M55</b>	Fresh: No insulation	63.8	4.4
	Low T: No insulation	75.4	3.9
	Mid T: 0.5" insulation	80.4	4.6
	High T: 2" insulation	82.7	5.0

## Module-level Characterization Results

The pre-and post-stress test characterizations of the eight modules is presented below. The module-level characterizations presented and analyzed include UVF imaging, module-level LI-V and DI-V, EL imaging, indoor and outdoor IR imaging. Cell-level data presented include QE, reflectance, and cell-level I-V.

### Ultra-violet Fluorescence (UVF) Imaging

UVF imaging was used to identify the extent and intensity of browning of the modules. Browning area has been increased with UV exposure and the degree of degradation was correlated to the module temperature. Modules at a higher temperature exhibited greater browning in both MSX and M55 field-aged modules as seen in Fig. 43. The fresh modules of both types showed signs of uniform browning on all cells. The peripheral cells appeared to be less brown than the center cells of the module. This might be attributed to a small temperature variation within the module due to its placement within the UV chamber.

Another interesting feature of MSX modules is the streak pattern in the cracked cells caused by photobleaching of the browned EVA. The cell cracks open the pathways for oxygen to diffuse through the backsheet and the areas between the cells. Furthermore, the pattern has not changed post-testing due to the presence of Al tape that acts as a barrier against oxygen and moisture ingress through the backsheet. The cells in the MSX 60 module are thinner (200  $\mu\text{m}$ ) than those in the M55 module (300  $\mu\text{m}$ ) leading to more cracks during their field-exposure. The difference in image intensity between the pre- and post- accelerated UV exposure images is due to more lamps being added to the UVF

imaging setup once the UV exposure had begun. The encapsulant browning reaction was intensified due to the presence of Al tape on the backsheet of the field-aged modules.


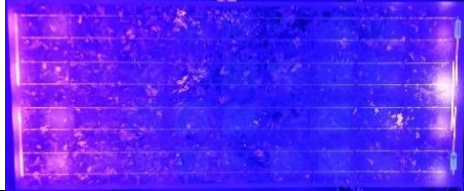
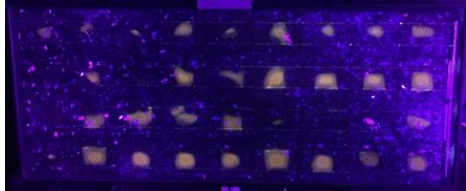
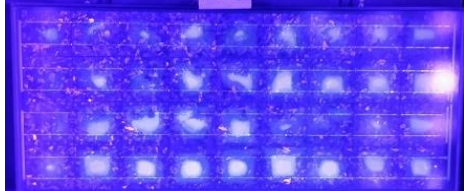
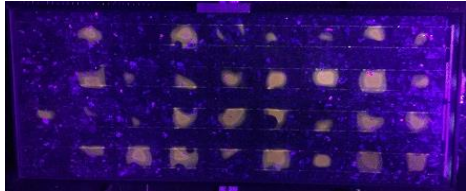
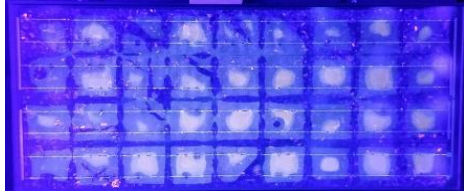
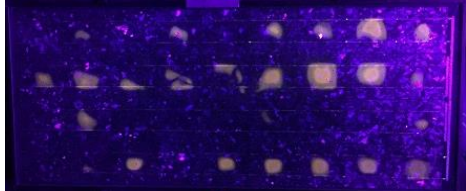
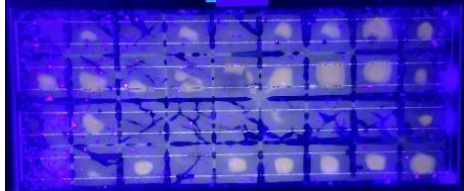
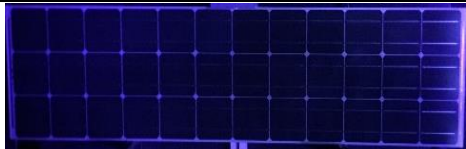

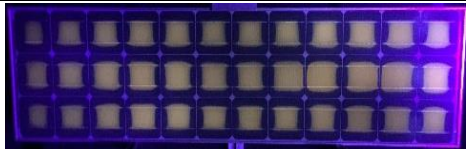
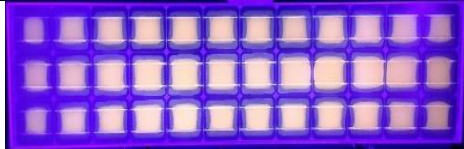
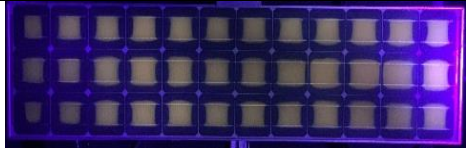
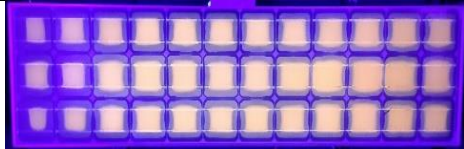
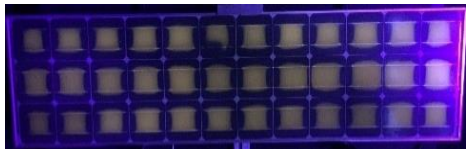
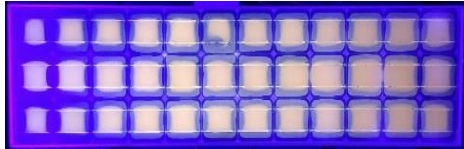
Module	Pre 450 kWh/m <sup>2</sup> exposure	Post 450 kWh/m <sup>2</sup> exposure
<b>MSX Fresh</b>		
<b>MSX 4961 Low T</b>		
<b>MSX 4968 Mid T</b>		
<b>MSX 4960 High T</b>		
<b>M55 Fresh</b>		
<b>M55 4186 Low T</b>		
<b>M55 4149 Mid T</b>		
<b>M55 4137 High T</b>		

Fig. 43. UVF images of modules before and after UV exposure

## LI-V and DI-V curve tracing

The module-level LIV and DIV reflect on the module's performance. Over time, the  $I_{sc}$  of the modules is expected to drop with an increase in temperature. The extent of  $I_{sc}$  degradation in MSX modules correlated to their operating temperature in UV exposure test. Higher temperature accelerates the browning rate, resulting in greater  $I_{sc}$  drop.

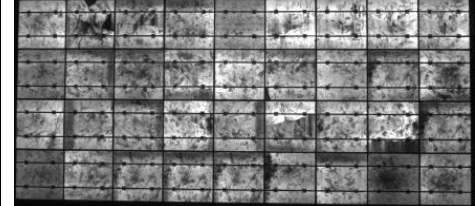
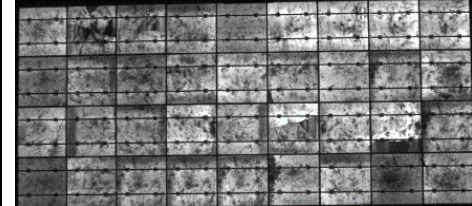
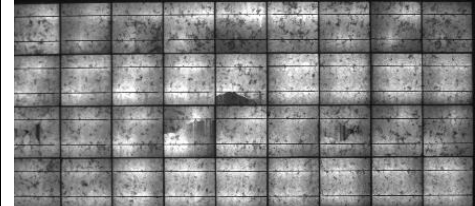
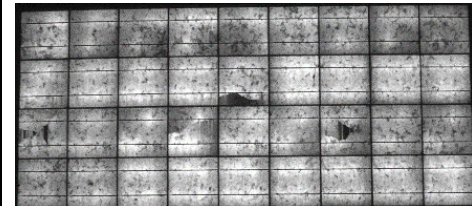
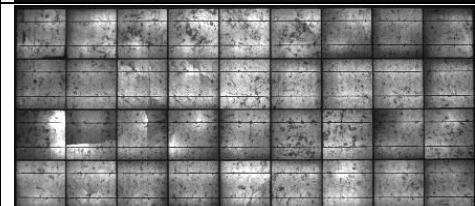
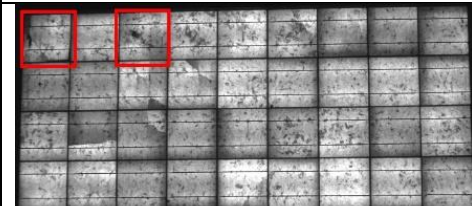
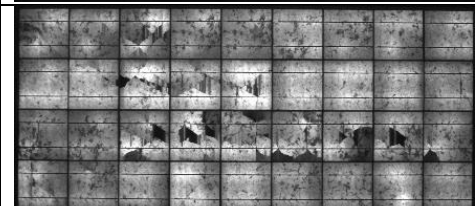
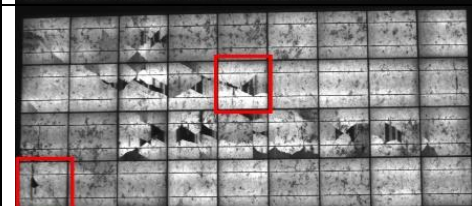
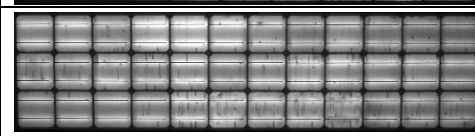
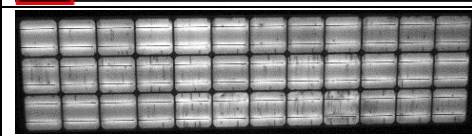
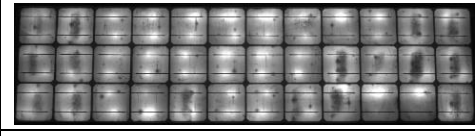
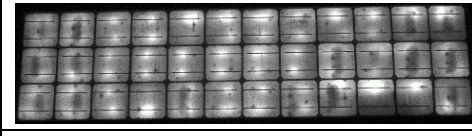
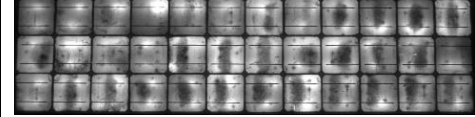
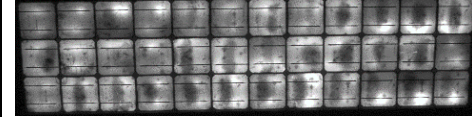
TABLE XIII: MODULE-LEVEL LIV AND DIV PERFORMANCE AFTER 450 kWh/m<sup>2</sup> OF UV DOSAGE

Modules			$I_{sc}$ (A)	$I_{sc}$ deg (%)	$V_{oc}$ (V)	$I_{mp}$ (A)	$V_{mp}$ (V)	FF (%)	$P_{max}$ (W)	$R_s$ ( $\Omega$ )	$R_{sh}$ ( $\Omega$ )
MSX	Fresh 67°C	Pre	4.72		21.70	4.25	17.29	71.6	73.43	0.69	842
		Post	4.68	0.85	21.60	4.25	17.00	71.5	72.40	0.62	1012
	Low T 60°C	Pre	3.64		21.50	3.38	16.82	72.7	56.90	0.72	3099
		Post	3.60	1.09	21.30	3.33	16.90	73.3	56.30	0.68	3094
	Mid T 77°C	Pre	3.62		21.35	3.35	16.75	72.5	56.14	0.88	4452
		Post	3.56	1.66	21.20	3.26	17.00	73.2	55.40	0.46	12710
	High T 85°C	Pre	3.62		21.44	3.27	16.82	70.7	54.92	0.92	5036
		Post	3.52	2.76	21.30	3.17	17.10	72.0	54.10	0.69	17465
MS5	Fresh 64°C	Pre	10.04		7.26	9.12	5.62	70.3	51.24	2.44	6667
		Post	9.71	3.29	7.20	8.80	5.70	71.4	49.70	2.64	7743
	Low T 75°C	Pre	3.14		21.67	2.84	16.54	69.1	46.99	1.18	8024
		Post	3.06	2.54	21.60	2.73	16.20	67.0	44.30	1.29	6229
	Mid T 80°C	Pre	3.14		21.58	2.76	15.83	64.6	43.73	1.27	6678
		Post	2.99	4.77	21.40	2.63	15.90	65.1	41.80	1.50	8062
	High T 83°C	Pre	3.18		21.68	2.83	16.34	67.0	46.20	1.23	13355
		Post	3.04	4.40	21.50	2.69	16.20	66.9	43.60	1.54	6261

## Electroluminescence (EL) imaging

Fig. 44 shows the EL images of modules taken pre and post UV stress testing. No major changes were seen in MSX fresh and insulated modules. Few cells in MSX 4968 (A1 and A3) and MSX 4960 (B5 and D1) have darkened regions post-testing, which is likely due

to the prolonged exposure of modules to high intensity UV light at elevated temperatures that exerted some stress to the cells in the vicinity of cracks. This led to more opening of the cracks and aggravated their severity from mode-B to mode-C [99].

Module	Pre 450 kWh/m <sup>2</sup> exposure	Post 450 kWh/m <sup>2</sup> exposure
MSX Fresh		
MSX 4961		
MSX 4968		
MSX 4960		
M55 Fresh		
M55 4186		
M55 4149		

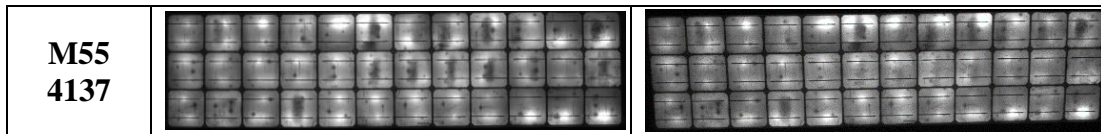
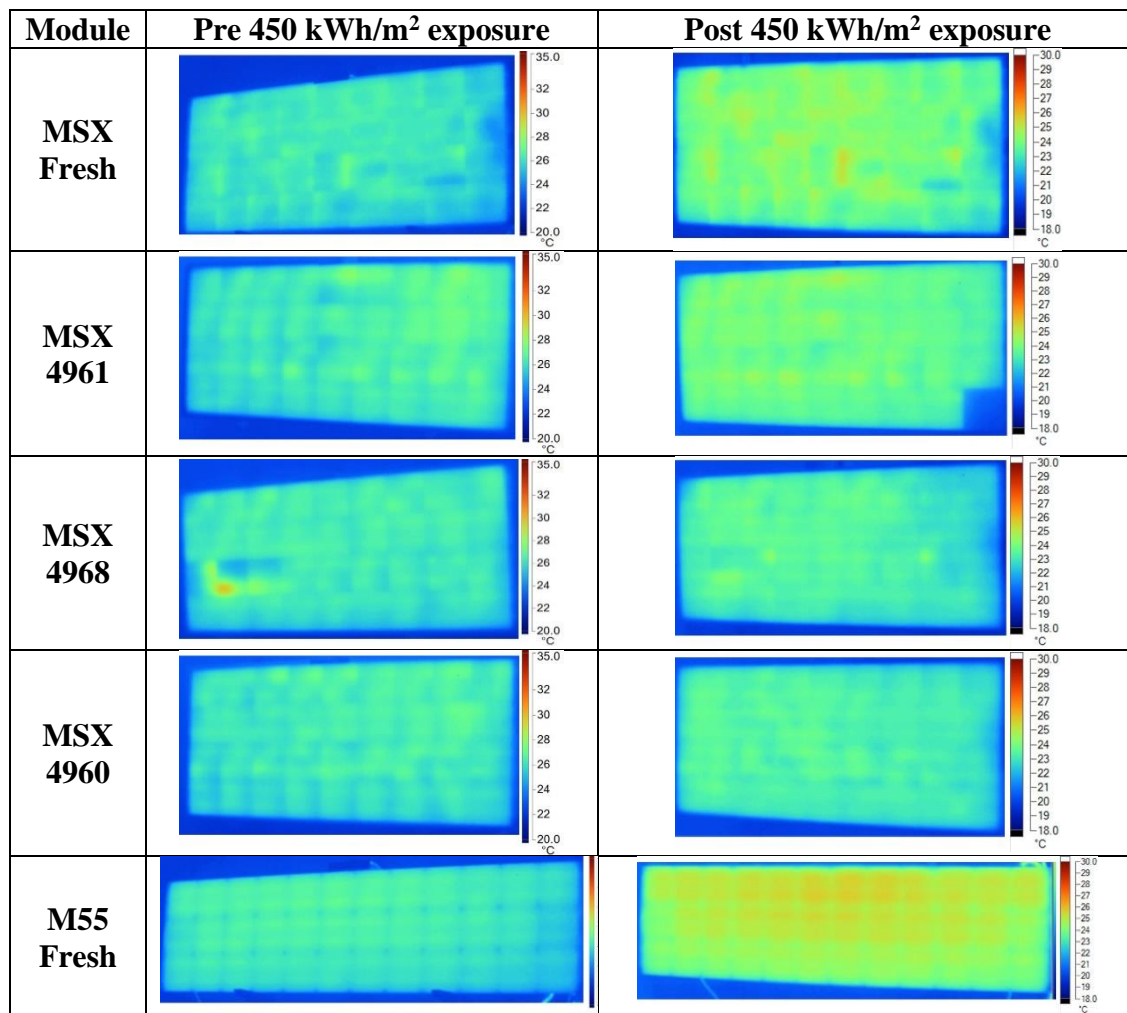


Fig. 44. EL images of the modules before and after the UV exposure. Current equivalent to the module  $I_{sc}$  was injected and the image was taken over 60 s.

### Indoor infra-red (IR) imaging

MSX modules did not display much change in the thermal images in Fig. 45. However, the M55 modules exhibited some hot cells. Note that the temperature scale for the pre-stress test images is 20°C - 35°C, whereas for the post-stress test images it is 18°C - 30°C.





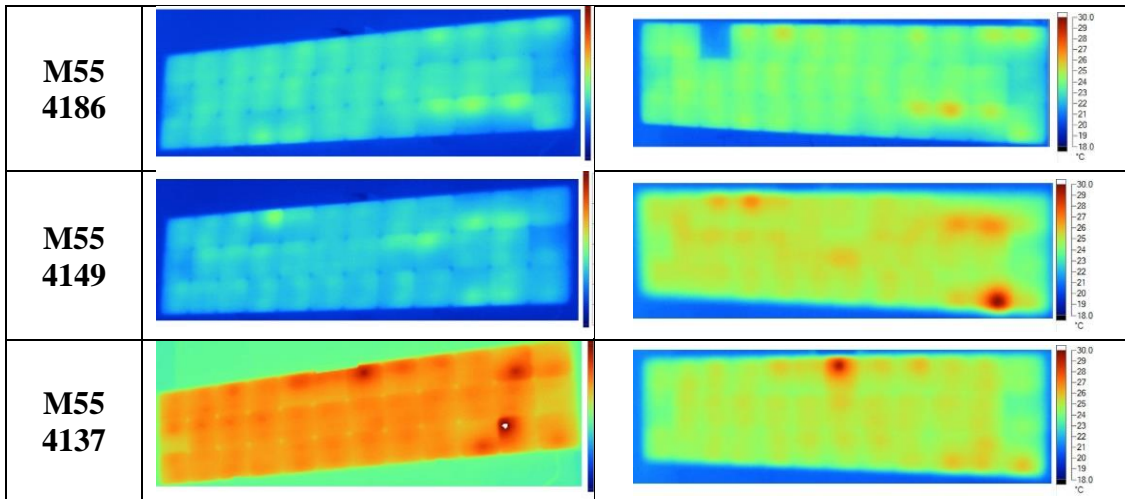
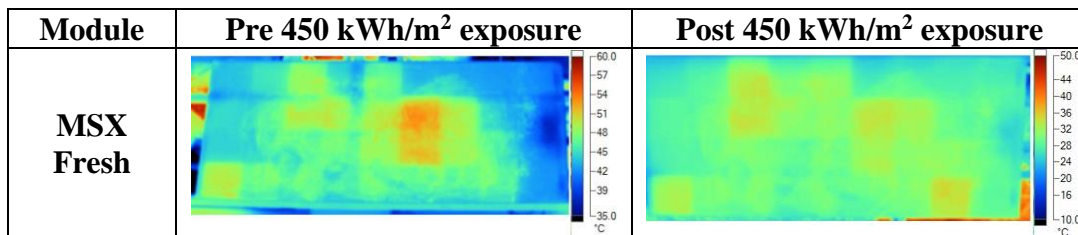


Fig. 45. Indoor IR images of the modules before and after the UV exposure. The module was connected in forward bias and current equivalent to the  $I_{sc}$  was injected for 5 minutes.

#### Outdoor infra-red (IR) imaging

Fig. 46 shows the IR images of the module under short-circuit conditions taken on a clear sunny day, pre and post-stress testing. For all modules, no significant change was observed, indicating that the UV exposure affected mainly the EVA layer and not the status of the cells. However, some cells are operating at considerably higher temperatures than the others around them. These cells have slightly patterned encapsulant browning as seen in the UVF images, and no cracks as shown in the corresponding EL images. Note that the temperature scale for the pre-stress test images is 35°C - 60°C, whereas for the post-stress test images it is 10°C - 50°C.



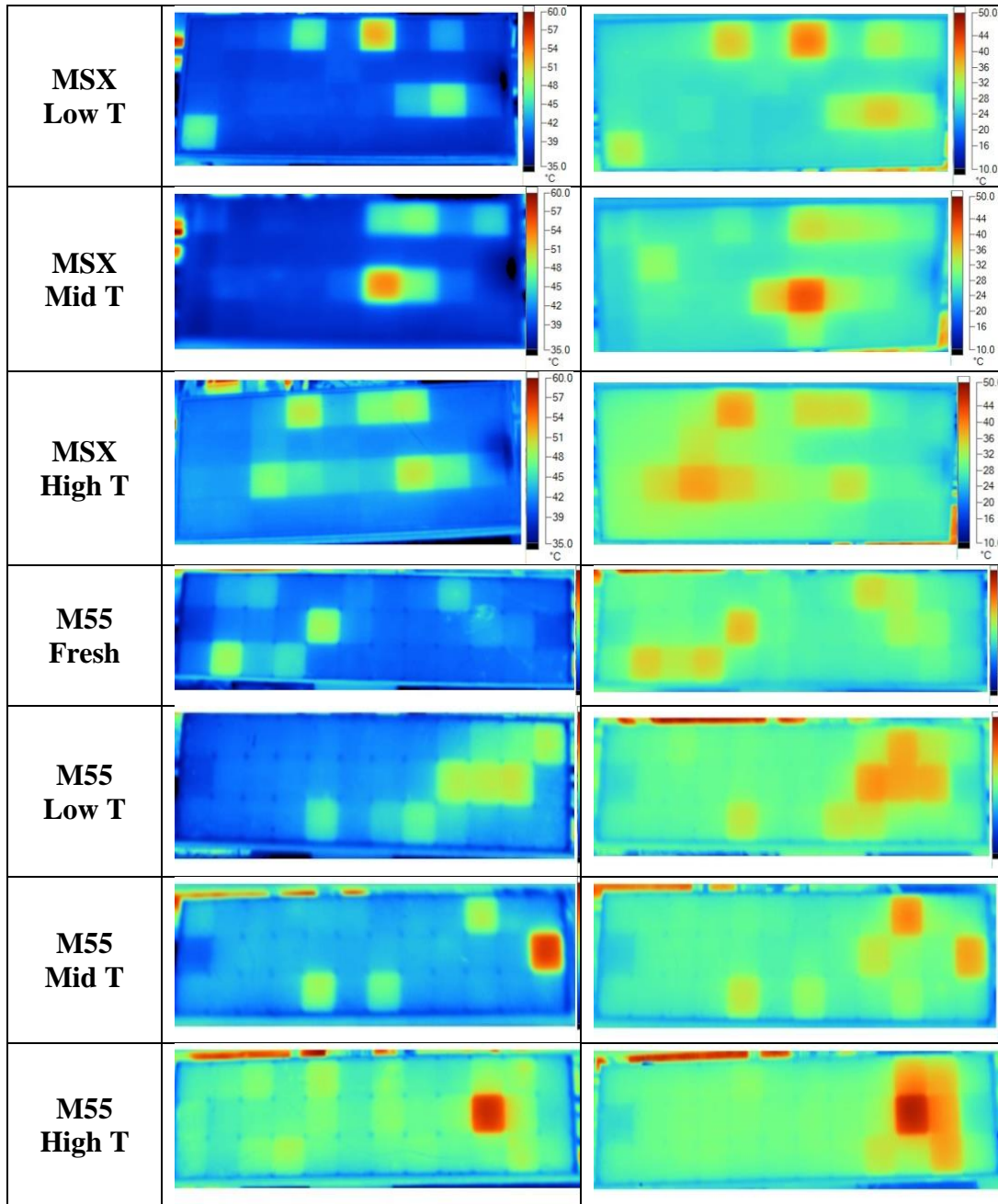


Fig. 46. Outdoor IR images of the modules before and after the UV exposure. The module was placed in the sun under short-circuit conditions for 5 minutes.

Cell-level Characterization Results

Cell-level characterizations give localized information and can provide multiple data points within one module. Quantum efficiency, reflectance, LIV, and DIV are cell-level measurements that provide more clarity. The locations of these characterizations have been highlighted in Fig. 47. The backsheets of about 15 cells from each of the field-aged modules were cut and their  $I_{sc}$  were measured.

76

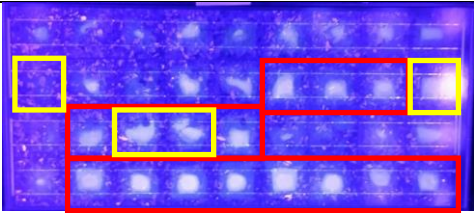
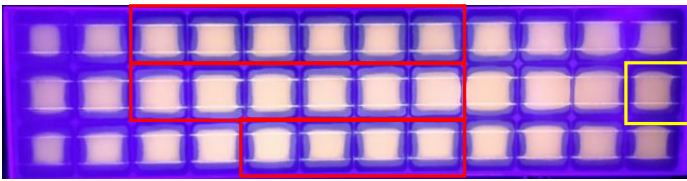
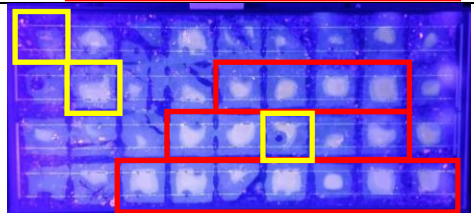
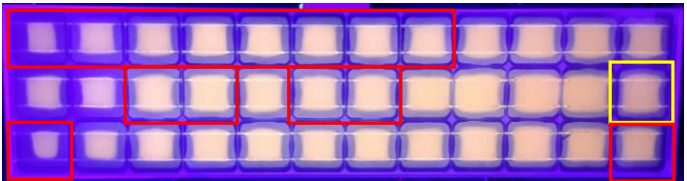
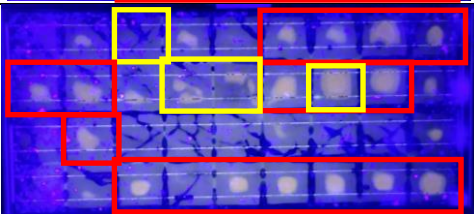
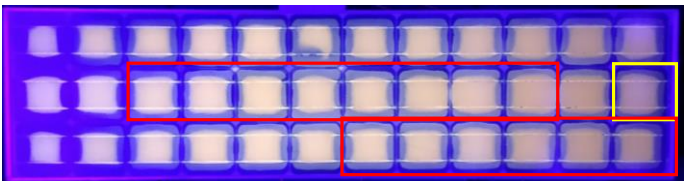
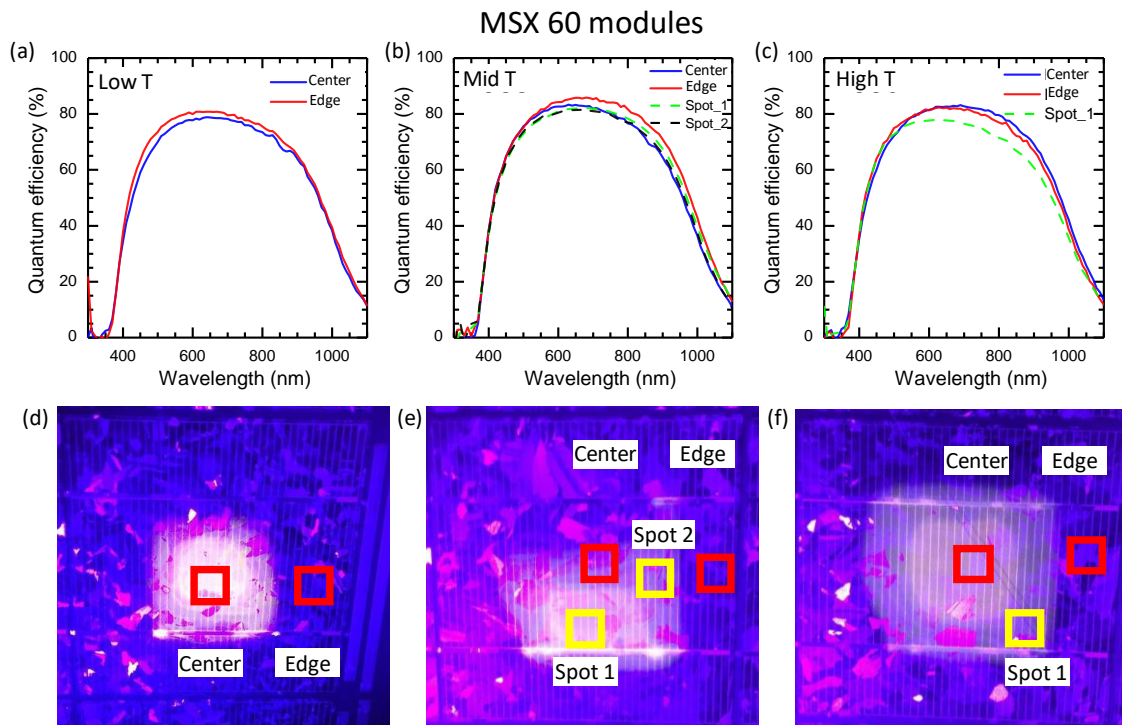
Module	MSX 60	M55
Low T		
Mid T		
High T		

Fig. 47. UVF images with cells marked that correspond to measurements taken. Solar simulator measurements were taken on the cells highlighted in red. Reflectance, and quantum efficiency measurements were taken on cells highlighted in yellow. Fresh modules did not have their cells individually accessed.

## Quantum Efficiency (QE) measurements

The efficiency of the local cell area for representative cells from each of the three MSX 60 and M55 modules is shown here. The plots presented are from before accelerated UV exposure. Measurements post UV exposure were not able to be taken due to unavailability of the machine. The QE in Fig. 48 of different areas of the cell show the effect of field-exposure-induced encapsulant browning. MSX 60 modules experience a uniform drop in QE across the wavelengths whereas M55 modules have lower QE in the lower wavelength range. This could be indicative of different chromophore formation between the module types.



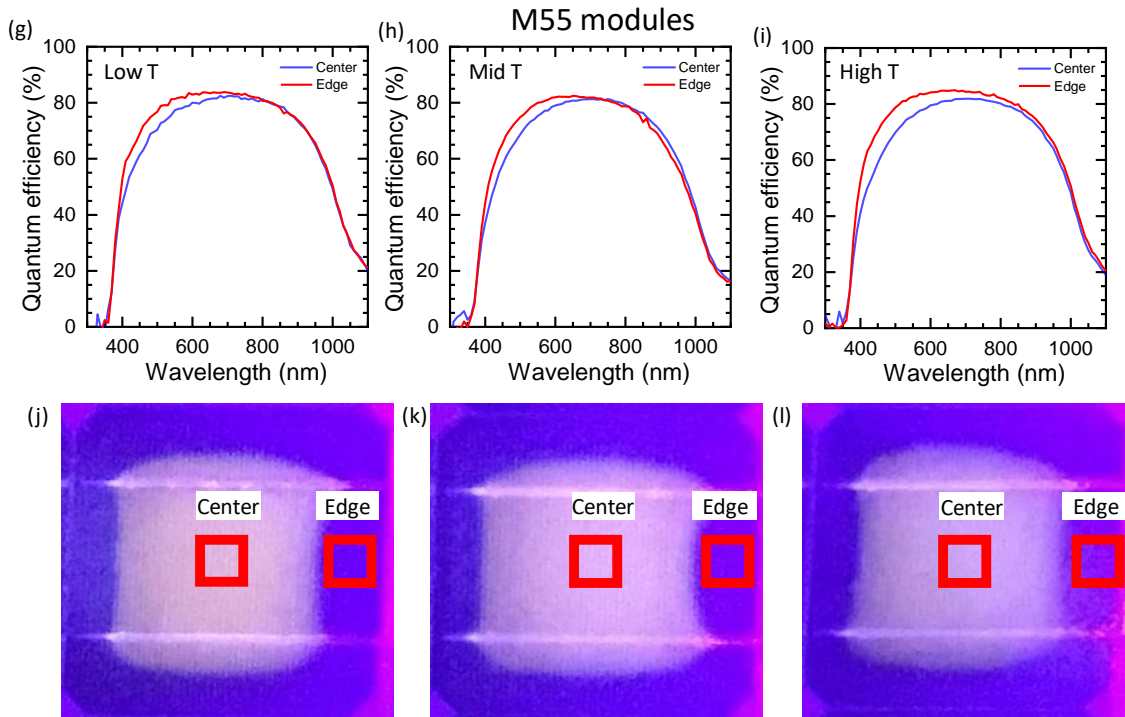


Fig. 48. QE measurements of representative cells from the Low T, Mid T, and High T modules of MSX 60 and M55 modules. The cell centers consistently show lower QE than the cell edges between 400 nm and 900 nm.

#### Reflectance measurements

The reflectance is expected to decrease with an increase in the browning of the encapsulant due to the increased absorbance of the browned EVA. Below are representative plots of reflectance from one cell in the each of the modules as shown in Fig. 49. The spots measured in the modules show a decreased reflectance when compared to the pre-UV exposure values.

### MSX 60 modules

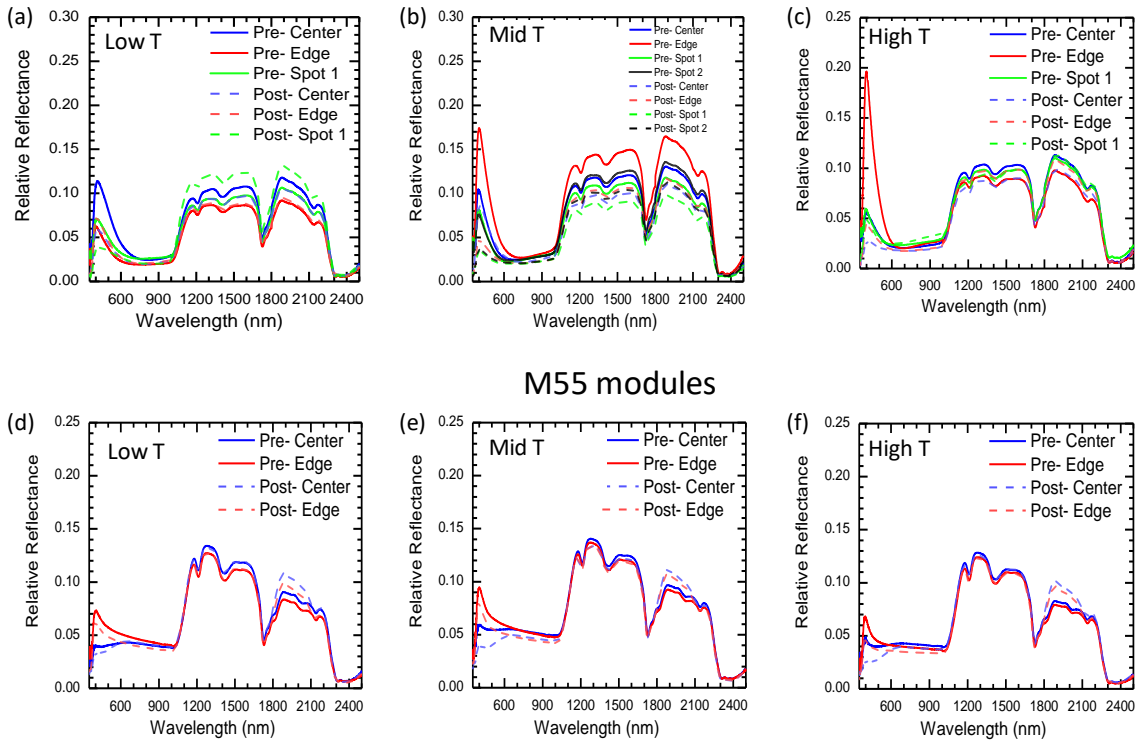


Fig. 49. Reflectance curves from one representative cell in each of the six field-aged modules, the same for which QE measurements are shown in Fig. 48.

### Cell-level LI-V and DI-V curve tracing

The LIV characteristics of individual cells in the module are measured by a solar simulator, which is calibrated with a standard reference cell. Fig. 50 shows the cell  $I_{sc}$  drop after 450 kWh/m<sup>2</sup> of UV exposure in the chamber. About 16 cells from each of the six modules were individually accessed after 326 kWh/m<sup>2</sup> of UV exposure.

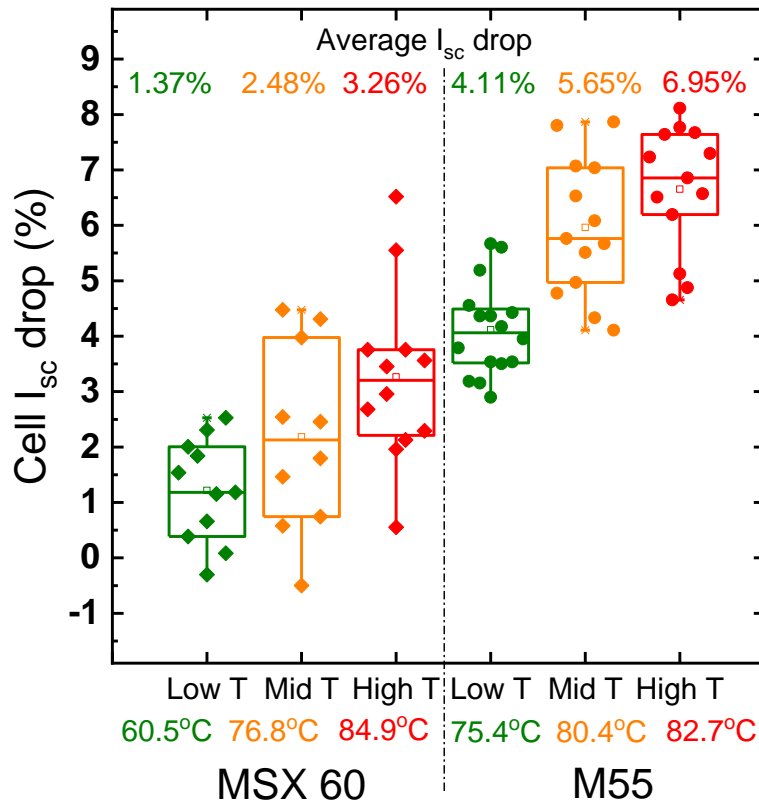


Fig. 50. Box plot of the cell-level  $I_{sc}$  measurements of the individual cells in the MSX 60 and M55 modules. Module-level  $I_{sc}$  (at 0 kWh/m<sup>2</sup>) was taken as the initial measurement whereas cell-level  $I_{sc}$  (at 450 kWh/m<sup>2</sup>) was taken as the final measurement.

It is possible that MSX 60 and M55 modules had different EVA formulations (standard vs. fast cure) as supported by UVF images (Fig. 43) and Fig. 50. The UVF images for MSX 60 modules show two intensities of browning in the pre-accelerated UV exposure images whereas the M55 modules show uniform intensity of fluorescence. This could be indicative of at least two types of chromophores in the MSX 60 modules. The lamination time, temperature, and EVA formulation all affect the concentration of chromophores in the EVA. This could explain the higher drop in  $I_{sc}$  in the Low T M55 module than in the High T MSX 60 module.

## Activation Energy Calculation and Encapsulant Browning Degradation Rate Prediction

For encapsulant browning,  $I_{sc}$  is the parameter used for  $E_a$  and AF calculations and not  $P_{max}$ . The average drop in  $I_{sc}$  for the cells in the MSX 60 and M55 modules was graphed on an Arrhenius plot to calculate the  $E_a$  for encapsulant browning in Fig. 51.

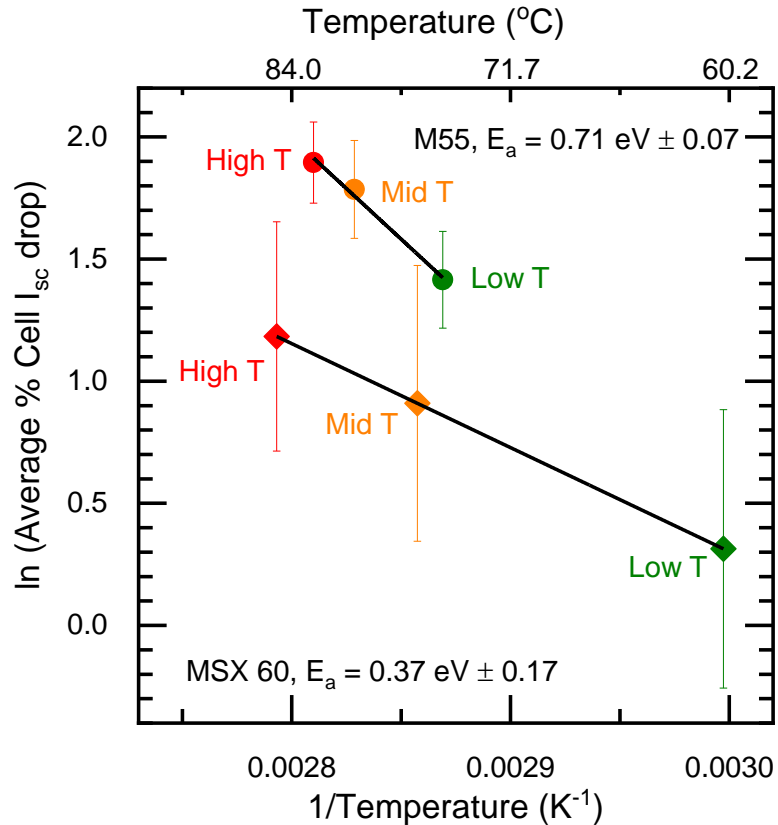


Fig. 51. Activation energy calculation from the average %  $I_{sc}$  drop from the MSX 60 and M55 module. The  $E_a$  for MSX 60 modules is 0.37 eV. The Low T, Mid T, and High T data points represent the average % $I_{sc}$  drop of 10 cells, 9 cells, and 12 cells, respectively. The  $E_a$  for M55 modules is 0.71 eV. The Low T, Mid T, and High T data points represent the average % $I_{sc}$  drop of 16 cells, 13 cells, and 13 cells, respectively.

The Arrhenius plots in Fig. 51 shows the  $E_a$  calculated from the average %  $I_{sc}$  degradation of cells to be 0.37 eV for MSX60 and 0.71 eV for M55 modules. The error was calculated by normalizing the standard deviation to the average % $I_{sc}$  drop. The higher error in the  $E_a$  calculation for the MSX 60 modules likely stems from the spread in data as



seen in Fig. 50. About 15 out of 48 data points were removed from the Arrhenius plots (and thus the  $E_a$  calculation) due to non-uniform/patterned browning and cracked cells. Only cells with uniform browning and non-cracked cells were considered for  $E_a$  calculation. The wider spread in the MSX 60 module could be from the two intensities of browning observed in UVF imaging as seen in Fig. 47. The difference in  $E_a$  between the MSX60 and M55 modules could possibly be attributed to the different additive formulations in the EVA used during module fabrication leading to varying encapsulant browning rates and mechanisms.

All the cells in the M55 modules have uniform browning across all cells and have no cracks. In the M55 modules, the overall increase in the browning coverage area is low as compared to that of the MSX 60 modules. Most of the cell area in the M55 modules was already uniformly brown at the start of the accelerated UV exposure whereas in the MSX 60 modules, the cells are non-uniformly browned. The  $E_a$ s calculated are for an intensified encapsulant browning reaction in the MSX 60 and M55 modules with Al tape on the backsheets. The  $E_a$  calculated was used to predict the degradation rate. A degradation was calculated from each of the six field-aged modules and compared to its own field-induced degradation rate.

TABLE XIV: PREDICTED  $I_{sc}$  DEGRADATION RATES BASED ON ACCELERATED UV EXPOSURE. DEGRADATION RATES IN %/YEAR.

	<b>Annual <math>I_{sc}</math> degradation rate (%)</b>			
	<b>Condition</b>	<b>Low T</b>	<b>Mid T</b>	<b>High T</b>
<b>MSX 60</b>	<b>Field</b>	0.26	0.31	0.30
	<b>Accelerated</b>	0.30	0.29	0.30
<b>M55</b>	<b>Field</b>	0.35	0.35	0.28
	<b>Accelerated</b>	0.14	0.14	0.15

The variance in the predicted and field degradation rates could stem from non-uniform module temperatures during the testing. The source of heat for the thermally insulating foamboards used to maintain the modules at different temperatures is the UV lamps. With irradiance changes, the temperature of the module fluctuates. The average module temperature was used for  $E_a$  and AF calculations.

#### 4.1.2 Studying Solder Bond Degradation in Field-Aged Modules

The modified thermal cycle of the IEC 61215 successfully achieved multiple temperatures during the dwell time. The total cycle time was 220 minutes with 15 minutes each at  $-40^{\circ}\text{C}$  and at the elevated temperatures ( $85^{\circ}\text{C}$ ,  $95^{\circ}\text{C}$ , and  $105^{\circ}\text{C}$ ). Within each module, three thermal zone being maintained as shown in Fig. 52. The 10-minute time lag in module temperature catching up to the chamber temperature is due to time required for thermal equilibrium.

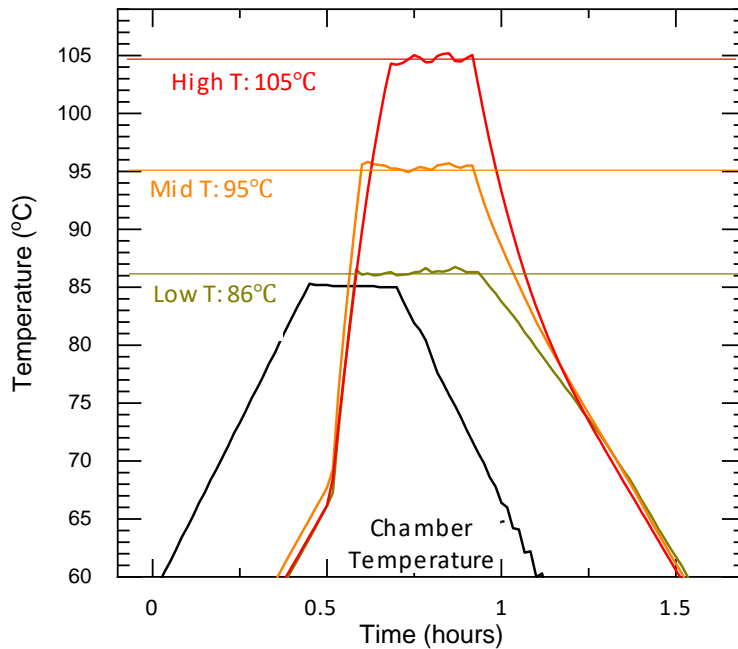


Fig. 52. The achieved thermal profiles of the MSX 60 module with three temperatures during 15 minute dwell time of accelerated TC test. The black line corresponds to chamber temperature.

TABLE XV: DEGRADATION IN IV PARAMETERS OF MSX 60 AND M55 MODULES AFTER THE MODIFIED TC TESTING.

MSX60				
Exposure type		Light IV		Dark IV
		FF (%)	P <sub>max</sub> (W)	R <sub>s</sub> (Ω)
Field	Nameplate	74.7	59.2	0.38*
	21 years	73.1	53.2	0.82
	% Deg.	2.1	10.1	116
	<b>% Deg./year</b>	<b>0.1</b>	<b>0.48</b>	<b>5.51</b>
Testing	0 cycles	73.1	53.2	0.82
	800 cycles	72.3	52.0	1.04
	% Deg.	1.1	2.3	26.8
	<b>% Deg./200 cycles</b>	<b>0.27</b>	<b>0.56</b>	<b>6.7</b>
M55				
Exposure type		Light IV		Dark IV
		FF (%)	P <sub>max</sub> (W)	R <sub>s</sub> (Ω)
Field	Nameplate	72.9	52.9	0.47*
	18 years	57.6	38.1	1.29
	% Deg.	20.9	28	195
	<b>% Deg./year</b>	<b>1.2</b>	<b>1.6</b>	<b>10.9</b>
Testing	0 cycles	57.6	38.1	1.29
	400 cycles	37.2	23.6	3.66
	% Deg.	35.4	38.1	184
	<b>% Deg./200 cycles</b>	<b>17.7</b>	<b>19.0</b>	<b>91.9</b>

The degradation rates of test modules shown in TABLE XV were calculated based on the nameplate rating. The module R<sub>s</sub> before field exposure was calculated by the Dobos method which uses V<sub>oc</sub>, V<sub>mp</sub>, and I<sub>mp</sub> of the module (from the nameplate) [24]. The degradation per year and per 200 cycles is highlighted in red. The annual FF, P<sub>max</sub>, and R<sub>s</sub> field degradation rates were lower in the MSX60 module (21 years) than in the M55 module (18 years) despite the longer field exposure of the MSX60 module. The same trend was replicated in accelerated testing with a consistent drop in FF and P<sub>max</sub> and an increase in the R<sub>s</sub>.

## Module-level Characterization Results

The MSX 60 module underwent much lower degradation than the M55 module in the field despite being having longer field exposure. The  $P_{\max}$  degradation rate is higher than the FF degradation rate for both modules indicating the role of other degradation mechanisms in the field. Over the accelerated TC testing, the % degradation per 200 cycles show that again MSX 60 module underwent much less degradation than the M55 module. Note that the degradation calculated in TABLE XV is for the whole module and not for the individual temperature zones.

### Outdoor IR and EL Imaging

Further information about degradation was obtained via imaging techniques such as EL and IR imaging. In EL images, dark areas correspond to electrically inactive areas. No major changes were observed in EL images between the pre- and post- modified TC800 testing for the MSX60 module in Fig. 53a and Fig. 53c. The EL images for the M55 module in Fig. 53 show an overall module darkening and an increase in bright areas near busbars, which is attributed to electron crowding because of  $R_s$  increase. IR images show thermal anomalies in metallization in the module. The difference in the ambient temperatures (37°C during pre-test IR imaging and 15°C during post-test IR imaging) dictates the module temperature. No new hotspots were observed in the MSX60 (Fig. 53e and Fig. 53g). A few new hotspots were observed in the Mid T and High T zones of the M55 module possibly due to increased  $R_s$  as seen in Fig. 53f and Fig. 53h.

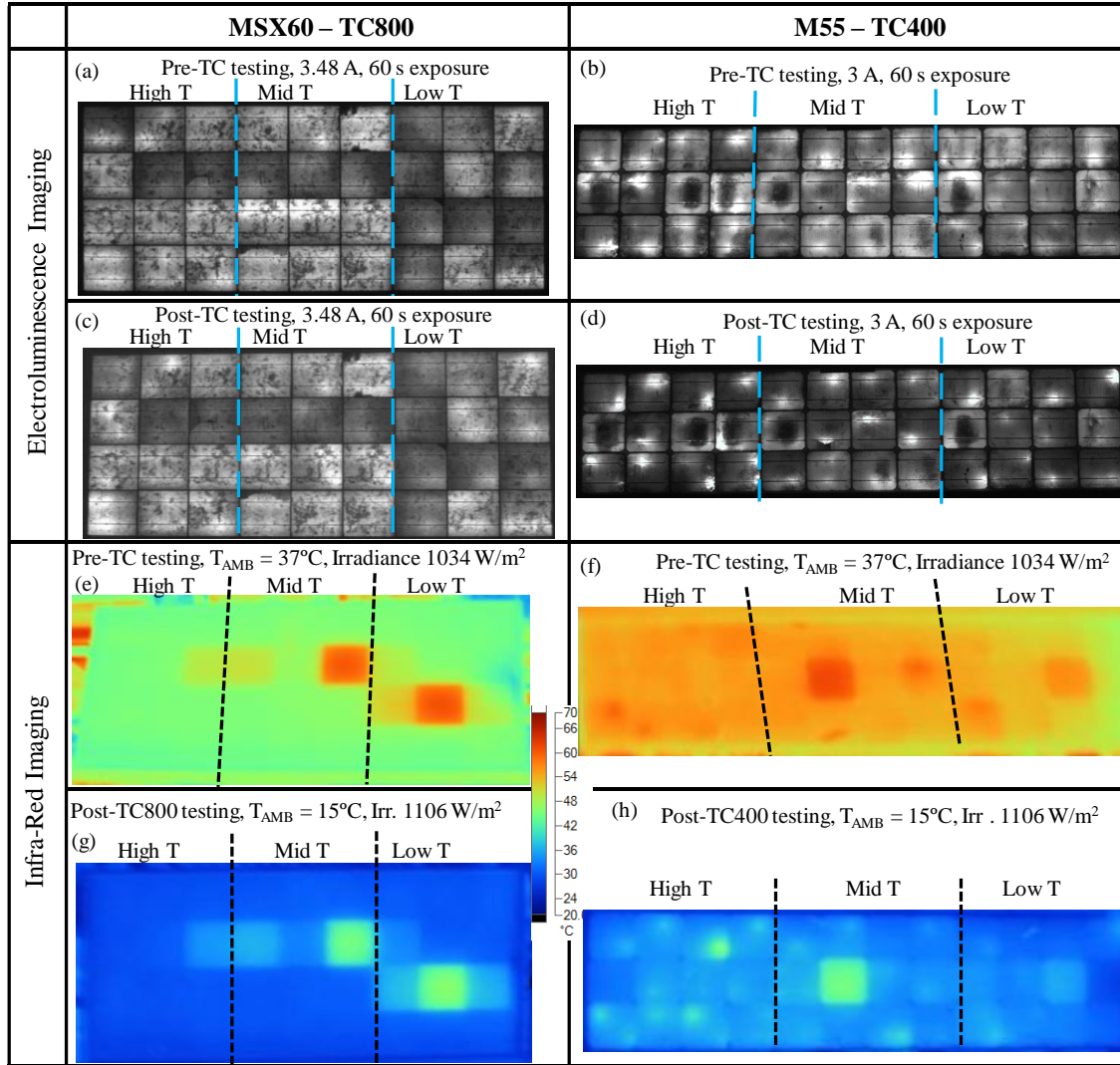


Fig. 53. (a – d) EL and (e – h) IR images of the field-exposed modules before and after thermal cycling. The MSX60 module EL images (a and c) do not show much degradation whereas the M55 module (b and d) shows an overall cell darkening and brightness near the busbars indicate increased  $R_s$  leading to electron crowding. The cells in green on the MSX60 module and the cells in yellow on the M55 module correspond to the cells in IR imaging that have a slightly higher temperature.

### Cell-level Characterization Results

The cell-level  $R_s$  measurements of the M55 module shown in TABLE XVI have a more distinct temperature dependence than the MSX60 module. Again,  $R_s$ , and not  $P_{max}$  is considered as the direct parameter affected by the modified TC testing. To further

understand the changes caused by thermal cycling, SEM imaging and EDXS analysis was done.

TABLE XVI: AVERAGE % CELL-LEVEL  $R_s$  INCREASE IN THE MSX 60 AND M55 MODULES FOR 200 CYCLES

Average % Cell level $R_s$ change/200 cycles	MSX 60			M55		
	Low T	Mid T	High T	Low T	Mid T	High T
	5.33	5.53	6.55	27.60	39.75	50.55

### Electron Imaging and Compositional Analysis

Six samples were imaged and analyzed from the three temperature zones across two modules. Scanning electron micrographs and EDXS compositional maps were obtained at the interfaces where the cell interconnect was bonded to the Ag cell metallization. In MSX60 modules,  $\text{Sn}_{62}\text{Pb}_{36}\text{Ag}_2$  was introduced as a part of the solder layer (during the cell-soldering stage of module manufacturing) but not used in the M55 module. Thus, imaging locations on both module types were carefully chosen to highlight this vital difference.

Large-area SE micrographs showed that most of the solder along the Cu ribbon that was exposed to the EVA layers (near the glass and near the backsheet) had migrated to the interface between the cell interconnect and the Ag busbars for both the MSX60 and the M55 module. Solder in the MSX60 High T sample and the M55 Mid T sample had migrated towards the edges of the Cu core. Fig. 55 lays out the SE micrographs and EDXS maps for Cu, Sn, and Pb across the samples. It is critical to consider the field-exposure and testing history of the MSX60 and the M55 modules while analyzing the SEM images and EDXS maps.

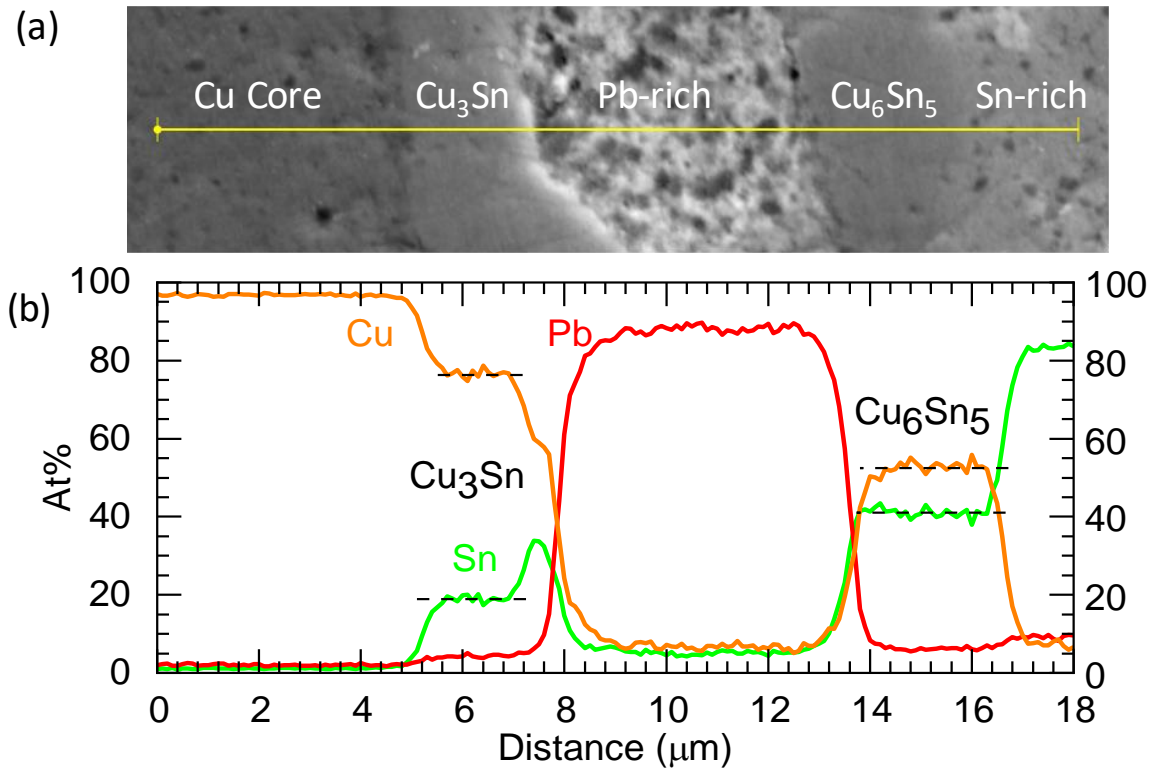


Fig. 54. SEM micrograph of a sample from the MSX 60 Mid T region (a) with a corresponding line scan showing the at% of Pb, Cu, and Sn (b). Between 5  $\mu\text{m}$  and 8  $\mu\text{m}$ , the IMC observed is  $\text{Cu}_3\text{Sn}$ . Some segregation was observed with Pb-rich and Sn-rich phases. The  $\text{Cu}_6\text{Sn}_5$  IMC layer was about 3  $\mu\text{m}$  thick.

Quantitative EDXS distinguished the two  $\text{Cu}_x\text{Sn}_y$  IMCs. From the Cu-solder interface,  $\text{Cu}_3\text{Sn}$  IMC formed with more Sn at the edge showing formation of  $\text{Cu}_6\text{Sn}_5$  IMC. The  $\text{Cu}_6\text{Sn}_5$  IMC was also found further into the solder due to diffusion and creep. In addition to the line scan in Fig. 54, quantitative point scans (not shown here) were performed showing roughly 75 at% Cu and 25 at% Sn for  $\text{Cu}_3\text{Sn}$  and about 60 at% Cu and 40 at% Sn for  $\text{Cu}_6\text{Sn}_5$ .



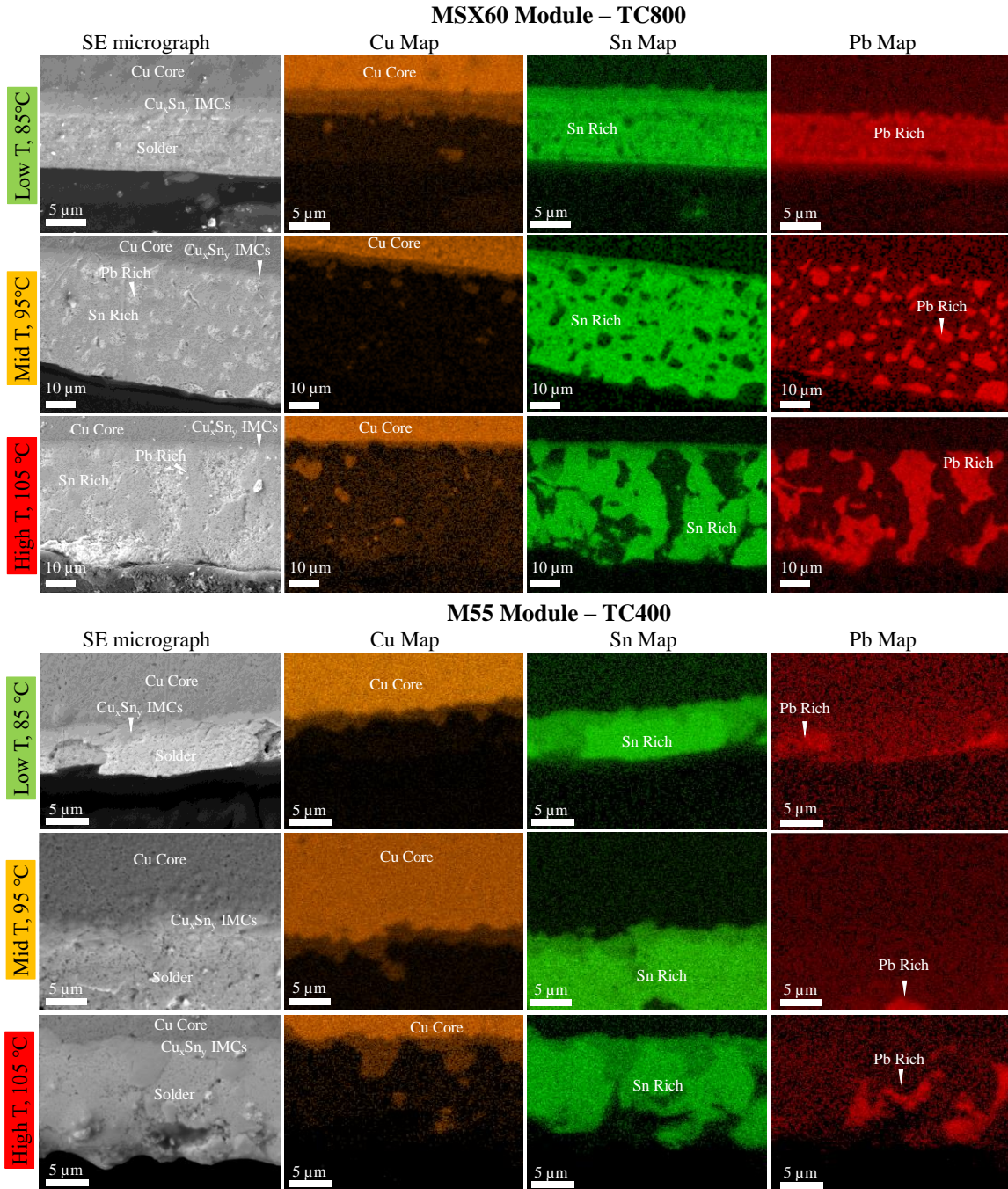


Fig. 55. SE micrographs of cell interconnect cross-sections from the three temperature zones of the MSX60 and the M55 modules along with their corresponding EDXS maps. Note the feature-size appropriate scale bars used in the Mid T and High T sample images of the MSX module. Overlap of Cu and Sn maps indicate at the presence of Cu<sub>3</sub>Sn and Cu<sub>6</sub>Sn<sub>5</sub> IMCs. While the Low T MSX60 sample has a lamellar structure, an increase in the Pb-rich segregation was observed in the Mid T (94 Pb-rich islands with an average area of 14.38 μm<sup>2</sup>) and High T (15 Pb-rich islands with an average area of 82.64 μm<sup>2</sup>) samples. Samples from all temperature zones of the M55 module show major segregation.

In the MSX60 module, the Low T SE micrograph shows a solder layer of uniform thickness. The overlapping areas in the Cu and Sn maps indicate the formation of a thin  $\text{Cu}_3\text{Sn}$  (closer to the Cu core) and  $\text{Cu}_6\text{Sn}_5$  (thicker and next to the  $\text{Cu}_3\text{Sn}$  layer) IMCs. The average IMC layer thickness was  $3.82\ \mu\text{m}$ . The Cu map also shows a few regions of Cu diffused into the Sn-Pb matrix. It is possible that some of these islands could be connected to the Cu core in 3D. The Sn and Pb maps show closely-packed lamellar segregation of Sn-rich and Pb-rich regions. The Sn-Pb layers make it challenging to obtain exact area fractions with respect to the total solder area. The approximate area fractions of Sn and Pb is 0.77 and 0.64, respectively. The samples from the Mid T and High T zones have a uniform solder thickness with visible spots. The Cu maps for both the samples show regions of scalloped  $\text{Cu}_x\text{Sn}_y$  IMCs along with more Cu islands. Average IMC layer thicknesses of  $3.9\ \mu\text{m}$  (Mid T) and  $4.2\ \mu\text{m}$  (High T) were calculated. In both samples, the Pb-rich regions have segregated and coarsened as evident from the Pb maps. The Sn and Pb area fraction for the Mid T region sample was 0.74 and 0.23, respectively. About 94 Pb-rich regions with an average area of  $14.4\ \mu\text{m}^2$  were measured via ImageJ. For the High T region sample, the area fractions were 0.64 (Sn) and 0.34 (Pb), with about 15 Pb-rich regions with an average area of  $82.6\ \mu\text{m}^2$ . With increasing temperature, microstructure coarsened to increased phase separation and more Cu island formation, all of which lead to increased  $R_s$ .

In all of the M55 module samples, a distinct IMC layer was observed from SE micrographs and the Cu maps. Major phase segregation and growth was observed across samples from all temperature zones. Most of the Pb had segregated to form one or two

large regions. The Sn-Pb area fractions, respectively, were 0.93 and 0.13 (Low T), 0.92 and 0.04 (Mid T), and 0.77 and 0.19 (High T). The discrepancy for Low T came from a surface void showing Sn in a Pb-rich region. The average IMC layer thicknesses calculated was 2.2  $\mu\text{m}$ , 2.8  $\mu\text{m}$ , and 3.1  $\mu\text{m}$  for the Low T, Mid T, and the High T zones, respectively. The EDXS measurement uncertainty was 0.2  $\mu\text{m}$ .

Exposure to higher temperatures is conducive to IMC formation which can lead to cracking especially when combined with thermal cycling. There can be a physical separation of the alloys/compounds (phase segregation) upon thermal cycling due to TMF from the differential CTEs. All samples show Pb and Sn segregation along with an increase in the IMC layer thickness with increasing temperature. Cracking, delamination, and grain size increase result in increased  $R_s$ .

## Activation Energy Calculation and Solder Bond Degradation Rate Prediction

The cell-level  $R_s$  increase data was used to calculate the  $E_a$  for solder bond degradation in the MSX60 and M55 modules. Each temperature section was considered to be one unit. The percent cell  $R_s$  increase from all cells within one temperature section was averaged and presented on the Arrhenius plot in Fig. 56. The  $E_a$  was estimated to be 0.12 eV for MSX60 module and 0.35 eV for the M55 module.

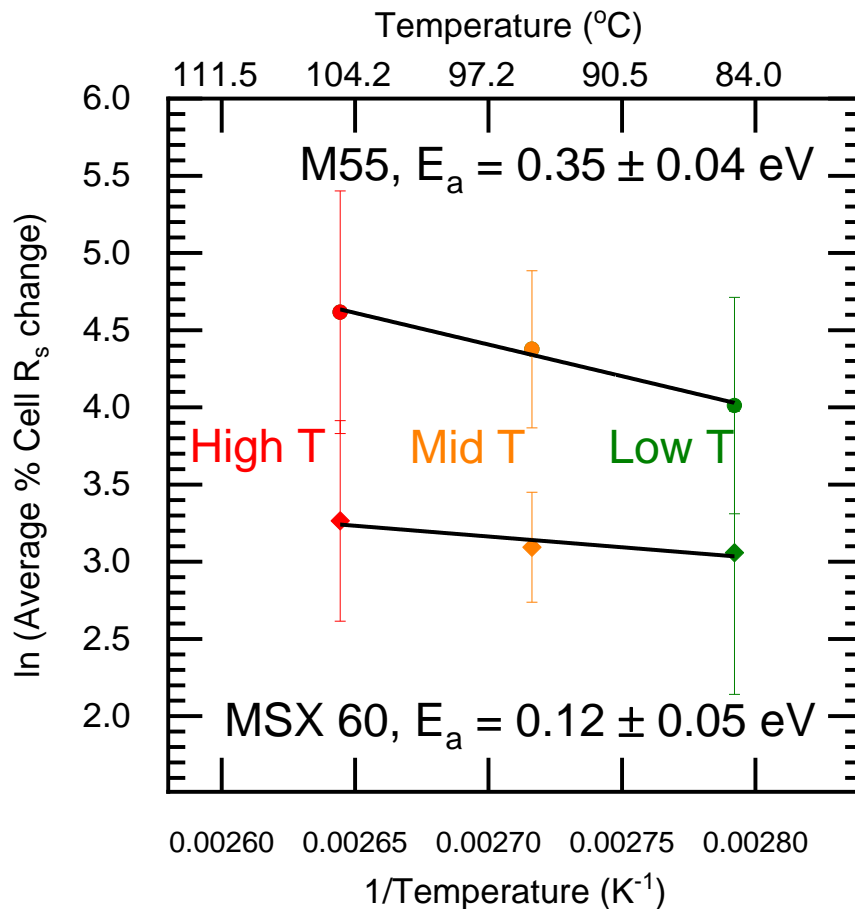


Fig. 56. Arrhenius plot for solder bond degradation with the average  $R_s$  degradation in cells from the MSX 60 and the M55 module. The  $E_a$  calculated for the MSX 60 module was 0.12 eV. The Low T, Mid T, and High T data points represent the average % $R_s$  increase of 7 cells, 5 cells, and 7 cells, respectively. The M55 module was 0.35 eV. The Low T, Mid T, and High T data points represent the average % $R_s$  increase of 6 cells, 9 cells, and 5 cells, respectively.

Based on literature reported values [48], [50], [52], the increase in the  $R_s$  seems to be dominated by TMF more than by IMC formation in the MSX60 module. With IMC formation and increasing grain size, crack initiation and propagation occurring at interfaces is easier [100]. However, the presence of 2wt% Ag in the solder joints of the MSX 60 module likely inhibited much of the IMC formation and grain coarsening in the field [52], [76], [77], [101], [102]. The grains of Pb in the Sn<sub>60</sub>Pb<sub>40</sub> solder (M55) further coarsen in addition to IMC formation. The reported  $E_a$  values for TMF induced degradation are 0.12 eV and 0.46 eV [48], [50]. Geipel et al. have reported 0.89 eV - 1.34 eV as  $E_a$  for IMC formation in Sn<sub>60</sub>Pb<sub>40</sub> solders [52]. In both modules, solder bond degradation seems to be dominated by TMF. The high variability in the  $R_s$  could be attributed to non-uniformity in heating and therefore in the degradation measured.

The  $E_a$  (0.12 eV and 0.35 eV) obtained was through the  $R_s$  increase in cells of field-aged modules subjected to thermal cycling. In this work, the IMCs in the modules—formed during soldering and lamination and grown during field exposure—underwent further crack formation and propagation in the modified thermal cycling test. The parameter directly affected by the presence of IMCs and the TMF further induced by thermal cycling was  $R_s$  and its relative increase was used for  $E_a$  calculation. The  $E_a$  reported by Geipel et al. is 0.89 eV – 1.34 eV based on IMC growth in freshly fabricated samples subject to isothermal aging. The effect of crack formation and growth was not accounted for in the  $E_a$  calculation. The IMC thickness increases with increased exposure to isothermal conditions.

Both modules have 18 – 21 years of field exposure in Arizona during which the majority of the IMCs present would have formed. In the modified TC test, TMF is expected to dominate due to the testing profile. Out of the 220-minute cycle, only 15 were spent at elevated temperatures (which encourage IMC formation). With another 15 minutes at -40°C, a total of 190 minutes was spent ramping up and down in temperature. During this time, TMF was expected to dominate over IMC formation. It is theorized that the reduced silver scavenging effect of the 2wt% Ag in the MSX60 solder joint reduced IMC formation and the effects of TMF when compared to the M55 solder material—which does not contain any silver at all [77]. With IMC formation and increasing grain size, crack initiation and propagation occurring at interfaces is easier [100]. The  $E_a$  can also be influenced by the variance in module/cell temperature during the dwell time.

The average  $R_s$  degradation rate in the field was calculated to be 1.04%/year for the MSX 60 modules. For M55 modules, the degradation rate was 3.04%/year in the field. With an  $E_a$  of 0.27 eV, the predicted degradation rate was 0.19% and with an  $E_a$  of 0.35 eV, the predicted rate is 0.26%/year. The low predicted degradation rate could be attributed to the short dwell time of 15 minutes at the upper temperatures.

4.2 Accelerated Stress Testing to Induce Encapsulant Browning And Solder Bond Degradation in Freshly Fabricated 9-cut-cell Samples

4.2.1 UV-T exposure of 9-cut-cells with either UV-cut and UV-pass EVA above and below the cell

The approach of having thermally insulating foamboards of varying thicknesses to maintain the samples at varying temperatures was successfully demonstrated. UVF images show the extent and intensity of browning in the UVC EVA samples. With the UVP EVA samples, no obvious browning is seen in Fig. 57. The UVC1 sample at 800 kWh/m<sup>2</sup> has cracks due to a fall. This is apparent through the pattern of encapsulant browning intensified due to the Al tape on the backsheet of the samples.

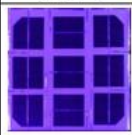
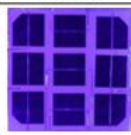
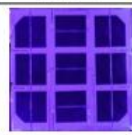
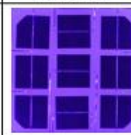


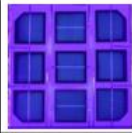
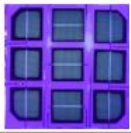
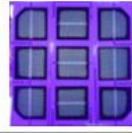
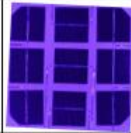


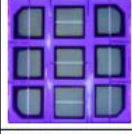
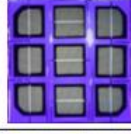
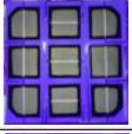
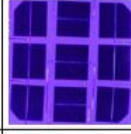


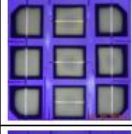
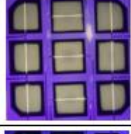
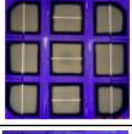
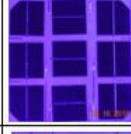



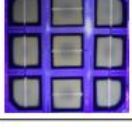

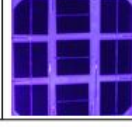


Coupons	UVC 1	UVC 2	UVC 3	Coupons	UVP 1	UVP 2	UVP 3
Temperature	60.9°C	66.2°C	72.5°C	Temperature	59.3°C	66.5°C	69.9°C
0 kWh/m <sup>2</sup>				0 kWh/m <sup>2</sup>			
200 kWh/m <sup>2</sup>				200 kWh/m <sup>2</sup>			
400 kWh/m <sup>2</sup>				400 kWh/m <sup>2</sup>			
600 kWh/m <sup>2</sup>				600 kWh/m <sup>2</sup>			
786 kWh/m <sup>2</sup>				786 kWh/m <sup>2</sup>			

Fig. 57. UVF images of the 9-cut-cell samples with UVC EVA and UVP EVA at every 200 kWh/m<sup>2</sup>.

The cell-level  $I_{sc}$  in Fig. 58 show a 2.0%, 3.7%, and 4.2%  $I_{sc}$  drop in UVC1, UVC2, and UVC3 samples, respectively. The  $I_{sc}$  drop in UVP1, UVP2, and UVP3 samples was 3.1%, 4.4%, and 4.9%, respectively. The similar  $I_{sc}$  drop between the UVC and UVP samples indicate that a degradation mode other than browning is involved. The YI values shown in Fig. 58b increase consistently for UVC samples with increasing temperature. In the UVP sample, the YI values show a negligible increase.

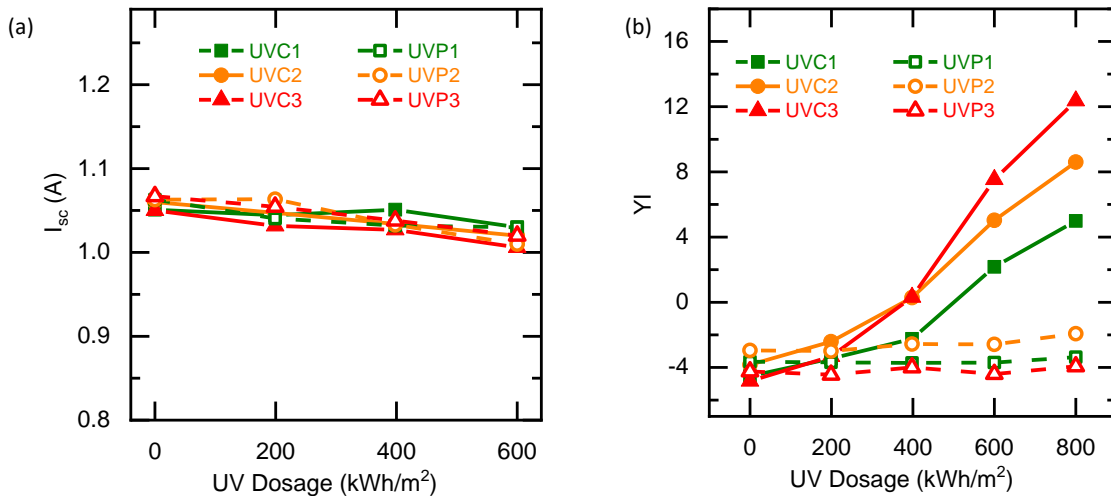


Fig. 58. (a)  $I_{sc}$  change after every 200 kWh/m<sup>2</sup> until 600 kWh/m<sup>2</sup> show little drop. (b) YI change over the duration of the test. The YI increase in the UVC samples indicate that encapsulant browning is the likely degradation mode whereas the negligible change in the YI of the UVP mini-modules indicate a different degradation mode.

To explain the  $I_{sc}$  drop and negligible YI increase, a closer look at one cell from the UVC3 and the UVP3 samples is necessary (Fig. 59). The extent of encapsulant browning extends to the edges of the cell. The peripheral clear ring is indicative of photobleaching. It is possible that the adhesive of the Al tape on the backsheet of the samples was weakened due to the extended exposure at elevated temperatures. The weakened adhesive allowed



limited air diffusion through the backsheet enabling photobleaching of the cell periphery. With higher sample temperatures supporting greater photobleaching, UVC3 is expected to have more clear space on the cell periphery than the UVC2 or UVC1 samples. However, UVC2 and UVC3 have 0.5” and 2” thick insulating foamboards that can further affect the rate of oxygen diffusion through the backsheet. In contrast, the UVC1 sample has no foamboard on the backsheet.

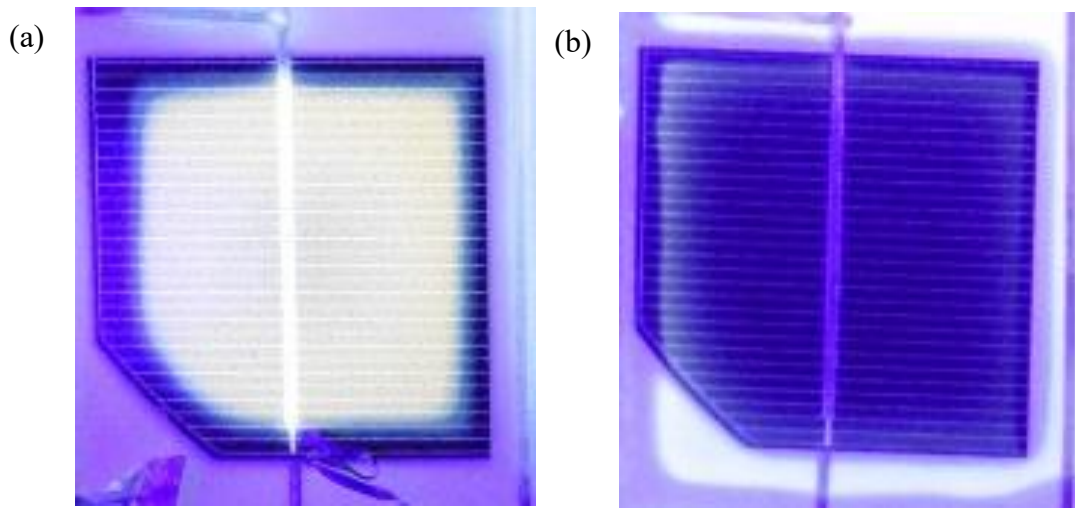


Fig. 59. Close-up UVF images of one cell from the (a) UVC3 and the (b) UVP3 samples. The area of browning is clearly seen in the UVC3 sample. A ring like pattern is seen in the UVP3 sample that could be attributed to EVA main chain degradation.

4.2.2 Combined UV-T-RH Accelerated Testing of PV Modules: Reliability of UV-Cut and UV-Pass EVA Encapsulants

9-cut-cell samples were maintained at multiple temperatures exposed to humidity. UVF imaging (Fig. 60) shows the extent of browning in the modules.

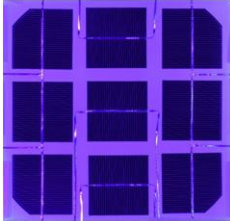
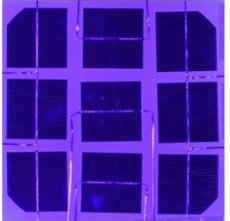
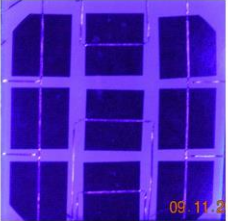
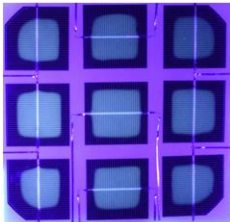
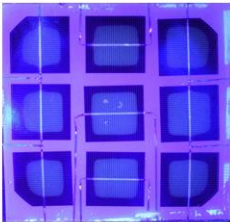
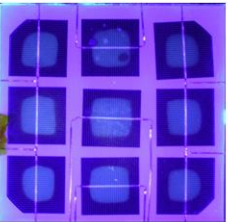

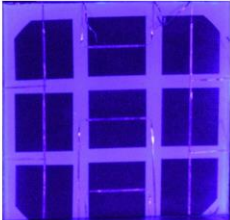
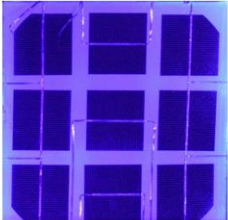
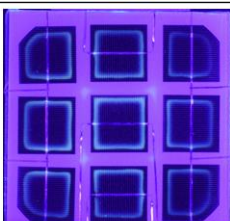
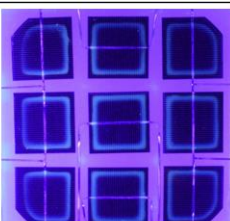
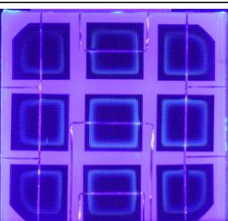
Coupons	UVC 1	UVC 2	UVC 3
Temperature	64.4°C	60.3°C	63.1°C
% RH	11.2	54.4	28.9
0 kWh/m <sup>2</sup>			
200 kWh/m <sup>2</sup>			
Coupons	UVH 1	UVH 2	UVH 3
Temperature	60.7°C	56.7°C	67.1°C
% RH	11.2	54.4	28.9
0 kWh/m <sup>2</sup>			
200 kWh/m <sup>2</sup>			

Fig. 60. UVF imaging of UVC and UVH samples at different temperatures and humidities. The extent of encapsulant browning and influence of oxygen diffusion can be seen. The ring-like feature is browning.

As the temperature increases, the extent and intensity of browning increases. Diffusion of oxygen through the backsheet enables oxygen photobleaching as seen by the clear peripheral rings on all cells. A ring of fluorescence was seen in the 9-cut-cell samples with UVP EVA above the cell. This could be due to additive migration from the back UVC EVA layer to the front UVP EVA layer during lamination [24]. Ring-like fluorescence pattern has been reported in modules with UVC EVA below the cell and UVP EVA above the cell [35], [103] and also in UV-chamber aging [104]. The increased fluorescence could be due to agglomerated fluorophores [105].

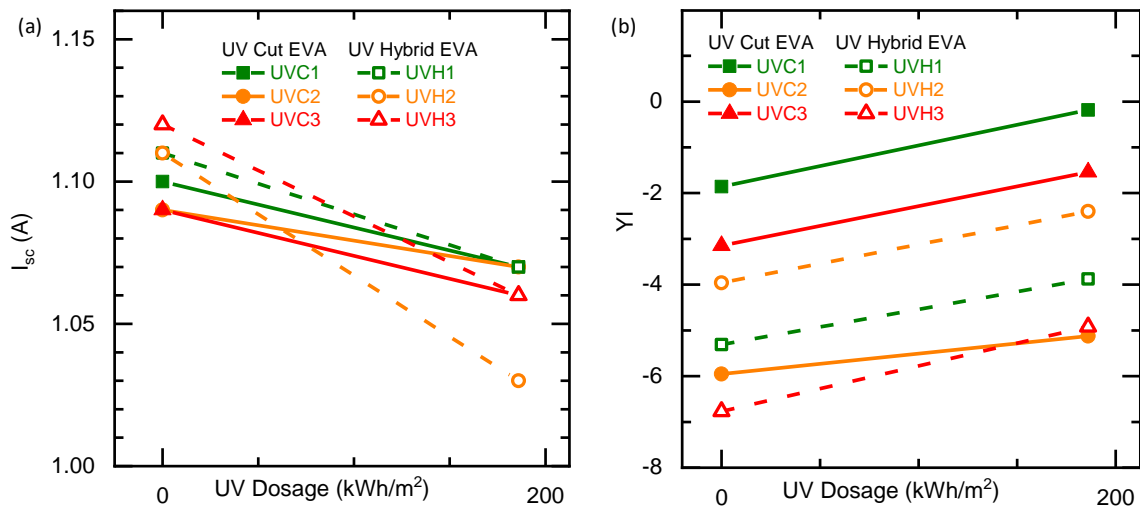


Fig. 61. (a) Median  $I_{sc}$  drop in the six 9-cut-cell samples after 186 kWh/m<sup>2</sup> of UV dosage. (b) The YI plot shows a consistent increase YI data for all 9-cut-cell samples.

A consistent  $I_{sc}$  drop and a YI increase was measured in all the samples. However, since the  $I_{sc}$  change measured was within the measurement uncertainty, we are not able to use this data to further calculate the  $E_a$ .

### 4.2.3 Combined UV-T-RH Accelerated Testing of 9-cut-cell Samples

Two sets of six 9-cut-cell samples each were exposed to UV-T and UV-T-RH. In the previous experiments, the samples were maintained at elevated temperatures using the passive heating method of having insulating foamboards of varying thicknesses behind the samples. The caveat of this approach was that the sample temperature directly fluctuated with the incident UV light intensity. Despite the use of heating blankets aimed at maintaining samples at multiple temperatures, for the UV-T samples, three different temperatures could not be maintained. This is likely due to the lack of a box enclosing the samples thus retaining heat from the blanket. Heat from the blankets was dissipated to the ambient within the walk-in UV chamber. In the case of UV-T-RH, samples were placed within an enclosed box to contain the steam. The enclosure helped to maintain the temperature of the samples with heating blankets.

TABLE XVII: SAMPLE TEMPERATURES OBTAINED WITH THE HELP OF SILICONE HEATING BLANKETS. DUE TO THE LACK OF AN ENCLOSURE BOX, DISTINCT SAMPLE TEMPERATURES COULD NOT BE MAINTAINED IN THE UV-T SAMPLES.

Module and Condition		Temperature (°C)			
		UV-T	Std. Dev	UV-T-RH	Std. Dev
TPT	Low T	61	4.6	66	3.5
	Mid T	65	3.8	74	2.6
	High T	82	8.4	83	4.6
KPE	Low T	61	5.4	63	3.6
	Mid T	65	4.4	70	2.7
	High T	73	9.2	78	5.0

A one-inch gap was maintained between the sample and the heating blanket so as to allow only radiative heating and not damage the backsheet. With increasing temperatures, more browning and degradation is expected. The browning of these samples was characterized by UVF imaging, colorimetry, reflectance, and  $I_{sc}$  measurements.

Colorimetry results shown in TABLE XVIII, do not show a distinct trend. In the negative range, the YI indicates an increase in the blue wavelength corresponding to reflectance of the solar cell. Currently, the UV exposure maybe insufficient to cause an adequate increase in the YI.

TABLE XVIII: YI VALUES AVERAGED FROM 18 SPOTS ON EACH UVH SAMPLE EXPOSED TO ACCELERATED UV LIGHT AT ELEVATED TEMPERATURES WITH AND WITHOUT HUMIDITY

Module and Condition		UV-T (kWh/m <sup>2</sup> )			UV-T-RH (kWh/m <sup>2</sup> )		
		0	225	$\Delta$ YI	0	225	$\Delta$ YI
TPT	Low T	-1.69	-0.24	<b>1.45</b>	-1.41	-0.31	<b>1.10</b>
	Mid T	-4.34	-3.09	<b>1.26</b>	-5.06	-3.58	<b>1.48</b>
	High T	-3.22	-1.52	<b>1.71</b>	-6.81	-5.73	<b>1.09</b>
KPE	Low T	-4.27	-3.19	<b>1.08</b>	-4.30	-3.64	<b>0.66</b>
	Mid T	-2.97	-1.71	<b>1.26</b>	-8.49	-7.33	<b>1.17</b>
	High T	-1.85	-0.74	<b>1.10</b>	-4.93	-4.15	<b>0.78</b>

TABLE XIX: PERCENTAGE DECREASE IN AVERAGED  $I_{sc}$  VALUES FROM SAMPLES EXPOSED TO ACCELERATED UV LIGHT AT ELEVATED TEMPERATURES WITH AND WITHOUT HUMIDITY. EACH DATA POINT IS AN AVERAGE OF 9 CELLS

Module and Condition		Low T	Mid T	High T
UV-T	TPT	9.70	9.05	9.99
	KPE	10.38	10.94	9.88
UV-T-RH	TPT	9.89	9.70	10.34
	KPE	10.34	10.19	10.56

$I_{sc}$  measurements from each 9-cut-cell sample were measured before and after UV exposure and averaged as shown in

TABLE XIX. As the temperature increases, a higher decrease in  $I_{sc}$  is expected. The KPE samples have a greater drop in  $I_{sc}$  (except the High T UV-T sample) than the TPT samples. The boxplot in Fig. 62 shows the spread of data points within each sample. Though the samples have undergone 225 kWh/m<sup>2</sup> of UV exposure at multiple elevated temperatures, a distinct temperature dependent trend was not observable. This is possibly due to non-uniform browning in the shape of an inward advancing ring as seen in Fig. 63 and Fig. 64.

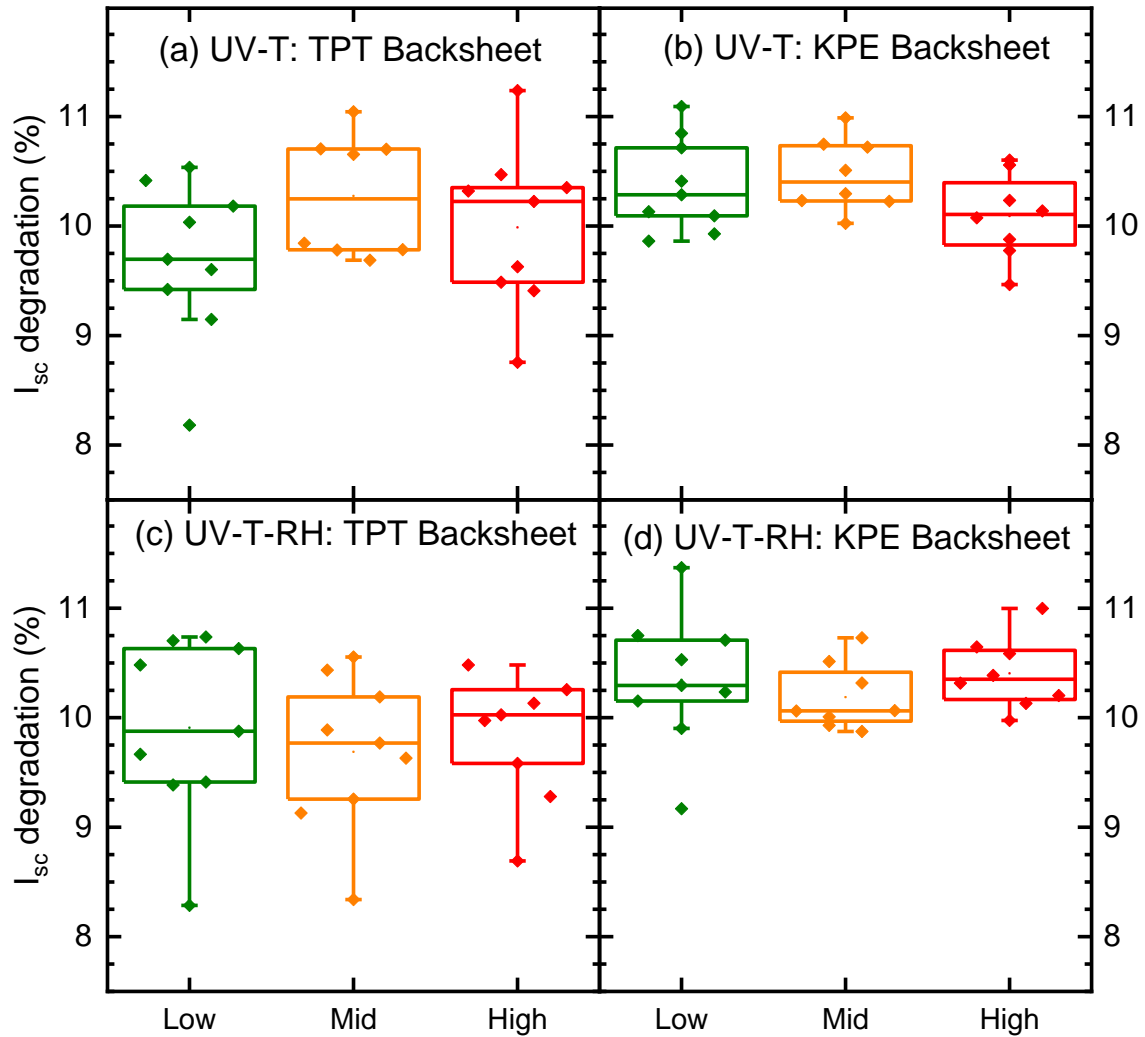


Fig. 62. Box plots of (a) samples with TPT backsheets in the UV-T test, (b) samples with KPE backsheets in the UV-T, (c) samples with TPT backsheet in the UV-T-RH test, and (d) samples with the KPE backsheet in the UV-T-RH test.

UVF images of the samples are shown in Fig. 63 (UV-T) Fig. 64 (UV-T-RH). Some general observations applicable to all samples across UV-T and UV-T-RH. A ring like browning pattern was observed where the thickness or width of the browning ring increased with an increase in the sample temperature. This is consistent with results from the experiment in the previous section. Thicker/wider browning rings in samples with TPT backsheet suggest the KPE backsheet has a higher oxygen permeability than the TPT

backsheet. As the sample temperature increases, so does the rate of oxygen photobleaching. For samples with TPT backsheets, the outside edges of the cells seem to undergo more oxygen photobleaching than the “inside facing” sides of the cells. This could be due to faster heat dissipation through the sample edges leading to locally lower cell temperatures. This suggests that for KPE backsheets, the sample temperatures may have been more uniform. Samples exposed to UV-T-RH have spread-out browning rings with more diffuse borders when compared to samples exposed to UV-T. The presence of humidity would lead to acetic acid formation which is an auto-catalyst. The higher sample temperature enables quicker and further diffusion of water within the sample. The browning ring seems to travel inward faster in the UV-T-RH samples. With more exposure to UV light, the ring of browning travels inward as most evident by the High T TPT backsheet sample exposed to UV-T-RH in Fig. 64. If the samples had a glass/glass construction, browning starting over the cell periphery would be expected to spread inwards as there would be no photobleaching without diffusion through the substrate.

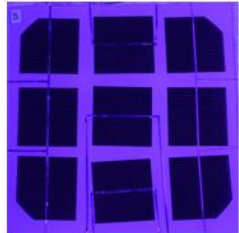
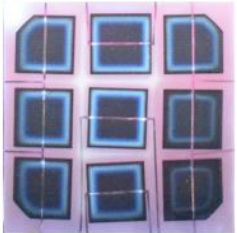
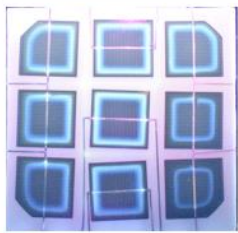
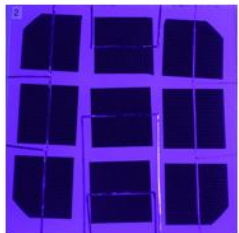
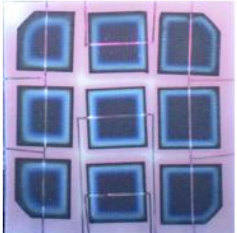
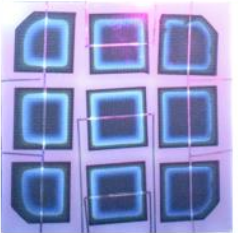
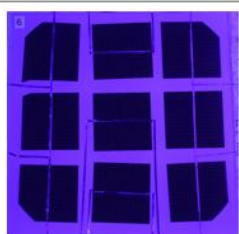
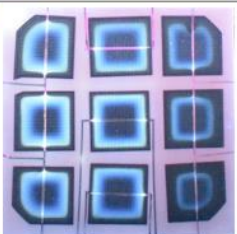
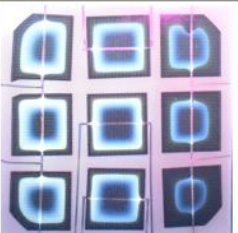
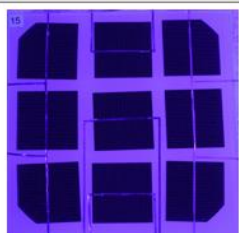
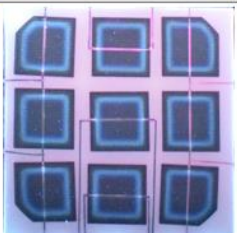
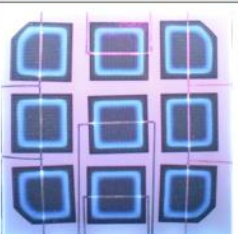
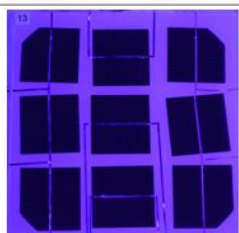
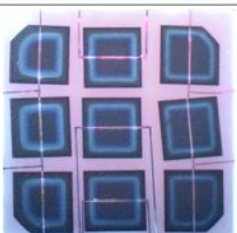
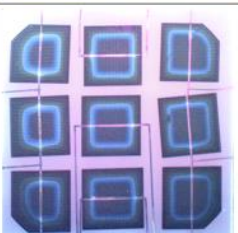
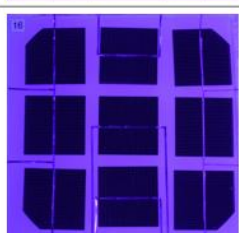
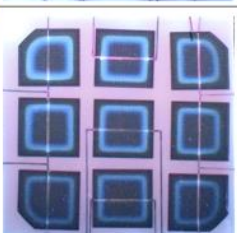
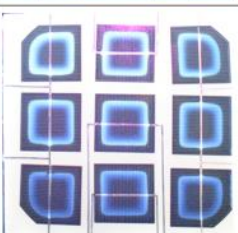
Module		UV-T		
		0 kWh/m <sup>2</sup>	160 kWh/m <sup>2</sup>	225 kWh/m <sup>2</sup>
TPT Backsheet	Low T 61°C			
	Mid T 65°C			
	High T 82°C			
KPE Backsheet	Low T 61°C			
	Mid T 65°C			
	High T 73°C			

Fig. 63. UVF images of 9-cut-cell samples during the 225 kWh/m<sup>2</sup> of UV exposure at elevated temperatures without humidity.



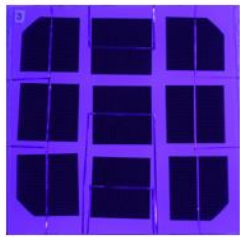
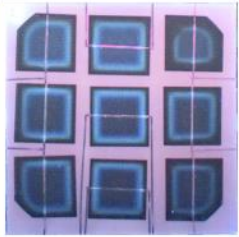
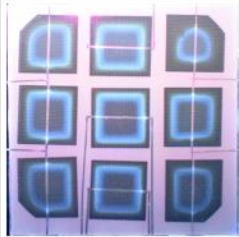
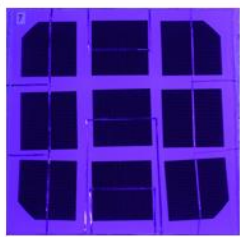
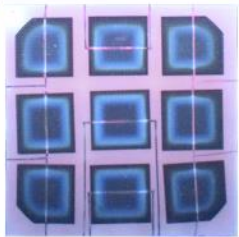
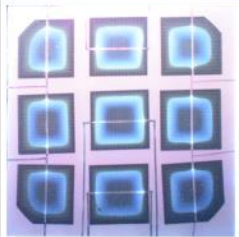
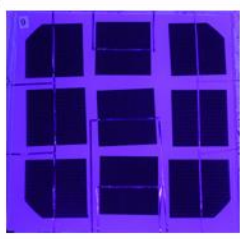
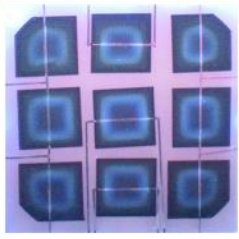
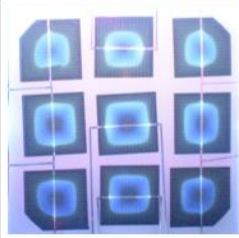
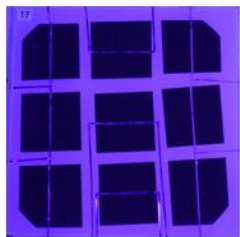
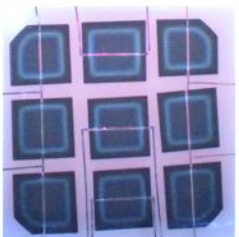
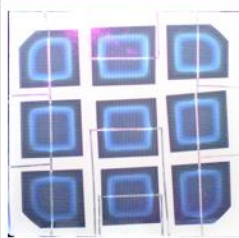
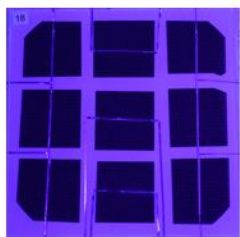
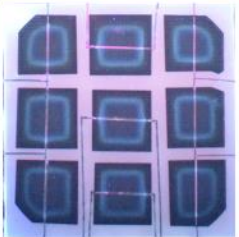
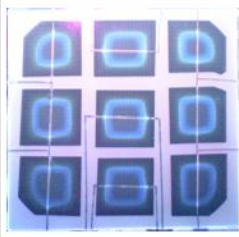
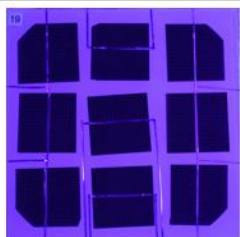
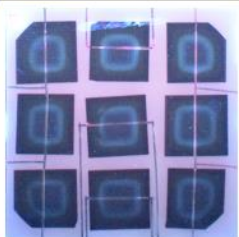
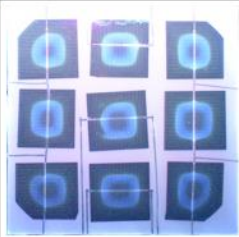
Module		UV-T-RH (RH between 20% - 40%)		
		0 kWh/m <sup>2</sup>	160 kWh/m <sup>2</sup>	225 kWh/m <sup>2</sup>
TPT Backsheet	Low T 66°C			
	Mid T 74°C			
	High T 83°C			
KPE Backsheet	Low T 63°C			
	Mid T 70°C			
	High T 78°C			

Fig. 64. UVF images of 9-cut-cell samples during the 225 kWh/m<sup>2</sup> of UV exposure at elevated temperatures and humidity.

One possible explanation of the ring like browning observed is presented. A small amount of the UV absorber from the UVC EVA below the cells diffuses to the UVP EVA above the cells during the lamination which takes place at 150°C for 20 minutes (Fig. 65a). In the UVP EVA layer, the inter-cell regions have more UV absorber than the region above the cells (since the absorber cannot diffuse through silicon). There is more UV absorber at the interface between the two EVA layers than at the interface of the UVP EVA and the glass.

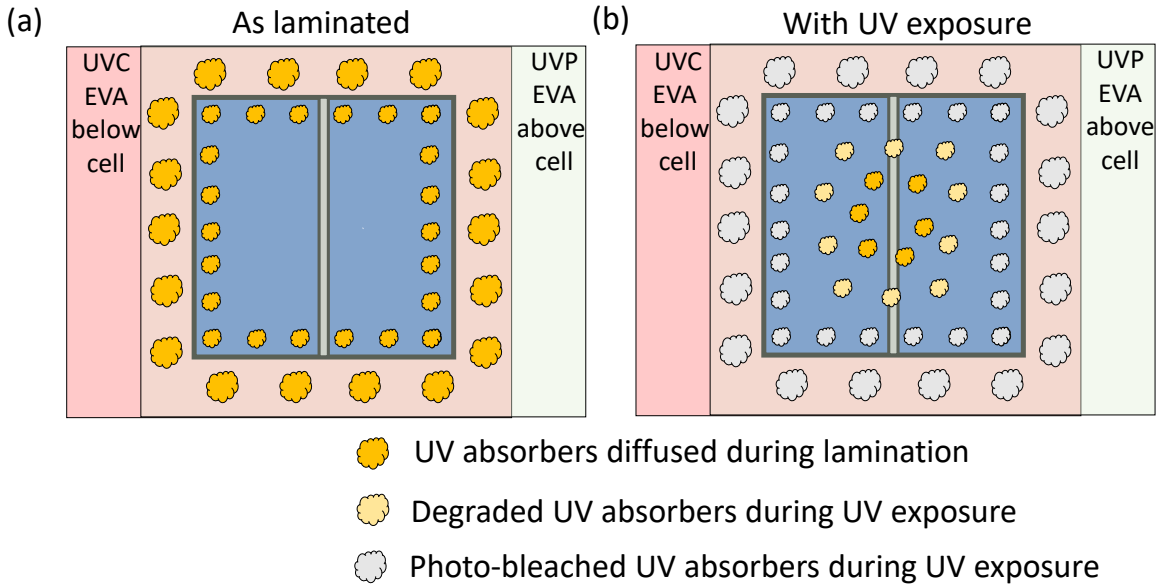


Fig. 65. Schematic showing the possible pathways of encapsulant browning and subsequent oxygen photobleaching due to the movement of UV absorbers during lamination.

With exposure to UV light, the UV absorber closer to the glass starts to degrade and form chromophores. The unreacted UV absorbers starts to diffuse inwards to the cell center as evident by the UVF images due to the concentration gradient over the cell. A simultaneously occurring reaction is oxygen photobleaching where ambient oxygen diffuses through the backsheets and reverses the effect of chromophore formation (Fig.

65b). It is important to remember that the rate of oxygen photobleaching is lower than the rate of EVA browning due to the higher intensity of incident UV light. The limiting factor is the permeability of the backsheet to oxygen.

The reflectance data was obtained for 18 spots as shown in Fig. 36. Due to the symmetric nature of the uniform browning (Fig. 63 and Fig. 64), a median of the reflectance data was calculated for each 9-cut-cell sample and plotted as shown in Fig. 66.

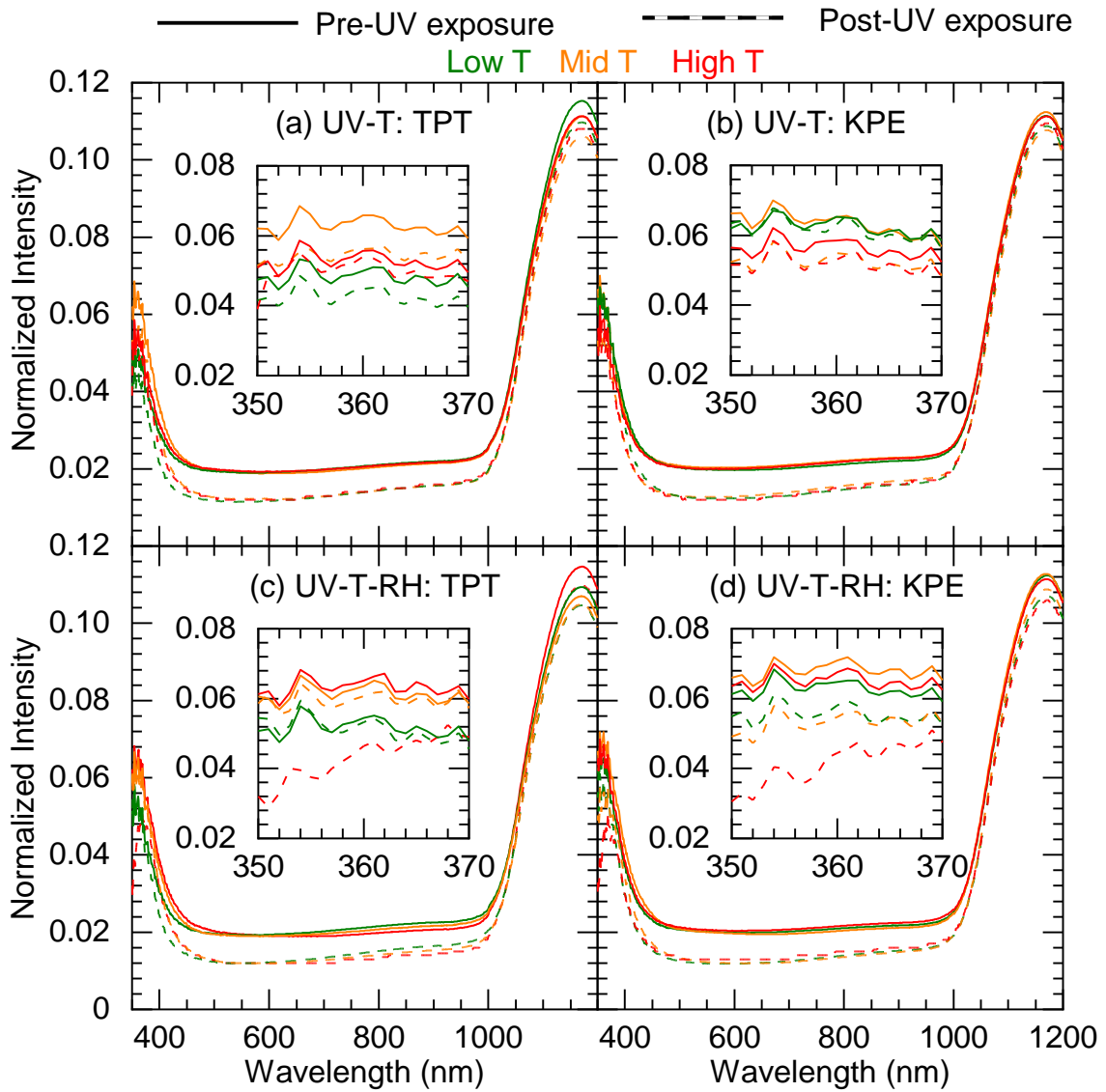


Fig. 66. Reflectance measurements before and after UV exposure (a) and (b) with elevated temperatures and (c) and (d) with elevated temperatures and relative humidity. Each line is the median of 18 measurements from each 9-cut-cell sample. The inset figures show a decrease in reflectance between 350 nm – 370 nm indicating an increase in the absorbance.

In the wavelength range of 350 nm – 370 nm, a considerable decrease in the reflectance was observed in the High T samples exposed to UV-T-RH. The drop could be indicative of an increase in absorbance in the UV range due to absorber diffusion during lamination or the deterioration of the anti-reflection coating. A drop in reflectance was observed in the 1000 nm – 1200 nm range. Between 370 nm – 1000 nm, a drop in reflectance was observed across all samples and condition sets. The decrease in reflectance implies an increase in the absorbance in the EVA layer. The transmittance of the glass is not affected by the stressors. The decrease in the reflectance is due to light passing through the degraded EVA twice: on the way to the cell and after being reflected from the cell. The summarized findings of the exposure of 9-cut-cell coupons to UV-T (TABLE XX) and to UV-T-RH (TABLE XXI) are presented in Fig. 67. There is a distinct difference between the browning pattern of the samples with UVC EVA above the cell and UVP EVA above the cell. The samples with UVC EVA above the cell had uniform browning whereas a ring-like browning pattern was observed in samples with UVP EVA above the cells.

The interplay between the rate of encapsulant browning and oxygen photobleaching presents a challenge in calculating the  $E_a$  as do the fluctuations in stressor intensity over the testing duration. In accelerated testing, the rate of browning is greater than that in real life whereas the rate of oxygen photobleaching remains the same possibly leading to very low  $E_a$  values for some sample sets. In the sample with UVP-UVP EVA, not much fluorescence observed. In the samples with UVC-UVC EVA, uniform and intense

browning was observed across the cell. In all samples with UVP-UVC EVA, a ring-like browning feature was observed across both backsheets and conditions sets. With increasing UV dosage and temperature, the intensity and extent of browning increases. The borders of the rings are less distinct in samples exposed to UV light with humidity.

TABLE XX: SUMMARY OF 9-CUT-CELL SAMPLES EXPOSED TO UV-T WITH VARYING INTENSITIES OF STRESSORS.

EVA Type		Backsheet	UV Dosage	Test Conditions	Main Findings	
Above	Below				Browning	Photobleaching
UVC	UVC	TPT	UV-T (786 kWh/m <sup>2</sup> ) Page 96	61°C - 73°C, Al tape on the backsheet	Intense and uniformly spread out	Thin band limited to cell edges
UVP	UVP	TPT	UV-T (786 kWh/m <sup>2</sup> ) Page 96	59°C - 70°C, Al tape on the backsheet	Light and uniformly spread out	Thin band limited to cell edges
UVC	UVC	TPT	UV-T-RH (200 kWh/m <sup>2</sup> ) Page 99	60°C - 64°C, RH levels: 11% - 55%	Intense and uniformly spread out	Wider band at the cell edges

111

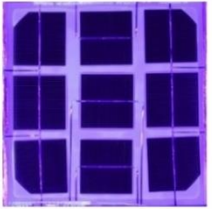

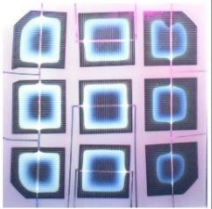
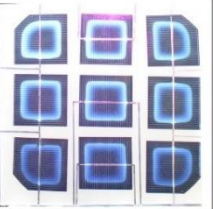
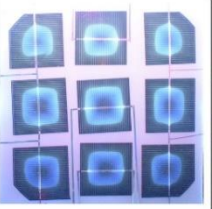
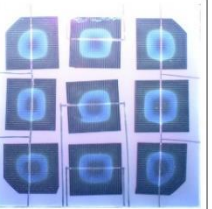
Dosage (kWh/m <sup>2</sup> )	200	200	225 (Without RH)		225 (With RH)	
EVA Type						
EVA Above Cell	UVP	UVC	UVP		UVP	
EVA Below Cell	UVP	UVC	UVC (TPT)	UVC (KPE)	UVC (TPT)	UVC (KPE)
Temperature (°C)	70	73	81	68	82	79
Final						

Fig. 67. Comparative UVF images with varying EVA combinations showing the effect of EVA type on extent and pattern of encapsulant browning.

TABLE XXI: SUMMARY OF 9-CUT-CELL SAMPLES EXPOSED TO UV-T-RH WITH VARYING INTENSITIES OF STRESSORS.

EVA Type		Backsheet	UV Dosage	Test Conditions	Main Findings	
Above	Below				Browning	Bleaching
Common observation for samples with UVP EVA above cells and UVC EVA below cells					Ring-like starting at cell edges and traveling inward	Ring-like starting at the cell edges and following the browning ring
UVP	UVC	TPT	UV-T-RH (200 kWh/m <sup>2</sup> ) Page 99	57°C - 67°C, RH levels: 11% - 55%	Ring moves closer to center with increasing sample temperature	Higher temperature encourages bleaching
UVP	UVC	TPT	UV-T (225 kWh/m <sup>2</sup> ) Page 101	61°C - 82°C No humidity	Width of intense browning ring follows temperature increase	Higher temperature results in more bleaching
UVP	UVC	KPE	UV-T (225 kWh/m <sup>2</sup> ) Page 101	61°C - 73°C No humidity	Width increases with temperature but is smaller than TPT backsheet ring width	Smaller ring width suggests higher backsheet oxygen permeability
UVP	UVC	TPT	UV-T-RH (225 kWh/m <sup>2</sup> ) Page 101	66°C - 83°C RH levels: 20% - 40%	Rings are wider with less distinct ring borders	More oxygen photo-bleaching than samples without humidity
UVP	UVC	KPE	UV-T-RH (225 kWh/m <sup>2</sup> ) Page 101	63°C - 78°C RH levels: 20% - 40%	Extent of browning similar to TPT samples	More oxygen photo-bleaching than samples with TPT backsheet.

#### 4.2.4 Studying Solder Bond Degradation in 9-cut-cell Samples

A set of six samples underwent the modified thermal cycling profile and were maintained at three distinct temperatures during the hot dwell time. Possibly due to the setup (Fig. 42) and distance between the heating blankets and the sample, sample temperatures could not be maintained exactly at 85°C, 95°C, 105°C. In previous experiments, the blankets were placed directly on the module backsheet which allowed for accurate temperature control.

TABLE XXII: SAMPLE TEMPERATURES OBTAINED WITH THE HELP OF SILICONE HEATING BLANKETS OVER 456 MODIFIED THERMAL CYCLES. THE AVERAGE OF SAMPLES TEMPERATURES ABOVE 75°C, 85°C, AND 95°C WERE TAKEN FOR THE LOW T, MID T, AND HIGH T SAMPLES, RESPECTIVELY.

Module and Condition		Temperature (°C)	Std. Dev (°C)
TPT	Low T	80.2	2.9
	Mid T	91.8	3.2
	High T	103.6	8.0
KPE	Low T	78.1	1.7
	Mid T	88.4	2.1
	High T	102.7	6.5

The change in  $R_s$  was measured through DI-V, EL imaging, and IR imaging. In the 9-cut-cell samples, each “column” of cells had a different solder bond composition as shown in Fig. 41 and is considered in the analysis. The left “column” has  $Pb_{36}Sn_{62}Ag_2$ , the middle “column” has  $Pb_{40}Sn_{60}$ , and the right “column” has  $Sn_{42}Bi_{58}$  solder-coated ribbons. The increase in  $R_s$  was measured through Dark I-V and is presented in TABLE XXIII.

TABLE XXIII: THE % INCREASE IN  $R_s$  USING DARK I-V BASED ON SOLDER BOND COMPOSITION AND SAMPLE TEMPERATURE DURING THE HOT DWELL TIME. EACH DATA POINT IS AN AVERAGE OF 6 CELLS.

Solder type	Low T	Mid T	High T
$Pb_{36}Sn_{62}Ag_2$	48.8	113.6	174.8
$Pb_{40}Sn_{60}$	69.5	88.0	69.7
$Sn_{42}Bi_{58}$	162.6	16.9	96.7



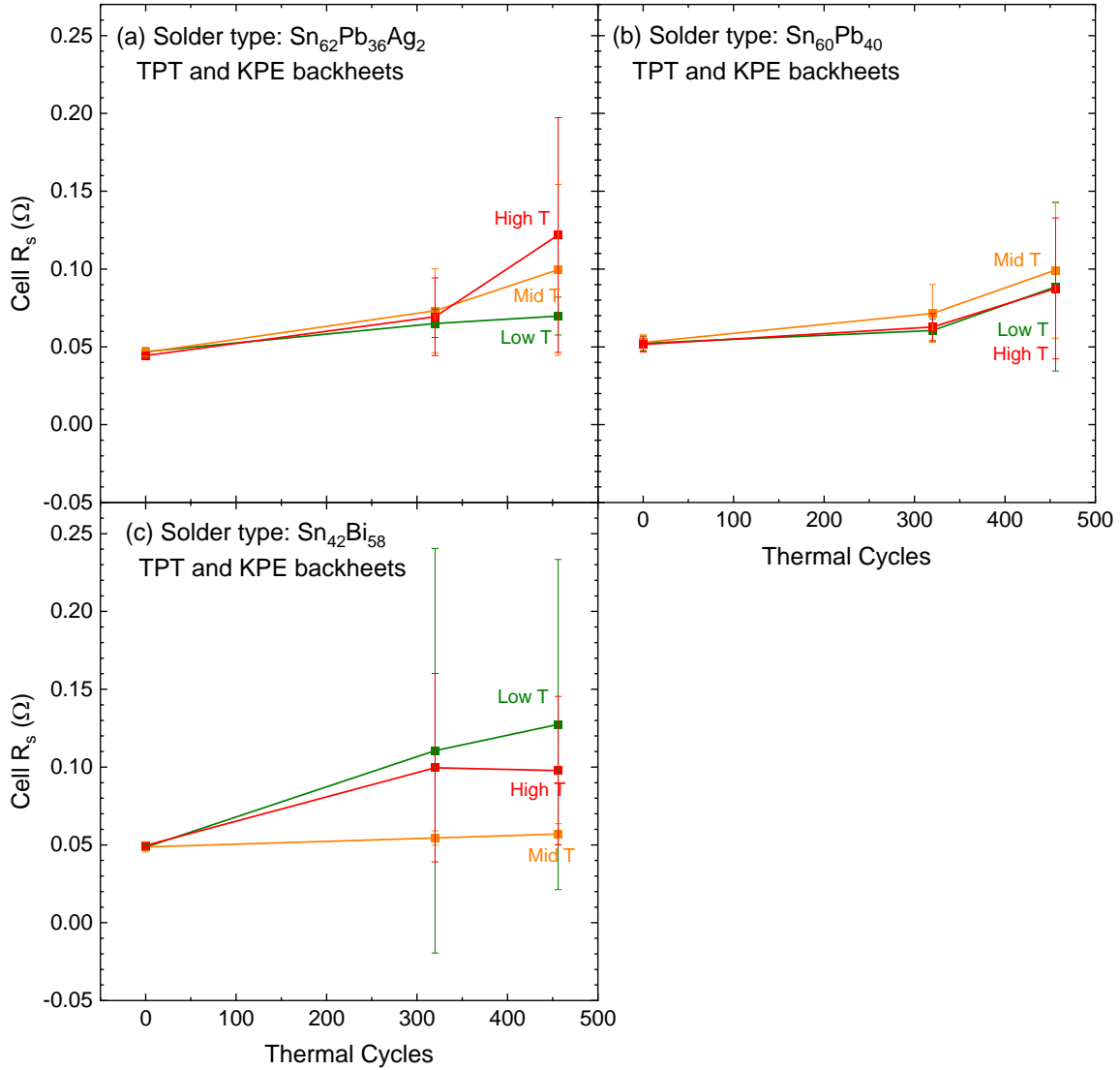


Fig. 68. Average  $R_s$  increase and standard deviation in the 9-cut-cell samples that underwent thermal cycling separated by solder type (a) for  $\text{Pb}_{36}\text{Sn}_{62}\text{Ag}_2$  (6 cells), (b) for  $\text{Pb}_{40}\text{Sn}_{60}$  (6 cells), and (c)  $\text{Sn}_{42}\text{Bi}_{58}$  (6 cells).

The change in  $R_s$  is plotted in Fig. 68 with each data point being an average of 6 cells: three each from samples with TPT and KPE backsheets. In all three solder bond types, the  $R_s$  increased slightly (less than three times of original  $R_s$ ) after 456 thermal cycles. The testing was terminated due to time constraints. The small increase observed in this 456-cycle study would be heavily influenced by the measurement uncertainty in  $R_s$  and hence

it is recommended to continue the thermal cycling beyond 456 cycles, preferably 700-800 cycles, to obtain true  $E_a$  values. The cells with  $\text{Sn}_{62}\text{Pb}_{42}\text{Ag}_2$  solder show some, though not significant, temperature dependent trend in the anticipated direction. However, not much  $R_s$  increase was observed from 320 cycles indicating the no wear-out degradation had occurred thus far. In cells with  $\text{Sn}_{60}\text{Pb}_{40}$  solder, no clear trends were evident and wear-out degradation was not observed until TC320. Cells with  $\text{Sn}_{42}\text{Bi}_{58}$  solder also have an inconsistent trend, possibly due to insignificant increase in  $R_s$  i) possibly due to non-uniform temperatures across the samples and ii) from  $R_s$  values which fall within the measurement uncertainty. The high standard deviation in the  $\text{Sn}_{42}\text{Bi}_{58}$  solder cells stems from a mix of negligible change in some cells and overall degradation in other cells. Further testing would be required to induce wear-out degradation in all cells. When the corresponding EL images of cells with the anomalous  $R_s$  increase from  $\text{Sn}_{60}\text{Pb}_{40}$  and  $\text{Sn}_{42}\text{Bi}_{58}$  solder types were examined in Fig. 69, a common factor observed was cell darkening and presence of bright spots suggesting current crowding. The IR images for the same cells showed areas within the cell that had a relatively higher temperature by roughly  $4^\circ\text{C}$ .

		Sn <sub>60</sub> Pb <sub>40</sub> solder					Sn <sub>42</sub> Bi <sub>58</sub> solder		
Sample		TC0	TC320	TC456	Sample		TC0	TC320	TC456
R <sub>s</sub> (Ω)		0.05	0.07	0.21	R <sub>s</sub> (Ω)		0.05	0.05	0.22
Low T TPT Cell 2				Low T TPT Cell 3					
R <sub>s</sub> (Ω)		0.06	0.11	0.16	R <sub>s</sub> (Ω)		0.05	0.40	0.32
Mid T KPE Cell 5				Low T TPT Cell 6					
R <sub>s</sub> (Ω)		0.05	0.07	0.16	R <sub>s</sub> (Ω)		0.05	0.19	0.15
Mid T KPE Cell 8				High T TPT Cell 6					
R <sub>s</sub> (Ω)		0.05	0.07	0.19	R <sub>s</sub> (Ω)		0.05	0.18	0.18
High T TPT Cell 2				High T TPT Cell 9					

Fig. 69. Individual cell-level EL images corresponding to cells with relatively higher R<sub>s</sub>. The cells exhibit cell darkening and formation of bright spots.

Each of these cells have cell darkening and/or bright spot formation. The IR images for the same cells showed areas within the cell that had a relatively higher temperature (~4°C). These cells have contributed to the lack of trend in Fig. 68b and Fig. 68c. The non-uniform degradation could indicate non-uniform temperatures in the samples during the hot dwell time.

From Fig. 70, the cells with Sn<sub>62</sub>Pb<sub>36</sub>Ag<sub>2</sub> solder have overall cell darkening and formation of some bright spots near busbars, especially close to solder joints. The bright spots indicate electron crowding due to increased R<sub>s</sub>. Some fingers seem to have lifted, resulting in areas of the cells darkening. In cells with Pb<sub>40</sub>Sn<sub>60</sub> solder, fewer bright spots

were observed than other cells, but some cell darkening was observed in High T samples. With Sn<sub>42</sub>Bi<sub>58</sub> solder, overall cell darkening was observed with most effect seen in the High T samples with some degradation in the Low T and Mid T samples.

A total of six samples with three different solder types and two different backsheets underwent 456 modified thermal cycles. The R<sub>s</sub> degradation, though insignificant, in the cells with Sn<sub>62</sub>Pb<sub>36</sub>Ag<sub>2</sub> solder type followed some temperature dependent trend enabling the calculation of an E<sub>a</sub> of 0.60 ± 0.13 eV (through the Arrhenius method). In the thermal cycling, the samples were subject to higher than field operating temperature, there was likely some growth of the IMC layer. The effect of TMF was probably dominant due to the 190 minutes out of the 220 minutes consisting of ramping temperatures. The cells with Pb<sub>40</sub>Sn<sub>60</sub> and Sn<sub>42</sub>Bi<sub>58</sub> solder types did not exhibit any consistent temperature dependency possibly due to insignificant increase in R<sub>s</sub> which falls within measurement uncertainty and non-uniform sample temperatures. The EL images of cells with anomalous R<sub>s</sub> values showed either cell darkening or bright spots along the busbars. The E<sub>a</sub> for the degradation of Pb<sub>40</sub>Sn<sub>60</sub> and Sn<sub>42</sub>Bi<sub>58</sub> solder types could not be calculated from these experiments.

Module		Modified Thermal Cycling								
Cycles		0 cycles			320 cycles			500 cycles		
Solder type		Sn <sub>62</sub> Pb <sub>36</sub> Ag <sub>2</sub>	Sn <sub>60</sub> Pb <sub>40</sub>	Sn <sub>42</sub> Bi <sub>58</sub>	Sn <sub>62</sub> Pb <sub>36</sub> Ag <sub>2</sub>	Sn <sub>60</sub> Pb <sub>40</sub>	Sn <sub>42</sub> Bi <sub>58</sub>	Sn <sub>62</sub> Pb <sub>36</sub> Ag <sub>2</sub>	Sn <sub>60</sub> Pb <sub>40</sub>	Sn <sub>42</sub> Bi <sub>58</sub>
TPT Backsheet	Low T 83°C									
	Mid T 94°C									
	High T 102°C									
KPE Backsheet	Low T 80°C									
	Mid T 92°C									
	High T 103°C									

Fig. 70. EL images of 9-cut-cell samples before, during, and after 456 thermal cycles.

## CHAPTER 5: CONCLUSIONS AND OUTLOOK

### 5.1 Encapsulant Browning and Solder Bond Degradation

The effects of encapsulant browning and solder bond degradation—the most commonly reported field degradation modes—are seen years after deployment. Through this work, the initial and end-of-life stages of these degradation modes were induced through exposure to accelerated UV exposure and modified TC testing carried out on field-aged modules and freshly fabricated samples. The unique features of the experimental approach are outlined below.

- Using field-aged (18 years - 21 years) and field-specific (hot-dry climate) modules reduced the overall testing time and activation energies for encapsulant browning and solder bond degradation were obtained for the wear-out failure/degradation stages.. Pre-stress testing characterizations reveal the extent of field-exposure induced degradation whereas post-stress testing characterizations reveal the extent of accelerated stress test induced degradation.
- Through active and passive heating methods, modules and samples were maintained at different elevated temperatures to enhance degradation and obtain an activation energy. One walk-in UV chamber and one environmental chamber was utilized to induce encapsulant browning and solder bond degradation at three different temperatures, respectively. The chambers were also used simultaneously for other samples of other researchers in the lab undergoing testing according to the IEC 61215 standard.
- Mostly non-destructive characterization methods were utilized to maximize the data obtained from the modules and samples.

- The  $E_a$  calculated was based on  $I_{sc}$  decrease for encapsulant browning or  $R_s$  increase for solder bond degradation and not  $P_{max}$  decrease. The parameter directly affected by the degradation mode was considered for analysis and characterization.
- Normally, one module would yield only one data point as the module performance parameter is normally measured using only the module output cables. Multiple cells of both types field-aged modules that underwent exposure to accelerated UV light and thermal cycling were individually accessed to obtain a statistically significant number of data points per temperature. The 9-cut-cell samples were also designed and fabricated for the same purpose of obtaining multiple data points at multiple temperatures in a single chamber.

#### 5.1.1 Field-Aged Modules

Multiple field-aged modules, maintained at different temperatures through passive heating, were exposed to 450 kWh/m<sup>2</sup> of UV exposure in a walk-in UV chamber. Modules from Solarex (MSX 60) and Siemens (M55) were used. The backsheet of both modules were covered in Al tape to prevent oxygen diffusion and photobleaching and intensify the encapsulant browning reaction. With increasing module temperature, more encapsulant browning was observed through i) increased fluorescence in UVF imaging, ii) increased YI in colorimetry, iii) decreased reflectance in spectral reflectance measurements, and iv) decreased  $I_{sc}$  in LI-V measurements. A drop in  $I_{sc}$  of 1.4%, 2.5%, and 3.3% was measured in the Low T, Mid T, and High T Solarex modules whereas a 4.1%, 5.7%, an 6.9% drop in the Siemens modules. The cell-level  $I_{sc}$  data from modules at different temperatures was used to calculate the  $E_a$  from an Arrhenius plot as 0.37 eV and 0.71 eV for MSX 60 modules

and M55 modules, respectively. The  $E_a$  was further used to predict the degradation rate for encapsulant browning for another climate.

The end-of-life stages of solder bond degradation were induced in field-aged modules through a modified TC test in two solder joint compositions:  $\text{Sn}_{62}\text{Pb}_{36}\text{Ag}_2$  (MSX 60) and  $\text{Sn}_{60}\text{Pb}_{40}$  (M55). To obtain data at three temperatures, one module would have to be placed in each chamber with a different upper temperature. In this study, each module had three individually controlled thermal blankets that helped maintain three upper temperatures during the hot dwell time thus reducing the number of modules required for testing. The MSX 60 module underwent 800 cycles whereas the M55 module underwent 400 cycles. Per 200 cycles, the increase in cell-level  $R_s$  for the Low T, Mid T, and High T regions was 5.3%, 5.5%, and 6.6%, respectively in the MSX 60 module. For the M55 module, the  $R_s$  increase was 27.6%, 39.8%, and 50.1%, for the Low T, Mid T, and High T regions, respectively. From the cell-level data, the  $E_a$  for solder bond degradation was calculated to be 0.12 eV ( $\text{Sn}_{62}\text{Pb}_{36}\text{Ag}_2$ ) and 0.35 eV ( $\text{Sn}_{60}\text{Pb}_{40}$ ). The degradation is thought to be driven by thermomechanical fatigue and creep. During fabrication and over the 18 – 21 years of field-exposure, most of the IMCs would have formed. During the 220 minute cycle, 190 minutes are spent ramping up or ramping down the temperatures. Cross-sectional SEM imaging showed a finer microstructure in the MSX 60 module than in the M55 module. There was complete phase segregation in the M55 module samples. EDXS compositional analysis identified the intermetallic compounds at the interfaces. The presence of 2wt% Ag at the solder joint is thought to inhibit grain coarsening, phase segregation and IMC formation. It also prevents silver scavenging from the Ag busbars.



### 5.1.2 Fresh 9-cut-cell Samples

To study the effects of encapsulant type, solder type, stressor type, stressor intensity, and backsheet type, freshly fabricated 9-cut-cell samples were exposed to i) accelerated UV light at elevated temperatures with and without humidity and ii) modified thermal cycling. Non-destructive characterization techniques were used on all samples before, during, and after the UV exposure.

In samples with UV Cut EVA both above and below the cells, a uniform browning was visible in UV fluorescence imaging which increased in intensity and area with increasing temperature and UV dosage. In samples with UVP EVA both above and below the cells, slight, but insignificant uniform browning was observed in UVF (not visually), possibly from non-UV-absorber additive in EVA or EVA main chain degradation itself. In samples with UVP EVA above the cells and UVC EVA below the cells, a ring-like browning pattern was observed that got thicker/wider with increasing UV exposure and sample temperature. More browning with diffuse borders was observed in the presence of humidity. It is possible that some UV absorber from the lower-UVC EVA between the cells first vertically diffused into the upper-UVP EVA between the cells during the lamination process and then laterally diffused to the cell edges. The diffused additives of lower-UVC EVA seems to be responsible for the ring-like browning pattern in the hybrid encapsulant structure with upper-UVP EVA and lower-UVC EVA. Encapsulant browning was most easily detectable by UVF imaging, then colorimetry, then reflectance and lastly through a drop in  $I_{sc}$ . Samples exposed to UV-T-RH have a less distinct and intense browning ring when

compared to samples exposed to UV-T. With more exposure to UV light, the ring of browning travels inward.

Samples with three types of solders were exposed to 456 cycles of a modified thermal cycling. A temperature dependent  $R_s$  increase trend was observed only in cells with  $\text{Sn}_{62}\text{Pb}_{36}\text{Ag}_2$  solder leading to an  $E_a$  calculation of 0.60 eV. Temperature non-uniformity could be causing the lack of a temperature dependent trend in cells with  $\text{Sn}_{60}\text{Pb}_{40}$  and  $\text{Sn}_{42}\text{Bi}_{58}$  solders. It is likely that more cycles are required to initiate wear-out stages of failure.

Multiple testing approaches have been tried and streamlined for i) saving time, ii) saving resources, iii) testing multiple conditions within one test chamber, iv) increased statistical significance. The proposed experiments are designed to take a deeper look at the effect of stressors and their interactions on encapsulant browning and solder bond degradation with the abovementioned features.

## 5.2 Outlook

Browning and delamination are problems that encapsulants face often in field-exposure. Researching encapsulant browning and solder bond degradation is critical to extending the reliability of modules. The research approach should account for the environmental factors that affect encapsulant browning and solder bond degradation.

### Encapsulant Degradation

- Testing can be continued beyond UV225 to induce more degradation. UVF image processing could help immensely in calculating the speed of the browning ring moving inwards with respect to temperature and stressor condition set. Image processing could also help with correlating the effective area of browning with  $I_{sc}$  drop.
- A “tear-away” design for the samples could be incorporated allowing small parts of the sample to be used for destructive testing. Without the integrity of the rest of the module compromised, it can continue to undergo stress testing. Destructive testing of these samples would help explain the underlying mechanisms of the two degradation modes in materials commonly used in the industry.
- Including water and acid detection strips would help visualize the extent of water ingress within the samples.
- Encapsulants, prior to sample fabrication, can be characterized by i) Raman spectroscopy, ii) Fourier-Transform Infra-Red spectroscopy, iii) UV-Vis spectroscopy, and iv) Gas Permeation Chromatography – Mass Spectroscopy.
- Samples for destructive testing can be obtained by coring the laminate or by water jet cutting.

## Solder Bond Degradation

- Thermal cycling can continue beyond 456 cycles to induce wear-out stages of solder bond degradation.
- A “tear-away” design for the samples could be incorporated allowing small regions of the sample to be used for destructive testing. With the integrity of the rest of the module intact, it can continue to undergo stress testing.
- A thermal cycling profile with longer dwell times would encourage IMC formation during the initial part of testing.
- Contact resistance measurements can be taken after cell tabbing/before lamination and compared with measurements after testing.
- Lock-in-thermography (LIT) would give more insight into the degradation location at the ribbon-solder-cell interfaces compared to conventional IR imaging.
- EL imaging combined with image processing can provide more information about the solder bond degradations
- *In situ* DIV  $R_s$  measurements could be taken for each thermal cycle with the proper equipment, allowing for the determination of which cycle major changes in  $R_s$  occur. The rate of  $R_s$  increase per cycle could also be determined to compare sudden and gradual degradation modes. Testing could also be stopped to investigate an isolated degradation with EL and IR.

## REFERENCES

- [1] G. Masson and I. Kaizuka, “IEA PVPS Trends in Photovoltaic Applications,” 2019.
- [2] Fraunhofer Institute for Solar Energy Systems, *Photovoltaics Report*, no. March. 2019.
- [3] A. W. Czanderna and F. J. Pern, “Encapsulation of PV modules using ethylene vinyl acetate copolymer as a pottant: A critical review,” *Sol. Energy Mater. Sol. Cells*, vol. 43, no. 2, pp. 101–181, 1996.
- [4] D. Wu, J. Zhu, T. Betts, and R. Gottschalg, “PV module degradation mechanisms under different environmental stress factors,” in *8th Photovoltaic Science Application and Technology Conference (PVSAT-8)*, 2012, pp. 177–180.
- [5] M. Köntges, *Performance and reliability of photovoltaic systems subtask 3.2: Review of failures of photovoltaic modules : {IEA PVPS} task 13 : external final report {IEA-PVPS}*. Sankt Ursen: International Energy Agency, Photovoltaic Power Systems Programme, 2014.
- [6] V. Sharma and S. S. Chandel, “Performance and degradation analysis for long term reliability of solar photovoltaic systems: A review,” *Renew. Sustain. Energy Rev.*, vol. 27, pp. 753–767, 2013.
- [7] J. Oh, “Elimination of Potential-Induced Degradation for Crystalline Silicon Solar Cells,” Arizona State University, 2016.
- [8] A. Zielnik, “Solar ABCs Validating Photovoltaic Module Durability Tests,” 2013.
- [9] E. Suhir, “Aging-related failure rate obtained from bathtub curve data,” in *2015 IEEE Aerospace Conference*, 2015, pp. 1–8.
- [10] U.S. Department of Energy Office of Indian Energy Policy and Programs, “Levelized Cost of Energy (LCOE),” 2015.
- [11] M. Woodhouse *et al.*, “On the Path to SunShot: The Role of Advancements in Solar Photovoltaic Efficiency, Reliability, and Costs,” *Natl. Renew. Energy Lab.*, no. May, p. 44, 2016.
- [12] A. Phinikarides, N. Kindyni, G. Makrides, and G. E. Georghiou, “Review of photovoltaic degradation rate methodologies,” *Renew. Sustain. Energy Rev.*, vol. 40, pp. 143–152, 2014.
- [13] D. Wu, “Investigation of the reliability of the encapsulation system of photovoltaic modules,” Loughborough University, 2015.

- [14] F. J. Pern, "Luminescence and absorption characterization of ethylene-vinyl acetate encapsulant for PV modules before and after weathering degradation," *Polym. Degrad. Stab.*, vol. 41, no. 2, pp. 125–139, 1993.
- [15] R. Hoogenboom, "Temperature-responsive polymers: Properties, synthesis and applications," in *Smart Polymers and their Applications*, 2014, p. 94.
- [16] F. J. Pern, "Ethylene vinyl acetate (EVA) encapsulants for photovoltaic modules: Degradation and discoloration mechanisms and formulation modifications for improved," *Die Angew. Makromol. Chemie*, vol. 252, pp. 195–216, 1997.
- [17] J. Schlothauer, S. Jungwirth, M. Köhl, and B. Röder, "Degradation of the encapsulant polymer in outdoor weathered photovoltaic modules: Spatially resolved inspection of EVA ageing by fluorescence and correlation to electroluminescence," *Sol. Energy Mater. Sol. Cells*, vol. 102, pp. 75–85, 2012.
- [18] W. Brune, "The Solar Spectrum." [Online]. Available: <https://www.e-education.psu.edu/meteo300/node/683>. [Accessed: 25-Jul-2019].
- [19] F. J. Pern, "Factors that affect the EVA encapsulant discoloration rate upon accelerated exposure," *Sol. Energy Mater. Sol. Cells*, vol. 41–42, pp. 587–615, 1996.
- [20] C. Peike, L. Purschke, K. A. Weiss, M. Kohl, and M. Kempe, "Towards the origin of photochemical EVA discoloration," *Conf. Rec. IEEE Photovolt. Spec. Conf.*, pp. 1579–1584, 2013.
- [21] M. C. C. de Oliveira, A. S. A. Diniz Cardoso, M. M. Viana, and V. de F. C. Lins, "The causes and effects of degradation of encapsulant ethylene vinyl acetate copolymer (EVA) in crystalline silicon photovoltaic modules: A review," *Renewable and Sustainable Energy Reviews*, vol. 81, pp. 2299–2317, 2018.
- [22] M. D. Kempe, G. J. Jorgensen, K. M. Terwilliger, T. J. McMahon, C. E. Kennedy, and T. T. Borek, "Acetic acid production and glass transition concerns with ethylene-vinyl acetate used in photovoltaic devices," *Sol. Energy Mater. Sol. Cells*, vol. 91, no. 4, pp. 315–329, 2007.
- [23] F. J. Pern and A. W. Czanderna, "Characterization of ethylene vinyl acetate (EVA) encapsulant: Effects of thermal processing and weathering degradation on its discoloration," *Sol. Energy Mater. Sol. Cells*, vol. 25, no. 1–2, pp. 3–23, 1992.
- [24] P. Klemchuk *et al.*, "Investigation of the degradation and stabilization of EVA-based encapsulant in field-aged solar energy modules," *Polym. Degrad. Stab.*, vol. 55, no. 3, pp. 347–365, 1997.

- [25] C. C. Gonzalez, R. Liang, and R. G. Ross, "Predicting Field Performance of Photovoltaic Modules From Accelerated Thermal and Ultraviolet Aging Data," *Int. Sol. Energy Soc. Meet.*, vol. 3, pp. 1775–1779, 1986.
- [26] M. D. Kempe, "Ultraviolet light test and evaluation methods for encapsulants of photovoltaic modules," *Sol. Energy Mater. Sol. Cells*, vol. 94, no. 2, pp. 246–253, 2010.
- [27] C. Peike, T. Kaltenbach, K. A. Weiß, and M. Koehl, "Indoor vs. outdoor aging: polymer degradation in PV modules investigated by Raman spectroscopy," *SPIE Vol. 8472*, vol. 8472, p. 84720V, 2012.
- [28] F. J. Pern and A. W. Czanderna, "EVA degradation mechanisms simulating those in PV modules," *AIP Conf. Proc.*, vol. 268, no. 1992, pp. 445–452, 1992.
- [29] J. H. Wohlgemuth, M. D. Kempe, and D. C. Miller, "Discoloration of PV encapsulants," *Conf. Rec. IEEE Photovolt. Spec. Conf.*, pp. 3260–3265, 2013.
- [30] M. Köntges *et al.*, "IEA PVPS Review of Failures of Photovoltaic Modules," 2014.
- [31] C. Peike, P. Hülsmann, M. Blüml, P. Schmid, K.-A. Weiß, and M. Köhl, "Impact of Permeation Properties and Backsheet-Encapsulant Interactions on the Reliability of PV Modules," *ISRN Renew. Energy*, vol. 2012, pp. 1–5, 2012.
- [32] G. TamizhMani and J. Kuitche, "Accelerated Lifetime Testing of Photovoltaic Modules Solar America Board for Codes and Standards," *Sol. ABC*, no. July, p. 106, 2013.
- [33] J. H. Kim, Y. Lyu, D. C. Miller, and X. Gu, "Characterizations of aged Glass / Ethylene Vinyl Acetate / Glass using fluorescence spectroscopy and instrumented indentation," in *Photovoltaic Specialist Conference*, 2017, pp. 3195–3199.
- [34] M. Köntges, A. Morlier, G. Eder, and E. Fleiß, "IEA PVPS Applications and Interpretation of UV Fluorescence Imaging for PV Plants," 2019, no. May.
- [35] B. Gilleland, W. B. Hobbs, and J. B. Richardson, "High Throughput Detection of Cracks and Other Faults in Solar PV Modules Using a High-Power Ultraviolet Fluorescence Imaging System," no. September, pp. 2575–2582, 2020.
- [36] IEC, *Terrestrial photovoltaic (PV) modules - Design qualification and type of approval - Part 2: Test Procedures*, vol. 61215–2. 2016.
- [37] S. Chattopadhyay *et al.*, "Visual degradation in field-aged crystalline silicon PV modules in India and correlation with electrical degradation," *IEEE J. Photovoltaics*, vol. 4, no. 6, pp. 1470–1476, 2014.

- [38] P. Hulsmann, K. A. Weiss, and M. Kohl, “Temperature-dependent water vapour and oxygen permeation through different polymeric materials used in photovoltaic modules,” *Prog. Photovoltaics Res. Appl.*, vol. 22, pp. 415–421, 2014.
- [39] E. Ashford, W. Brennan, A. Whitehead, A. Seaman, and E. Parnham, “Yellowing of PV Backsheets in Accelerated Tests Can Be Used as a Realistic Indication of Possible Field Failures – Fact or Fiction?,” *32nd Eur. Photovolt. Sol. Energy Conf. Exhib.*, pp. 1528–1531, 2016.
- [40] T. . H. Kim, N. . C. Park, and D. H. H. Kim, “The effect of moisture on the degradation mechanism of multi-crystalline silicon photovoltaic module,” *Microelectron. Reliab.*, vol. 53, no. 9–11, pp. 1823–1827, 2013.
- [41] P. Hülsmann, D. Philipp, and M. Köhl, “Measuring temperature-dependent water vapor and gas permeation through high barrier films,” *Rev. Sci. Instrum.*, vol. 80, no. 11, 2009.
- [42] M. D. Kempe, “Modeling of rates of moisture ingress into photovoltaic modules,” *Sol. Energy Mater. Sol. Cells*, vol. 90, no. 16, pp. 2720–2738, 2006.
- [43] H. Wirth, K. A. Weiss, and C. Wiesmeier, *Photovoltaic Modules Technology and Reliability*. De Gruyter, 2016.
- [44] W. Callister and D. Rethwisch, *Materials science and engineering: an introduction*, vol. 94. 2007.
- [45] H. Oberg, Erik, Day Jones, Franklin, Lynedon Horton, *Machinery’s Handbook: A Reference Book for the Mechanical Engineer, Designer, Manufacturing Engineer, Draftsman, Toolmaker, and Machinist*, 23rd ed. Industrial Press, 1988, 1988.
- [46] J. DeVore, A, “Fatigue Resistance of Solders,” in *National Electronic Packaging and Production Conference*, 1982, pp. 409–414.
- [47] P. Schmitt, P. Kaiser, C. Savio, M. Tranitz, and U. Eitner, “Intermetallic phase growth and reliability of Sn-Ag-soldered solar cell joints,” *Energy Procedia*, vol. 27, no. April, pp. 664–669, 2012.
- [48] N. Bosco, T. J. Silverman, and S. Kurtz, “Climate specific thermomechanical fatigue of flat plate photovoltaic module solder joints,” *Microelectron. Reliab.*, vol. 62, pp. 124–129, Jul. 2016.
- [49] D. R. Frear and P. T. Vianco, “Intermetallic growth and mechanical behavior of low and high melting temperature solder alloys,” *Metall. Mater. Trans. A*, vol. 25, no. 7, pp. 1509–1523, Jul. 1994.



- [50] H. Tang and C. Basaran, "Influence of microstructure coarsening on thermomechanical fatigue behavior of Pb/Sn eutectic solder joints," *Int. J. Damage Mech.*, vol. 10, no. 3, pp. 235–255, 2001.
- [51] U. Itoh, M. Yoshida, H. Tokuhisa, K. Takeuchi, and Y. Takemura, "Solder joint failure modes in the conventional crystalline Si module," *Energy Procedia*, vol. 55, no. 3, pp. 464–468, 2014.
- [52] T. Geipel, M. Moeller, J. Walter, A. Kraft, and U. Eitner, "Intermetallic compounds in solar cell interconnections: Microstructure and growth kinetics," *Sol. Energy Mater. Sol. Cells*, vol. 159, pp. 370–388, Jan. 2017.
- [53] Y. Xi, L. J. Liu, F. Q. Zu, and Z. H. Chen, "Effect of temperature-induced discontinuous liquid structure change on the solidification behavior and solidified structures of Pb-Sn alloy," *Kov. Mater.*, vol. 43, pp. 432–439, 2005.
- [54] C. H. Yeh, L. S. Chang, and B. B. Straumal, "Wetting transition of grain boundaries in the Sn-rich part of the Sn-Bi phase diagram," *J. Mater. Sci.*, vol. 46, no. 5, pp. 1557–1562, 2011.
- [55] F. Rosebury, *Handbook of Electron Tube and Vacuum Techniques*. American Inst. of Physics, 1997.
- [56] P. Gierth, L. Rebenklau, and A. Michaelis, "Evaluation of soldering processes for high efficiency solar cells," *Proc. Int. Spring Semin. Electron. Technol.*, pp. 133–137, 2012.
- [57] Qualitek, "Physical Properties Solder Composition." .
- [58] I. Tsai, E. Wu, S. F. Yen, and T. H. Chuang, "Mechanical properties of intermetallic compounds on lead-free solder by moiré techniques," *J. Electron. Mater.*, vol. 35, no. 5, pp. 1059–1066, 2006.
- [59] NIST, "Mechanical Properties of Intermetallic Compounds Formed Between Tin (Solder) and Copper or Nickel." [Online]. Available: [https://www.metallurgy.nist.gov/mechanical\\_properties/solder\\_mechanicalprop.html](https://www.metallurgy.nist.gov/mechanical_properties/solder_mechanicalprop.html). [Accessed: 29-Jul-2019].
- [60] Y. Tian, N. Ren, Z. Zhao, F. Wu, and S. K. Sitaraman, "Ag<sub>3</sub>Sn compounds coarsening behaviors in micro-joints," *Materials (Basel)*, vol. 10, no. 12, pp. 1–12, 2018.
- [61] Royal Society of Chemistry, "Periodic Table – Royal Society of Chemistry." [Online]. Available: <http://www.rsc.org/periodic-table>. [Accessed: 29-Jul-2019].

- [62] S. Ahat, L. Du, M. Sheng, L. Luo, W. Kempe, and J. Freytag, "Effect of aging on the microstructure and shear strength of SnPbAg/Ni-P/Cu and SnAg/Ni-P/Cu solder joints," *J. Electron. Mater.*, vol. 29, no. 9, pp. 1105–1109, 2000.
- [63] T. T. Luu, A. Duan, K. E. Aasmundtveit, and N. Hoivik, "Optimized Cu-Sn wafer-level bonding using intermetallic phase characterization," *J. Electron. Mater.*, vol. 42, no. 12, pp. 3582–3592, 2013.
- [64] J. Gong, C. Liu, P. P. Conway, and V. V. Silberschmidt, "Formation of Ag<sub>3</sub>Sn plates in SnAgCu solder bumps," *Mater. Sci. Eng. A*, vol. 527, no. 10–11, pp. 2588–2591, 2010.
- [65] H. A. Zarmani, M T, Ekere, N N, Oduoza, C F, Emeka, "Evaluation of thermo-mechanical damage and fatigue life of solar cell solder interconnections," *Robot. Comput. Manuf.*, vol. 47, pp. 37–43, 2017.
- [66] J. H. Wohlgemuth, *Photovoltaic Module Reliability*. John Wiley & Sons, 2020.
- [67] R. J. Crawford and J. L. Throne, *Rotational Molding Technology*. 2002.
- [68] H. Ma and J. C. Suhling, "A review of mechanical properties of lead-free solders for electronic packaging," *J. Mater. Sci.*, vol. 44, no. 5, pp. 1141–1158, 2009.
- [69] Y. Zhang, H. Zhu, M. Fujiwara, J. Xu, and M. Dao, "Low-temperature creep of SnPb and SnAgCu solder alloys and reliability prediction in electronic packaging modules," *Scr. Mater.*, vol. 68, no. 8, pp. 607–610, 2013.
- [70] B. C. Hendrix, "The interaction of creep and fatigue in lead-tin solders," Columbia University, 1989.
- [71] R. G. Ross, L. C. Wen, G. R. Mon, E. Jetter, and J. Winslow, "Creep-Fatigue Behavior of Microelectronic Solder Joints," *MRS Proc.*, vol. 226, pp. 1–6, 1991.
- [72] M. T. Zarmai, N. N. Ekere, C. F. Oduoza, and E. H. Amalu, "Optimization of thermo-mechanical reliability of solder joints in crystalline silicon solar cell assembly," *Microelectron. Reliab.*, vol. 59, pp. 117–125, 2016.
- [73] G. Abadias *et al.*, "Review Article: Stress in thin films and coatings: Current status, challenges, and prospects," *J. Vac. Sci. Technol. A Vacuum, Surfaces, Film.*, vol. 36, no. 2, p. 020801, 2018.
- [74] V. Jung and M. Köntges, "Al/Ni : V/Ag metal stacks as rear-side metallization for crystalline silicon solar cells," *Prog. Photovoltaics Res. Appl.*, vol. 21, no. 5, p. n/a-n/a, Feb. 2012.

- [75] R. L. J. M. Ubachs, P. J. G. Schreurs, and M. G. D. Geers, "Microstructure evolution of tin-lead solder," *IEEE Trans. Components Packag. Technol.*, vol. 27, no. 4, pp. 635–642, 2004.
- [76] M. S. Kang, Y. J. Jeon, D. S. Kim, and Y. E. Shin, "Comparison of the 60Sn40Pb and 62Sn2Ag36Pb solders for a PV ribbon joint in photovoltaic modules using the thermal shock test," *Energies*, vol. 10, no. 4, pp. 1–11, 2017.
- [77] C. A. Bulwith, R A, Mackay, "Silver Scavenging Inhibition of Some Silver Loaded Solders," *Weld. Res. Suppl.*, p. 89, 1985.
- [78] G. M. Kimball *et al.*, "Global acceleration factors for damp heat tests of PV modules," *Conf. Rec. IEEE Photovolt. Spec. Conf.*, vol. 2016-Novem, pp. 101–105, 2016.
- [79] D. L. King, M. A. Quintana, J. A. Kratochvil, D. E. Ellibee, and B. R. Hansen, "Photovoltaic module performance and durability following long-term field exposure," *Prog. Photovoltaics Res. Appl.*, vol. 8, no. 2, pp. 241–256, 2000.
- [80] M. Abramowitz and M. Davidson, "Fluorescence - Overview of Fluorescence Excitation and Emission Fundamentals." [Online]. Available: <https://www.olympus-lifescience.com/en/microscope-resource/primer/lightandcolor/fluoroexcitation/>. [Accessed: 24-Jul-2019].
- [81] Solmetric, "PV Array Performance Troubleshooting Flowchart." [Online]. Available: <http://tools.solmetric.com/Tools/Poster>. [Accessed: 26-May-2019].
- [82] G. Tamizhmani, K. Paghastian, J. Kuitche, M. G. Vemula, and G. Sivasubramanian, "Photovoltaic Module Power Rating per IEC 61853-1 Standard: Solar America Board for Codes and Standards."
- [83] A. Guechi, M. Chegaar, and M. Aillerie, "Solar Cells Parameters Evaluation from Dark I-V Characteristics," *Energy Procedia*, vol. 18, no. 1, pp. 1611–1623, 2012.
- [84] A. Namin, C. Jivacate, D. Chenvidhya, K. Kirtikara, and J. Thongpron, "Construction of Tungsten Halogen, Pulsed LED, and Combined Tungsten Halogen-LED Solar Simulators for Solar Cell I - V Characterization and Electrical Parameters Determination ," *Int. J. Photoenergy*, vol. 2012, pp. 1–9, 2012.
- [85] "Solar panel micro cracks explained." [Online]. Available: <https://sinovoltaics.com/quality-control/solar-panel-quality-an-introduction-to-micro-cracks/>. [Accessed: 26-May-2019].
- [86] "PV (Photo-voltaic or Solar Panel) Safety & Operational Inspections » Monroe Infrared." [Online]. Available: <https://monroeinfrared.com/infrared-inspections/ir-maintenance-inspections/pv-infrared-inspections/>. [Accessed: 26-May-2019].

- [87] “Quantum Efficiency | PVEducation.” [Online]. Available: <https://www.pveducation.org/pvcdrom/solar-cell-operation/quantum-efficiency>. [Accessed: 26-May-2019].
- [88] “What is E313 Yellowness Index and how is it calculated? – Hunterlab.” [Online]. Available: <https://support.hunterlab.com/hc/en-us/articles/203952825-What-is-E313-Yellowness-Index-and-how-is-it-calculated->. [Accessed: 26-May-2019].
- [89] T. Smith and J. Guild, “The C.I.E. colorimetric standards and their use,” *Trans. Opt. Soc.*, vol. 33, no. 3, pp. 73–134, Jan. 1931.
- [90] J. V. Li, S. W. Johnston, Y. Yan, and D. H. Levi, “Measuring temperature-dependent activation energy in thermally activated processes: A 2D Arrhenius plot method,” *Rev. Sci. Instrum.*, vol. 81, no. 3, 2010.
- [91] D. C. Miller *et al.*, “Degradation in PV encapsulant strength of attachment: An interlaboratory study towards a climate-specific test,” in *Conference Record of the IEEE Photovoltaic Specialists Conference*, 2015, no. July, pp. 95–100.
- [92] “IEC 61215: Crystalline silicon terrestrial photovoltaic (PV) modules - Design qualification and type approval,” 2005.
- [93] D. J. Veerendra Kumar and D. J. V. Kumar, “Determination of Activation Energy for Encapsulant Browning of Photovoltaic Modules,” Arizona State University, 2016.
- [94] H. Gopalakrishna, A. Sinha, K. Dolia, D. Jordan, and G. Tamizhmani, “Nondestructive Characterization and Accelerated UV Testing of Browning Field-Aged PV Modules,” *IEEE J. Photovoltaics*, vol. 9, no. 6, pp. 1733–1740, 2019.
- [95] J. Schindelin *et al.*, “Fiji: An open-source platform for biological-image analysis,” *Nat. Methods*, vol. 9, no. 7, pp. 676–682, 2012.
- [96] “National Solar Radiation Database (NSRDB),” <https://nsrdb.nrel.gov/>. .
- [97] K. Dolia, “Accelerated UV Testing and Characterization of PV Modules with UV-cut and UV-pass EVA Encapsulants,” Arizona State University, 2018.
- [98] P. Arularasu, “Combined UV-Temperature-Humidity Accelerated Testing of PV Modules : Reliability of UV-cut and UV-pass EVA Encapsulants,” Arizona State University, 2019.
- [99] S. Spataru, P. Hacke, D. Sera, S. Glick, T. Kerekes, and R. Teodorescu, “Quantifying solar cell cracks in photovoltaic modules by electroluminescence imaging,” *2015 IEEE 42nd Photovolt. Spec. Conf. PVSC 2015*, pp. 1–6, 2015.

- [100] P. L. Tu, Y. C. Chan, and J. K. L. Lai, "Effect of intermetallic compounds on the thermal fatigue of surface mount solder joints," *IEEE Trans. Components Packag. Manuf. Technol. Part B*, vol. 20, no. 1, pp. 87–93, 1997.
- [101] M. A. Quintana, D. L. King, T. J. McMahon, and C. R. Osterwald, "Commonly observed degradation in field-aged photovoltaic modules," *Conf. Rec. Twenty-Ninth IEEE Photovolt. Spec. Conf. 2002.*, pp. 1436–1439.
- [102] P. L. Hacke, A. F. Sprecher, and H. Conrad, "Microstructure coarsening during thermo-mechanical fatigue of Pb-Sn solder joints," *J. Electron. Mater.*, vol. 26, no. 7, pp. 774–782, 1997.
- [103] J. Lin, "UVFL Inspection: Drones and Tools," in *UV Fluorescence Measurement for Damage Assessment of PV Modules*, 2018.
- [104] D. Mayrhofer, "Exceptional UV features in the Field," in *UV Fluorescence Measurement for Damage Assessment of PV Modules*, 2018.
- [105] E. Fleiss and M. Diehl, "UV-Fluorescence: Experiences from the Field," in *UV Fluorescence Measurement for Damage Assessment of PV Modules*, 2018.

APPENDIX A

LIST OF PUBLICATIONS

- JOURNAL PAPERS – ACCEPTED FOR PUBLICATION
  - H. Gopalakrishna, A. Sinha, K. Dolia, D. Jordan, G. Tamizhmani, “Non-destructive Characterization and Accelerated UV Testing of Browning Field-aged PV Modules,” IEEE J. Photovoltaics, 2019
  - A. Sinha, H. Gopalakrishna, A. Bala Subramaniyan, J. Oh, G. Tamizhmani, “Prediction of Climate-specific Degradation Rate for Photovoltaic Encapsulant Discoloration,” IEEE J. Photovoltaics, 2020
  
- JOURNAL PAPERS – UNDER REVIEW OR IN THE WORKS
  - H. Gopalakrishna, A. Sinha, J. Carpenter, S. Niverty, N. Chawla, D. Jordan, G. Tamizhmani, “Accelerated Stress Testing of Field-aged Modules: Solder Bond Degradation,” IEEE J. Photovoltaics, 2020
  - H. Gopalakrishna, G. Tamizhmani, “Influence of Backsheet Type on Encapsulant Browning with and Without Humidity,” Journal TBD, 2020
  - H. Gopalakrishna, G. Tamizhmani, “Influence of Composition on Solder Bond Degradation with and Without Humidity,” Journal TBD, 2020
  
- CONFERENCE PAPERS, POSTERS, AND PRESENTATIONS
  - H. Gopalakrishna, A. Sinha, D. Jordan, G. Tamizhmani, “Activation Energy for Solder Bond Degradation: Thermal Cycling of Field-aged Modules at Multiple Upper Temperatures,” IEEE Photovoltaic Specialists Conference, 2019

- H. Gopalakrishna, P. Arularasu, K. Dolia, A. Sinha, G. Tamizhmani, “Characterization of Encapsulant Degradation in Accelerated UV Stressed Mini-Modules with UV-cut and UV-pass EVA,” IEEE Photovoltaic Specialists Conference, 2019
- P. Arularasu, H. Gopalakrishna, A. Sinha, G. TamizhMani, “Role of Humidity on the Degradation of UV-cut and UV-pass Encapsulants,” Photovoltaic Reliability Workshop, 2019
- P. Arularasu, H. Gopalakrishna, A. Sinha, G. TamizhMani, “Degradation Comparison of UV-cut and UV-pass Encapsulants,” Photovoltaic Reliability Workshop, 2019
- H. Gopalakrishna, A. Sinha, J. Oh, K. Dolia, S. Tatapudi, G. Tamizhmani, “Novel Accelerated UV Testing of Field-Aged Modules: Correlating EL and UV Fluorescence Images with Current Drop,” IEEE 7<sup>th</sup> World Conference on Photovoltaic Energy Conversion, 2018
- H. Gopalakrishna et al. “Novel Accelerated UV Testing of Field Aged Modules: Correlating EL and UV Fluorescence Images with Current Drop”, Photovoltaic Reliability Workshop, 2018
- H. Gopalakrishna, J. Oh, D. Jordan, S. Tatapudi, J. Kuitche, R. Pan, G. TamizhMani, “Novel Accelerated UV Testing of Field Aged Modules: Correlating EL and UV Fluorescence Images with Current Drop,” Photovoltaic Reliability Workshop, 2018



- J. Wu, E. Chan, R. Yadav, H. Gopalakrishna, G. Tamizhmani, “Durability Evaluation of PV Modules using Image Processing Tools,” Society of Photo-Optical Instrumentation Engineers, 2018
- A. Bala Subramaniyan, A. Sinha, S. Pore, H. Gopalakrishna, R. Pan, G. Tamizhmani, “Acceleration factor for damp heat testing of PV modules,” Society of Photo-Optical Instrumentation Engineers, 2018
- A. Sinha, A. Balasubramaniyan, S. Pore, H. Gopalakrishna, J. Oh, S. Tatapudi, G. TamizhMani, “Degradation Rate Modeling for Encapsulant Discoloration of Photovoltaic Modules,” Sandia’s PVPMC Workshop, 2018